

Photophysics of organic light-emitting diodes

—

Device efficiency and degradation processes

Dissertation

zur Erlangung des
Doktorgrades der Naturwissenschaften
(Dr. rer. nat.)

eingereicht an der
Mathematisch-Naturwissenschaftlichen Fakultät
der Universität Augsburg

vorgelegt von
Tobias D. Schmidt

geb. 18. März 1983
in Augsburg

April 2013

1. Gutachter: Prof. Dr. Wolfgang Brütting

2. Gutachter: Prof. Dr. Achim Wixforth

Tag der mündlichen Prüfung: 25.06.2013



CONTENTS

1	Introduction	1
2	Basic principles of organic light-emitting diodes (OLEDs)	5
2.1	Organic semiconductors	5
2.1.1	Optical properties	7
2.1.2	Electrical properties	14
2.2	Organic light-emitting diodes	18
2.2.1	Device operation	18
2.2.2	External quantum efficiency (EQE)	21
2.3	Optical modeling	25
2.3.1	Optical modes	25
2.3.2	Optical simulation	26
3	Device preparation, materials and stack design	33
3.1	Devices fabricated at University of Augsburg	33
3.2	Devices provided by OSRAM Opto Semiconductors	37
4	Experimental techniques	39
4.1	Current-voltage-luminance characteristics	39
4.2	Impedance spectroscopy	41
4.3	Time-resolved luminescence spectroscopy	44
4.3.1	Basic principles	44
4.3.2	Examples of time-resolved measurement concepts	48
5	Comprehensive efficiency analysis of OLEDs	57
5.1	RQE determination via integrating sphere measurements	61
5.2	RQE determination using simplified structures	64

5.2.1	Using SiO ₂ as optical spacer	65
5.2.2	Using LiF as optical spacer	69
5.3	RQE determination via microcavity OLEDs	74
5.4	Efficiency analysis of state-of-the-art phosphorescent OLEDs	77
5.4.1	Influence of the matrix material	79
5.4.2	Influence of the current density	84
5.4.3	Influence of non-isotropic emitter orientation	86
5.5	Comprehensive efficiency analysis of fluorescent OLEDs	98
5.6	Conclusions and further work	106
6	Degradation processes in OLEDs	111
6.1	OLED devices with short RC-times	112
6.2	Degradation analysis for low latency devices	116
6.3	Efficiency analysis after degradation of OLEDs	121
6.4	Conclusions and further work	127
7	Summary	133
8	Appendix	139
	References	141
	Danksagung	154

CHAPTER 1

INTRODUCTION

Organic light-emitting diodes (OLEDs) have promising applications in both display technology as well as in general lighting. The advantages of OLEDs are miscellaneous as it is possible to fabricate low-cost, lightweight, thin and flat large-area devices, that can even be produced on flexible substrates such as polymer or metal foils and can achieve a semi-transparent character. The total thickness of the organic layers inside the diode comprises only one to a few hundred nanometers and thus the total thickness is limited by the substrate and the encapsulation. The different organic materials are normally sandwiched between one (semi-)transparent and one reflecting electrode. Applying a voltage of a few volts to the electrodes results in charge carrier injection into the device followed by radiative recombination and therewith a strong electroluminescence from the organic layers inside the OLED.

In 1963 the first observation of electroluminescence of an organic crystal was presented by Pope et al. [1]. However, several thousand volts were needed to detect a clear luminescence signal from the 5 mm thick anthracene crystal. It took more than 20 years after these results until Tang and van Slyke had demonstrated the first efficient, low voltage driven OLED based on thin films from small organic molecules in 1987 [2]. In 1990 the first solution processed polymer based OLED was developed by Burroughes et al. [3] and therewith the starting signal for a new, rapidly growing field of research had been given.

In the following years a huge amount of results has been published in this field of research and the efficiencies of OLEDs could be increased continuously. Recently white OLEDs with efficacies of 87 lm/W could be demonstrated at brightnesses of about 1000 cd/m² [4]. This value is close to that of fluorescent tubes and so the entry of OLEDs into the general lighting sector is predictable, since the small-area display market (e.g. for mobile phones) has already been flooded predominantly by AMOLED (Active Matrix OLED) displays [5].

Keeping in mind that about 15–20 % of the global electrical power is consumed by lighting applications [6], it is crucial to develop energy-saving, long-lived lighting technologies such as LEDs and OLEDs. Although the first commercial products for general lighting have been introduced by several companies [7], there is still much room for improvement in efficiency and lifetime. Furthermore, many physical effects, especially degradation processes, are not yet fully understood.

This thesis investigates the influence of photo-physical processes inside the OLED on the efficiency and the degradation processes under optical and electrical excitation. The main focus of this work lies on the study of excitonic processes inside the emitting system of multi-layered OLED stacks. Time-resolved optical spectroscopy allows for an analysis of the excitonic decay behavior under varying conditions. Therewith, it is possible to investigate energy transfer mechanisms from excited dye molecules to surface plasmon polaritons at an organic/metal interface and to other molecular species in the surrounding. Furthermore, it is possible to analyze quenching processes under electrical operation such as triplet-polaron-quenching (TPQ) and triplet-triplet-annihilation (TTA) by means of induced excited states lifetime changes. Moreover, this technique is a powerful tool to explore the temperature dependent behavior of the excitonic lifetime, energy transfer processes and the radiative quantum efficiency of organic thin films.

Based on this, an efficiency analysis method has been developed for state-of-the-art OLED stacks. Analyzing the energy dissipation of the excited molecules to the different optical modes, which are present in a microcavity-like structure such as an OLED, is important to understand the basic underlying (photo-)physical processes. In particular, the distance of the emitting molecules to the highly reflecting cathode of the devices can drastically change the effective radiative quantum efficiency of the emitting system and the extraction of light to the outside world. Investigating the influence of the cavity on the emitting molecules in terms of changes of the radiative rate is the basis

for the mentioned efficiency analysis. Hence, the basic approach will be first proofed and evaluated for simplified structures, and thereafter introduced to state-of-the-art OLEDs. Essential processes such as current density dependent changes of the radiative quantum efficiency and possible deviations from isotropic emitter orientation have been added to this method to achieve a consistent analysis of the power dissipation in OLEDs. Moreover, processes that are changing the radiative exciton fraction in fluorescent OLEDs will be taken into account resulting in a comprehensive investigation of all factors determining the external quantum efficiency. Furthermore, this method gives an innovative approach for investigation of OLED degradation during electrical operation by both electrical driven external quantum efficiency measurements and time-resolved photoluminescence spectroscopy. Therewith, it was, for the first time, possible to analyze the degradation induced changes of the factors determining the EQE of OLEDs almost separately from each other after an accelerated aging protocol. Moreover, the common assumption of an unchanged radiative rate of the emitting molecules during the degradation process was disproved for the OLED stack under investigation. This can be the basis for a more detailed analysis of aging effects in OLEDs for future investigations.

All together, this thesis will present an insight in the excitonic processes during OLED operation. With the obtained results, it could be possible to achieve a huge boost in efficiency and long-term stability by means of electrical degradation in future applications. The presented efficiency analysis should be a standard method for developing new OLED stacks. Additionally, the feature of non-isotropic emitter orientation will be pointed out. If the orientation of the transition dipole moments of the emitting molecules can be influenced to lie in the preferred substrate plane of the OLED, a boost in efficiency up to 50 % can be reached without any expensive threatments. However, the determination of the present emitter orientation and the corresponding radiative quantum efficiency (as a function of the current density) of the emitting system is a crucial point for device optimization. If both variables are not taken into account properly, the device optimization in terms of layer thickness adjustment can be erroneous and hence suboptimal device performance would follow.

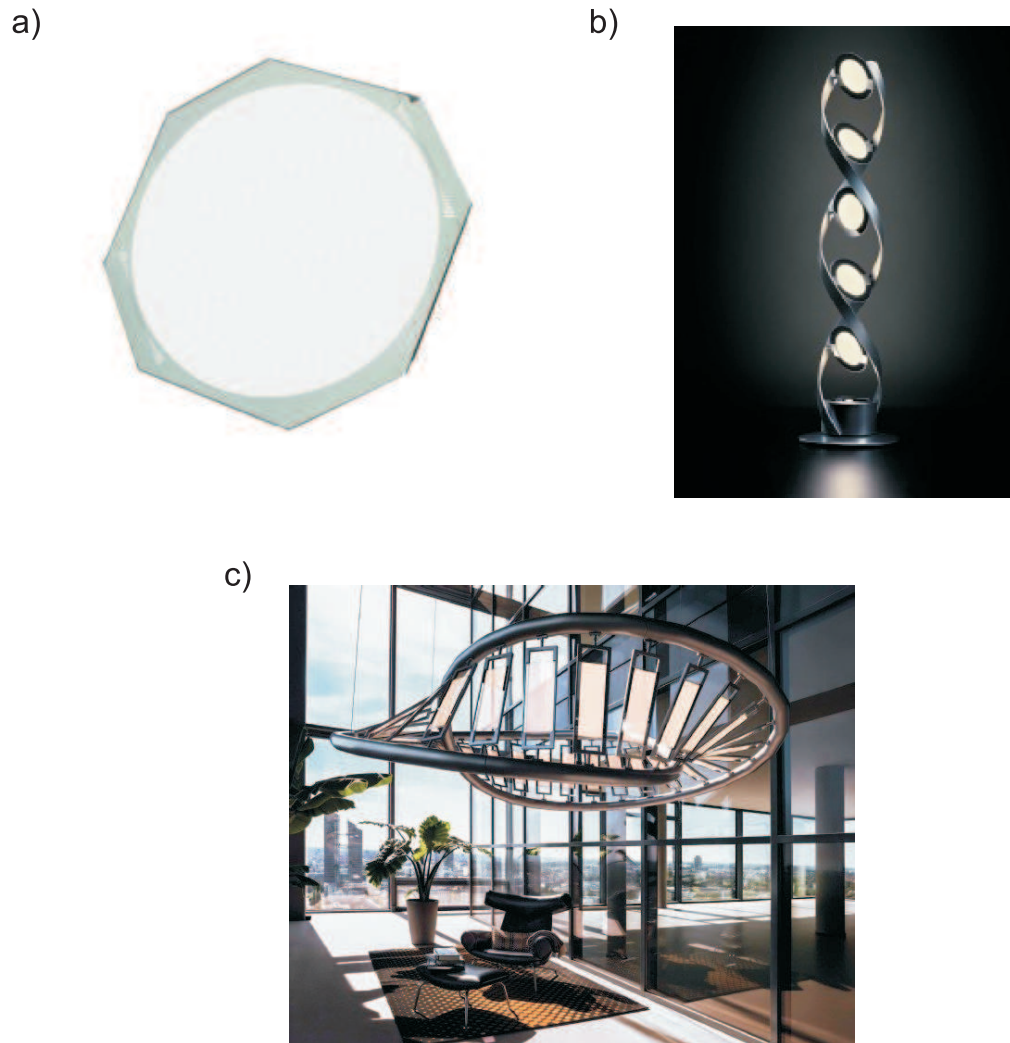


Figure 1.1: Commercial applications from OSRAM OS. a) Orbeos OLED panel with an active area of 49 cm^2 [8]. b) PirOLED luminaire combining inorganic with organic LEDs [9]. c) Rollercoaster luminaire using transparent OLEDs [10].

CHAPTER 2

BASIC PRINCIPLES OF ORGANIC LIGHT-EMITTING DIODES (OLEDs)

This chapter explains the basic processes and phenomena that are relevant for organic light-emitting diodes. First, the physics of organic semiconductors will be picked up. Starting with an overview about this material class a detailed consideration on both optical as well as electrical properties will follow. Please note, that this part is based on Refs. [11] and [12]. Subsequently, the working principles, in particular device operation mechanisms and efficiency determining factors of OLEDs, will be discussed. Thereafter, the optical modulation of micro-cavity like structures will be illustrated, including a detailed examination of the optical modes of an OLED and a brief sketch of the numerical simulation tool used in this thesis.

2.1 Organic semiconductors

In solid states physics it is convenient to distinguish between three different material classes by means of electrical and optical properties: metals, semiconductors and insulators. They are defined by the value of their energy band gap between valence and conduction band and by the position of the Fermi energy. Organic semiconductors are small molecules or polymers with a delocalized π -electron system in which the molecular bonding orbitals are fully filled with electrons [11]. The anti-bonding molecular orbitals are not occupied in the electronic ground state of the molecule. Hence, there exists an energy gap between the highest occupied molecular orbital (HOMO) and the lowest

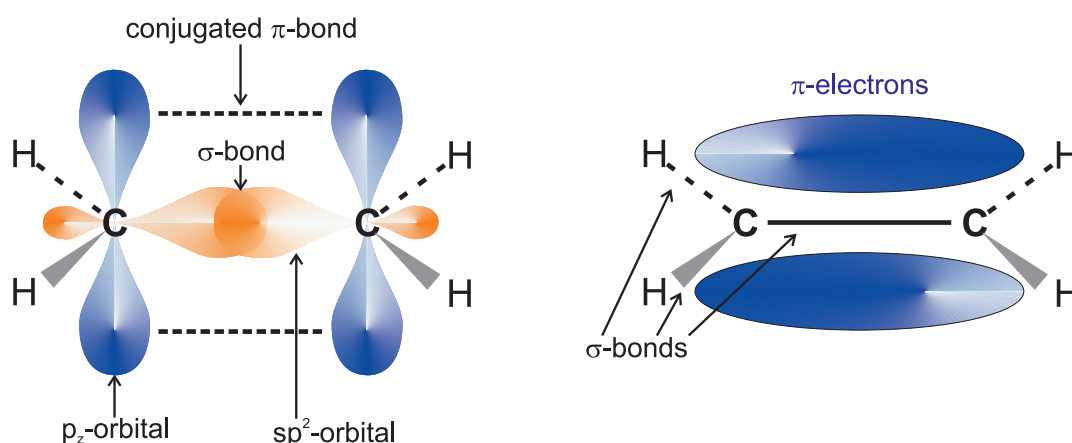


Figure 2.1: Schematic formation of a double bond between the two carbon atoms in the ethene molecule. The σ -bond between two sp^2 -hybrid orbitals of the carbon atoms are colored in orange, conjugated π -bonds in blue. The bonds between the carbon atoms (sp^2 -hybrid orbitals) and the hydrogen atoms (s-orbitals) are denoted by gray triangles and dashed diagonal lines.

unoccupied molecular orbital (LUMO) typically in the range of a few eV [12]. Thus, most organic materials used in this work are acting as insulators or semiconductors. Compounds with a metallic(-like) character do also exist, but are not subject of this thesis and will not be discussed.

The isolated carbon atom with its six electrons exhibits an electronic configuration of $1s^2 2s^2 2p^2$. If a carbon atom forms a covalent bond with another partner, i.e. another carbon atom, the electronic configuration changes to $1s^2 2s^1 2p^3$. Due to the occupied third p-orbital of the carbon atom it is possible to form hybrid-orbitals. Typically, the carbon atoms that are composing organic semiconductors are forming sp^2 -hybrid-orbitals [12]. Therefore, the $2p_x$ -, $2p_y$ - and $2s$ -orbitals are forming three new hybrid-orbitals, which are lying in one plain with an angle of 120° between them. Perpendicular to these three orbitals remains the p_z -orbital. Figure 2.1 shows a schematic sketch of the formation of a double bond between two sp^2 -hybridized carbon atoms consisting of one σ - and one π -connection. Therefore, the three sp^2 -hybrid orbitals are forming localized σ -bonds, while the remaining p_z -orbital is forming a π -bond. The electrons, that are involved in the π -bond of the carbon atoms are localized above and below the binding plain of the σ -bonds and have a smaller binding-energy than the direct overlapping σ -electrons. Therefore, the bonding π -electrons are creating the HOMO of the organic molecule, while the anti-bonding π -orbitals are forming the LUMO. Due to the geometric alignment of the sp^2 -hybrid-orbitals, organic materials that consist of more than six carbon

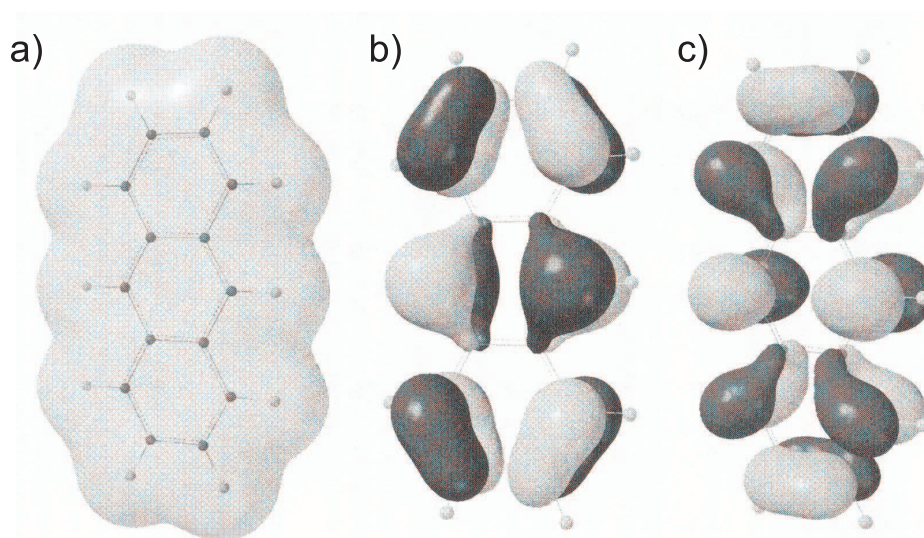


Figure 2.2: The anthracene molecule. a) Electronic configuration, b) HOMO and c) LUMO. (Graphic taken from Ref. [11].)

and hydrogen atoms are often forming a hexagonal structure in which the π -electrons are delocalized over the whole molecular ring. Figure 2.2 shows the complete electron distribution of the anthracene molecule ($C_{14}H_{10}$) and the positions of the HOMO and the LUMO of the molecule.

The interaction energy between different molecules in an organic crystal is only very weak compared to their inorganic counterparts. The fundamental interaction between the molecules are van-der-Waals forces [11]. Therefore, optical and energetic properties of an isolated molecule do not differ very strongly from the molecules in the solid state. The major difference lies in a shift to lower energies and a broadening of the emission spectrum. A detailed discussion of the optical properties of organic semiconductors will be given in the next section of this chapter.

2.1.1 Optical properties

The basic optical energy conversion processes of an organic molecule or an organic solid are shown in Fig. 2.3. Optical excitation of the ground state electrons in the π -orbital (HOMO; S_0) mainly leads to an occupation of the first excited singlet state (S_1) of the molecule, if the energy of the incoming photons is high enough. Singlet states have a spin multiplicity of 1, resulting from a pairwise anti-parallel orientation of the electronic spins. An excitation to energetically higher singlet states (S_2 , S_3 , S_4 , ...) is also possible,

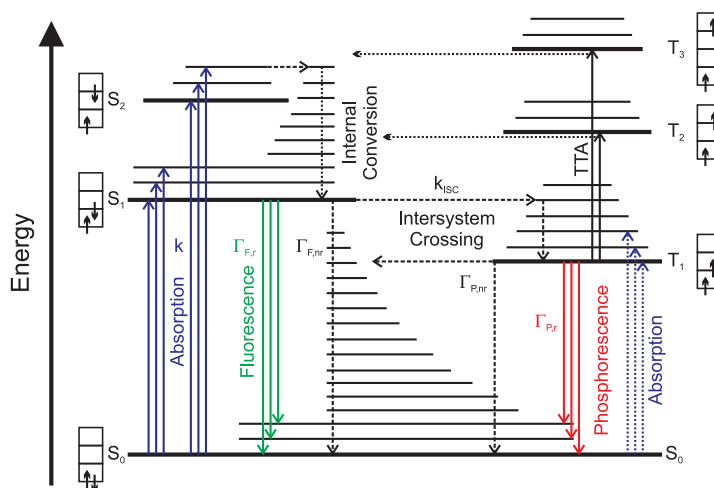


Figure 2.3: Energy level scheme of an organic molecule [11,12]. Solid, colored vertical arrows represent radiating optical processes, e.g. absorption and emission. Dashed vertical arrows are illustrating radiation-less processes. Solid, black vertical combined with dashed horizontal arrows describe the possible fusion of two triplets forming one excited singlet and one ground state (triplet-triplet-annihilation). Thick horizontal lines are electronic energy levels of the molecule. Thereby, S_0 is the energetic ground state of the molecule, which is occupied with two π -electrons with anti-parallel spins. S_1 and S_2 denote the first and the second excited singlet level, respectively. T_1 , T_2 and T_3 refer to the first three excited triplet states of the molecule, where the spins of the both electrons are oriented in parallel. The orientation of the electronic spins are indicated in the boxes next to each energy level. Thin horizontal lines are vibrational sub levels of the electronic states. Blue, solid arrows represent the absorption of light from the ground state to an excited singlet state. k indicates the rate of absorption. Blue, dotted lines show a potentially direct transition from the S_0 to an excited triplet state, which is normally forbidden by selection rules. Green arrows refer to light emission from the first singlet state S_1 , the so called fluorescence, while red arrows stand for the emission from the first excited triplet state, the phosphorescence. Dashed, vertical arrows from both first excited electronic states represent non-radiative decay channels. The radiative and non-radiative rates of the fluorescence and the phosphorescence are denoted as $\Gamma_{F,r}$, $\Gamma_{F,nr}$, $\Gamma_{P,r}$ and $\Gamma_{P,nr}$, respectively. Internal conversion describes the process that the energy of higher excited states is dissipated immediately after excitation to vibrational sub states of the first excited level. Intersystem crossing (ISC) characterizes the non-radiative energy transfer from a singlet to a triplet state under a flip of the electronic spin.

but these states do normally not decay radiatively, but rather relax to the S_1 state by a very fast non-radiative internal conversion process [11]. Strictly speaking, the absorption of light is depending on the symmetry of the electronic wavefunctions of the states.

Hence an excitation from e.g. S_0 to S_2 is typically forbidden. However, the emission of light during the recombination of the electron from the first excited singlet state to the ground state of the molecule is called fluorescence and exhibits a typical lifetime of a few to some ten nanoseconds.

Excited states with a spin multiplicity of 3, resulting from pairwise parallel oriented electronic spins are called triplet states. Triplet states of a molecule exhibit always a lower excitation energy than their singlet counterparts due to their different wavefunction and short coulomb radius of the exciton. However, the radiative decay from the triplet state to the singlet ground state is strictly forbidden by quantum mechanical selection rules, if no spin-orbit coupling is present in the molecule [11]. Hence, the triplet emission of molecules consisting purely of carbon and hydrogen atoms is very weak due to the very small spin-orbit coupling of the lightweight carbon atoms. Only if heavy (metal) atoms with a strong spin-orbit coupling are introduced to the molecules, it is possible to detect an intense emission from the triplet state called phosphorescence, with an excited states lifetime – depending on the strength of the spin-orbit coupling – of some μs to several ms. Strictly speaking, the direct optical excitation from the ground to the triplet states is forbidden, too, but again the spin-orbit coupling of the molecules could weaken this selection rule. Nevertheless, the predominant process in molecules with strong spin-orbit coupling is a different one. Typically, the optical excitation is a singlet transition. After the excited electron is relaxed to the S_1 by internal conversion, a process called intersystem crossing (ISC) takes place. Due to the ISC the electron is transferred from the S_1 to the energetically lower T_1 with an induced spin flip. This process is only weak for small, but can be very pronounced for strong spin-orbit coupling, exhibiting a transition time in the range of picoseconds.

Another process shown in Fig. 2.3 is the triplet-triplet-annihilation (TTA) represented by solid, black vertical arrows combined with dotted horizontal lines in Fig. 2.2. Thereby, two triplet states are fused creating an energetic ground state (S_0) and a higher excited singlet state. It should be noted that this process consists of two steps, the fusion and the induced spin-flip of the newly created excited state. For fluorescent emitters, for which the phosphorescence is only very weak, this process leads to a delayed fluorescence with a long lifetime of some μs [13]. For phosphorescent emitters this process is an important quenching process especially in OLEDs driven at high current densities, as will be explained in detail in section 2.2.2. The rates of absorption (k), the radiative (Γ_r) and the non-radiative (Γ_{nr}) decay are depending on the overlap of the wavefunctions of both states determined by the transition matrix element:

$$P_{i \rightarrow f}^2 \propto |\langle \Psi_f | \vec{p} | \Psi_i \rangle|^2 \propto |\langle \Psi_{el,f} | \vec{p} | \Psi_{el,i} \rangle|^2 \cdot |\langle \Phi_{vib,f} | \Phi_{vib,i} \rangle|^2 \cdot |\langle \chi_{spin,f} | \chi_{spin,i} \rangle|^2. \quad (2.1)$$

It can clearly be seen, that a transition between two different excited states is forbidden, if only one of the three factors becomes 0. The meaning of the different factors for the selection rules for an electronic transition will be discussed in detail in the following. In this equation $\vec{p} = e \cdot \vec{r}$ represents the dipole operator and $\vec{M} = \langle \Psi_f | \vec{p} | \Psi_i \rangle$ is the so called transition dipole moment between two electronic states in the molecule. Therefore, the transition is only allowed if the parity of the wavefunctions of the two states is different, what is typically fulfilled between the HOMO and the LUMO of an organic molecule. The second factor of Eq. 2.1 contributes to the fact that usually vibrations of the molecular backbone are involved in electrical transitions. The intensity distribution of the excitation and the emission spectra is determined by the Franck-Condon principle. Thus, only vertical electronic transitions, as shown in Fig. 2.3, are allowed at all. Furthermore, vibrational states with a large wavefunction overlap are preferred, as can be seen by the factor $|\langle \Phi_{vib,f} | \Phi_{vib,i} \rangle|^2$ in Eq. 2.1. In addition, a fast relaxation of higher excited vibronic states to the vibronic ground state takes place. From this it follows, that due to the so called Kasha's rule, no emission from higher excited electronic states is detectable, because the excitation energy is coupled to higher vibrational states of the first excited electronic state, which on the other hand suffer a fast relaxation to their vibronic ground state. Hence, the emission and absorption spectra of organic molecules exhibit a typical vibronic structure and mirror symmetry, as it is shown as a sketch in Fig. 2.4.

The last factor of Eq. 2.1 describes the spin selection rules of the electronic transition. The ground state of an organic molecule is usually a singlet state. The wavefunction of a singlet state (ground state or excited state) exhibit the spin multiplicity 1, and is therefore not degenerate. The schematic wavefunction of this state can be written as:

$$\chi_S = \frac{1}{\sqrt{2}} (|\uparrow_1 \downarrow_2\rangle - |\downarrow_1 \uparrow_2\rangle). \quad (2.2)$$

The triplet state with its spin multiplicity of 3 is three fold degenerate (in the absence of a magnetic field) and the three different schematic wavefunctions can be written as:

$$\chi_T = \begin{cases} |\uparrow_1 \uparrow_2\rangle \\ \frac{1}{\sqrt{2}} (|\uparrow_1 \downarrow_2\rangle + |\downarrow_1 \uparrow_2\rangle) \\ |\downarrow_1 \downarrow_2\rangle \end{cases}. \quad (2.3)$$

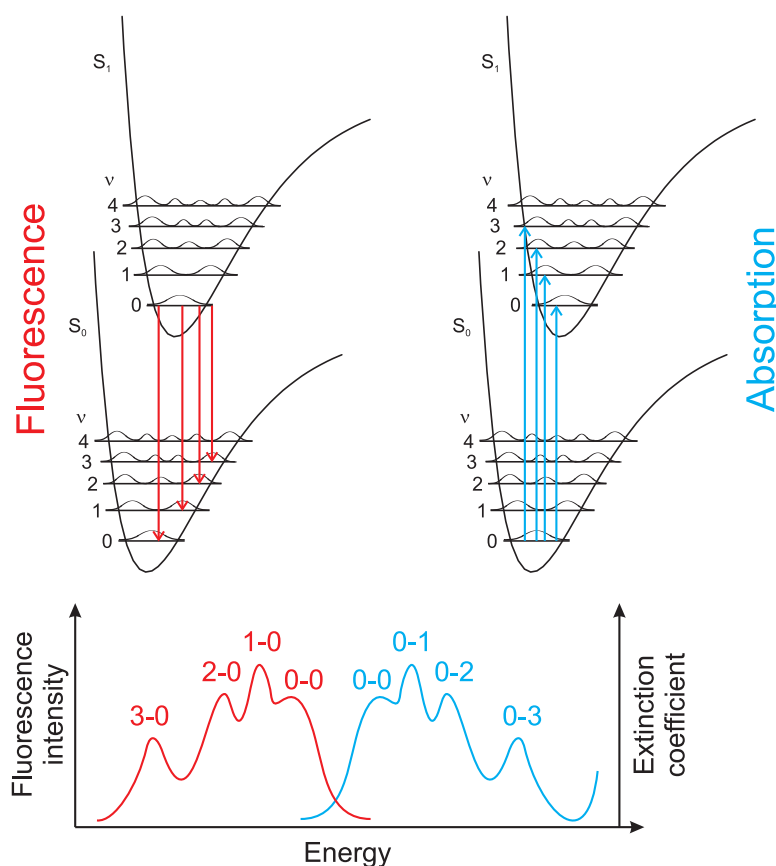


Figure 2.4: Mirror symmetry and the Stokes shift between absorption (blue) and emission (red) spectra between the S_0 and the S_1 state of an organic molecule. Vibrational transitions are denoted with numbers, e.g. 0-1 for the transition between the vibrational ground state of S_1 to the first vibronic state of S_0 and so on.

Hence, a transition between different spin multiplicities is strictly forbidden. However, if a strong spin-orbit coupling is present in the organic molecule, no pure singlet or triplet states are existing, but a linear combination of both states occurs. Thus, a transition between singlet and triplet states (ISC, phosphorescence) becomes allowed and is very strong for organic molecules consisting of heavy metal (central) atoms as Iridium or Platinum with organic ligands [14]. This type of molecules are called phosphorescent emitters and are often used in organic light-emitting diodes, as will be discussed in section 2.2.2.

It should be noted that it is possible to observe an electronic excitation of organic molecules with an energy lower than the HOMO-LUMO gap [11]. This effect is based on the Coulomb binding of the created electron-hole pair. An exciton corresponds to a hydrogen-like binding of an electron and a hole in a solid. There are existing three

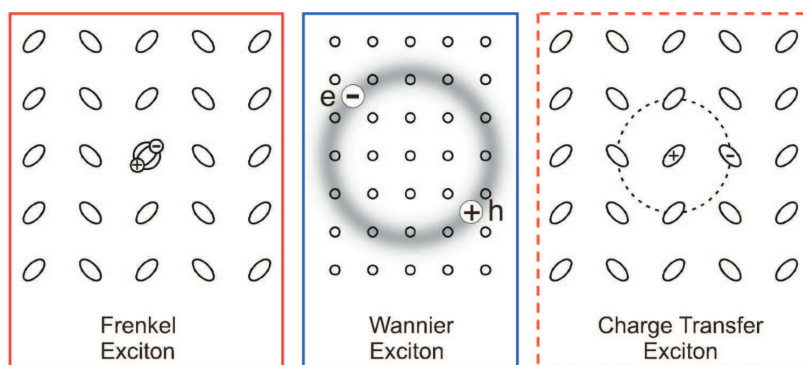


Figure 2.5: The three different types of excitons (from left to right): Frenkel, Wannier and Charge transfer exciton. (Graphic taken from Ref. [11].)

different types of excitons which are displayed in Fig. 2.5: Charge transfer, Wannier and Frenkel excitons [11]. Charge transfer excitons play an important role in organic photovoltaic cells (OPVCs), because it is defined as the excited state in which hole and electron are located on adjacent molecules, typically of a different species. The molecules on which the hole or the electron are located in OPVCs are denoted as donor or acceptor, respectively. Charge separation in OPVCs occurs at donor/acceptor interfaces via an intermediate charge transfer state. The second exciton type is the so-called Wannier exciton. This is the prevailing type of excitons in inorganic semiconductors. Wannier excitons are weakly bound electron-hole pairs with a large radius of several nanometers. In organic semiconductors, especially in organic light-emitting diodes, the dominant exciton type is the Frenkel exciton. Frenkel excitons are localized on one molecule and exhibit a strong coulomb binding with a radius in the range of a few nanometers and a binding energy of 0.1 to 1 eV. Therefore, an optical excitation with an energy lower than the HOMO-LUMO gap is possible. Figure 2.6 shows the coulomb potential for excitons in organic and inorganic semiconductors. It can clearly be seen, that a dissociation of an exciton in organic semiconductors cannot occur due to the thermal energy at room temperature, while excitons in inorganic semiconductors have a much lower binding energy than $k_B T$ and so can be dissociated very easily. Furthermore, this is one reason why the spin of the excitons plays an important role in organic solids and is almost negligible in their inorganic counterparts.

One crucial point in organic light-emitting diodes is the energy transfer process between different molecules. One can distinguish between two different transfer mechanisms, the Förster and the Dexter or Marcus energy transfer [11]. The Förster mechanism describes the long-range (up to ≈ 10 nm) transfer of an exciton by a non-radiative dipole-dipole coupling between a donor and an acceptor molecule. Thereby, it is essen-

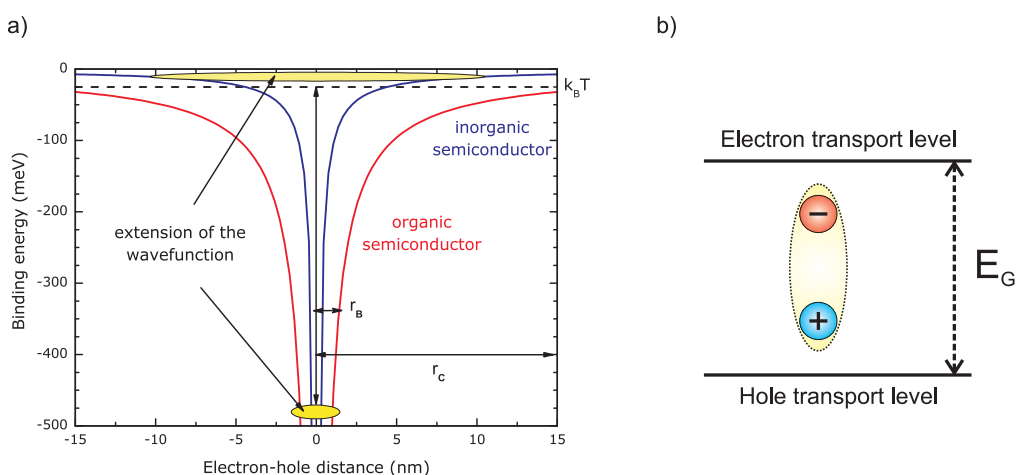


Figure 2.6: a) Coulomb potential and binding energies for excitons in organic and inorganic semiconductors. r_B denotes the radius of the exciton, while r_C represents the coulomb radius at which the binding energy is in the range of $k_B T$. b) An exciton in an organic semiconductor is energetically located inside the bandgap due to the high binding energy of the hole and the electron.

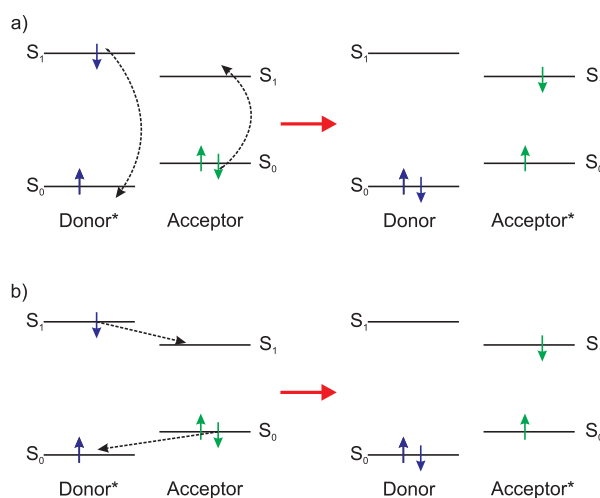


Figure 2.7: a) Förster and b) Dexter transfer processes of excitons from a donor to an acceptor molecule.

tial that the emission spectrum of the donor overlaps with the absorption spectrum of the acceptor molecule. The Dexter, or also called Marcus energy transfer mechanism represents the direct hopping of two electrons from one molecule to an adjacent acceptor molecule. Hence, this transfer process requires an overlap of the electron wavefunctions and thus exhibits only a very small range of a few angstroms. Both transfer processes are shown as a sketch in Fig. 2.7.

2.1.2 Electrical properties

The drift-diffusion-model describes the motion of charge carriers through a solid state body. Therefore, the current density is given by:

$$j = qnv = qn\mu F. \quad (2.4)$$

Therein, j represents the current density that is defined as the total current I per involved area A , q is the elementary electric charge and v describes the drift velocity of the charge carriers. The drift velocity is depending on the charge carrier mobility μ and the applied electrical field F . In general, the charge carrier mobility shows a nonlinear behavior and depends on the charge carrier density n , the temperature T and effective electric field F . The intrinsic (free) charge carrier density in semiconductors is given by

$$n = N_0 \cdot e^{-E_g/(2k_B T)}. \quad (2.5)$$

In the case of organic semiconductors, N_0 represents the density of organic molecules, E_g stands for the HOMO-LUMO-gap and $k_B T$ describes the thermal energy depending on the temperature T and Boltzmann's constant k_B . Calculating the intrinsic density of free charges that can take part in the electrical current at room temperature ($T \approx 300$ K) for a typical organic molecular solid with $E_g \approx 2.5$ eV and a molecular density of $N_0 = 10^{21} \text{ cm}^{-3}$ yields a very low value of the order of $n = 1 \text{ cm}^{-3}$. This is several orders of magnitude lower than characteristic charge carrier densities of their inorganic counterparts ($n_{\text{Si}} \approx 10^9 \text{ cm}^{-3}$). Thus, only very low currents are achievable if no additional free charge carriers are created due to secondary treatments such as photo generation by light absorption, injection of charge carriers from contacts, the field-effect or (electro-)chemical doping of the organic solids [15]. In the case of organic light-emitting diodes the most interesting processes are the injection of charge carriers from electrodes and the (electro-)chemical doping of the used organic layers.

Charge carrier injection

Figure 2.8 illustrates the simplified energetic scheme of an organic layer sandwiched between two metallic electrodes, the anode and the cathode, injecting holes and electrons, respectively. Without an applied external voltage, no charge carriers are injected into the organic layer due to reverse bias conditions. This is due to the different work functions of the electrodes and the energy alignment of Fermi and vacuum energies, if they are connected with the organic semiconductor resulting in a built-in potential Φ_{bi} . Hence, the flat band condition of the organic layer is achieved if an external potential as high

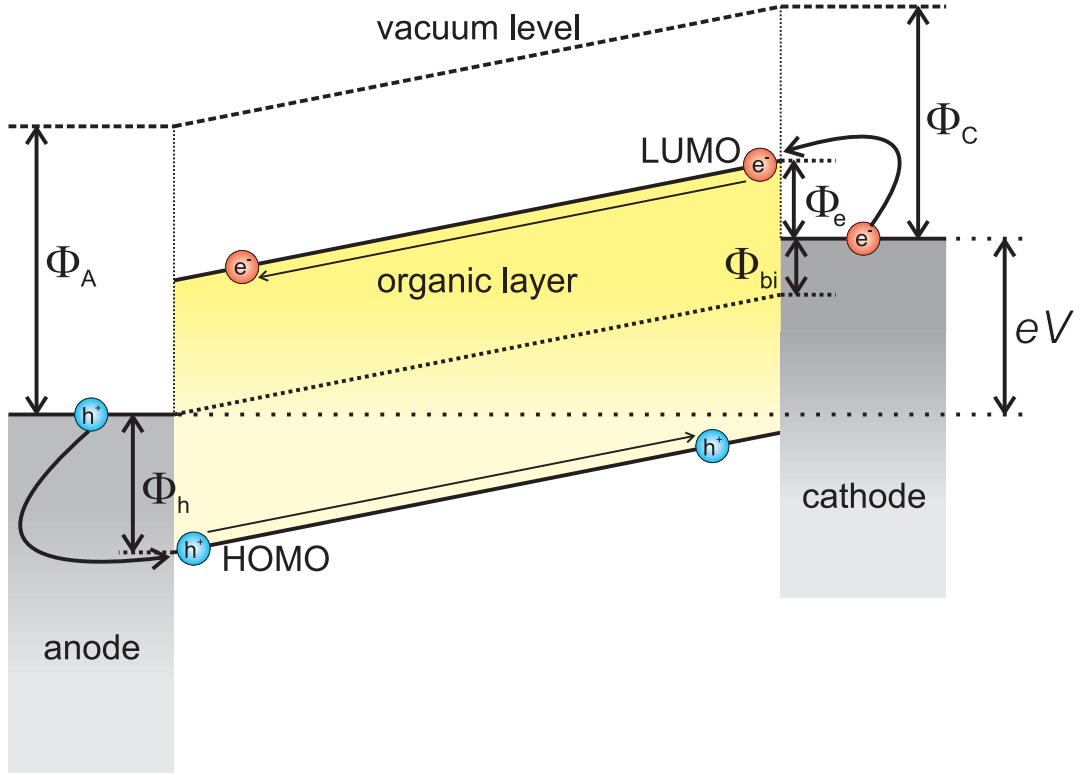


Figure 2.8: Simplified energetic sketch of an organic layer sandwiched between an anode and a cathode. Charge carrier injection occurs from both electrodes due to an applied voltage V . Injection barriers are denoted by Φ_h and Φ_e for the holes injected from the anode into the HOMO level of the organic layer and electrons injected from the cathode into the LUMO level, respectively. The difference between the work function of the anode (Φ_A) and of the cathode (Φ_C) determines the built-in potential ($\Phi_{bi} = e \cdot V_{bi}$). Charge carrier injection starts for voltages higher than V_{bi} .

as the internal potential Φ_{bi} is applied to the electrodes. The required voltage (V_{bi}) is defined as the built-in voltage and can be described by the difference of the work functions of the electrodes, Φ_A and Φ_C for the anode and the cathode, respectively:

$$V_{bi} = \frac{1}{e} \cdot (\Phi_A - \Phi_C), \quad (2.6)$$

with e being the elementary charge. Therefore, charge carrier injection from the electrodes appears for applied voltages higher than the built-in voltage ($V \geq V_{bi}$) as shown in Fig. 2.8.

The injection barriers for the holes and the electrons from the electrodes into the organic layer are defined by the energetic positions of the Fermi energy of the metals and the HOMO and LUMO levels of the organic with respect to the vacuum energy, respectively:

$$\Phi_h = E_{\text{HOMO}} - \Phi_A \quad (2.7)$$

$$\Phi_e = \Phi_C - E_{\text{LUMO}}. \quad (2.8)$$

In order to minimize the injection barriers for the charge carriers it is mandatory to choose electrodes, whose work functions are close to the HOMO energy level of the organic material for the injection of holes from the anode and close to the LUMO for the injection of electrons from the cathode, respectively.

Charge carrier transport

The charge carrier transport in perfect organic crystals and organic thin films is following two different concepts. While in perfect crystals band transport comparable to the charge carrier transport in inorganic semiconductors is the prevailing mechanism, the appearance of thermally activated hopping transport between localized molecules can be observed in organic thin films [11]. Because organic light-emitting diodes are consisting of thin organic (often amorphous) layers, only the approach of a hopping process of charge carriers between localized sites will be discussed in the following.

The hopping transport describes the motion of a charge carrier due to an applied field from one localized energy level to a neighboring one [16]. In thin organic layers, the molecular energy levels are not constant with respect to the vacuum level, due to a statistical alignment of the molecules during film growth. Thus, both the HOMO and the LUMO levels can be shifted to lower or higher energies due to interaction with the surrounding molecules and therewith, even the energy gap of the single molecules can be changed [17–20]. Hence, energetic disorder of the energy levels is apparent and thereby the hopping possibility between two adjacent molecules can vary strongly. Figure 2.9 illustrates the energetic situation in a thin organic film as a sketch. The HOMO and the LUMO energies of the molecular species are indicated with dashed lines. Due to the interaction with their surroundings the energy levels are shifted with respect to their intrinsic ones and a Gaussian energy distribution is assumed. The typical width of the energy distribution lies in the range of 75 to 100 meV [16]. Thus, the hopping of charge carriers has to be thermally activated in order to overcome the energetic

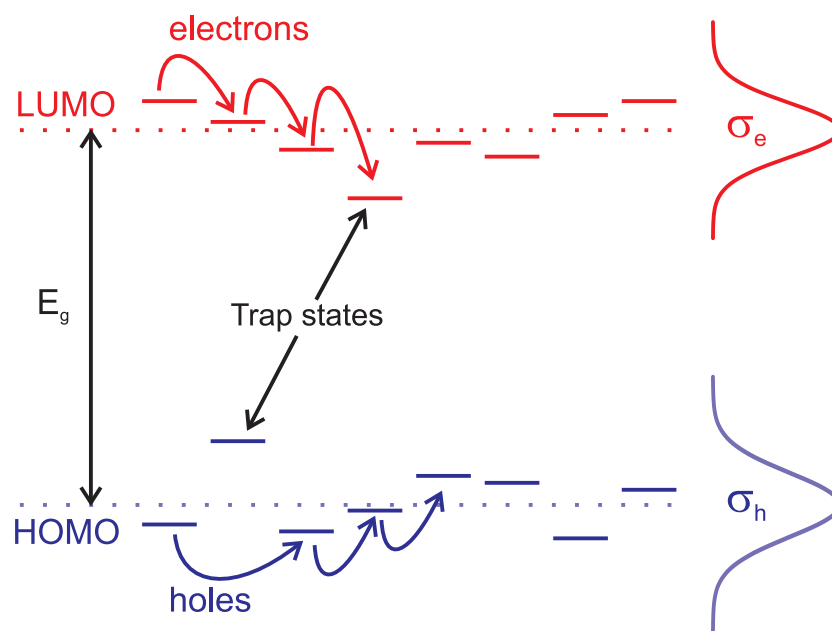


Figure 2.9: Schematic illustration of the hopping transport (arrows) of electrons and holes traveling in the LUMO and the HOMO of an organic molecular solid, respectively, for disordered energy levels with a Gaussian energy distribution. The width of the density of states is denoted by σ_e for the LUMO and σ_h for the HOMO. The energy gap of an isolated molecule is marked by E_g .

barriers between two localized sites and is drastically reduced for low temperatures. The hopping of charge carriers is indicated with arrows in Fig. 2.9. However, the energy level shift can be very pronounced for some molecules in an organic thin film, creating trap states for both types of charge carriers. If the LUMO of one molecule is drastically shifted to lower energies or the HOMO to higher energies, one is speaking of electron or hole traps, respectively. The presence of trap states is not only influencing the charge carrier conductivity in organic thin films, but can also influence the charge carrier recombination, and therewith the generation of light inside an OLED.

Strictly speaking, one has to distinguish between shallow traps, which are described by the mentioned gaussian energy distribution and deep traps, which typically result from impurities of the materials. However, this is beyond the scope of this thesis and will not be discussed in detail.

2.2 Organic light-emitting diodes

Organic light-emitting diodes are devices in which light emission due to an electrical current flow is induced by radiative recombination of the charge carriers inside an organic layer. The underlying process is the so-called electroluminescence, that is based on the recombination of injected charge carriers on an organic molecule forming an exciton. Afterwards, as discussed in the previous sections, this excited state can decay under radiation of light of a certain wavelength mainly depending on the molecular energy gap of the excited molecule. The first observation of electroluminescence from an organic solid was presented by Pope et al. in 1963 [1]. However, several thousand volts have been needed to detect a clear electroluminescence signal from the thick anthracene crystal. The first efficient, low-voltage driven OLED was later demonstrated by Tang and van Slyke in 1987 [2]. Their approach was using two thin organic layers deposited by vacuum evaporation. Hence, they achieved an external quantum efficiency (EQE) of about 1 % for voltages below 10 V. The first OLED based on polymers was fabricated using a spin-coating technique by Burroughes et al. in 1992 [3]. This fundamental research was the beginning of a new area in physics, the organic electronics. From this time on great efforts in this discipline have been accomplished yielding an efficiency record of 87 lm/W for a white OLED operated at 1.000 cd/m² in 2011 [4]. This efficiency is comparable to that of fluorescent tubes and marks the entry of OLEDs into the commercial application sector for general lighting.

2.2.1 Device operation

The simplest device structure of an OLED consists of only one organic layer sandwiched between two (metallic) electrodes [21]. Figure 2.10 illustrates the basic principles of such an one-layer OLED [11]. Holes and electrons are injected due to an applied voltage higher than the built-in voltage from the anode into the HOMO and from the cathode into the LUMO of the organic material, respectively. Due to the applied electrical field charge carriers are traveling from the electrodes towards each other and can then recombine under formation of an exciton inside the organic layer. The energetic levels for both charge carriers are shifted within the energy gap of the organic material due to the binding energy of the exciton. Finally, the exciton can decay under radiation of light and therewith electroluminescence from the organic molecules appears. However, due to the device layout comprising only one organic layer a huge amount of injected electrons and holes can reach the opposite electrode without recombining with each

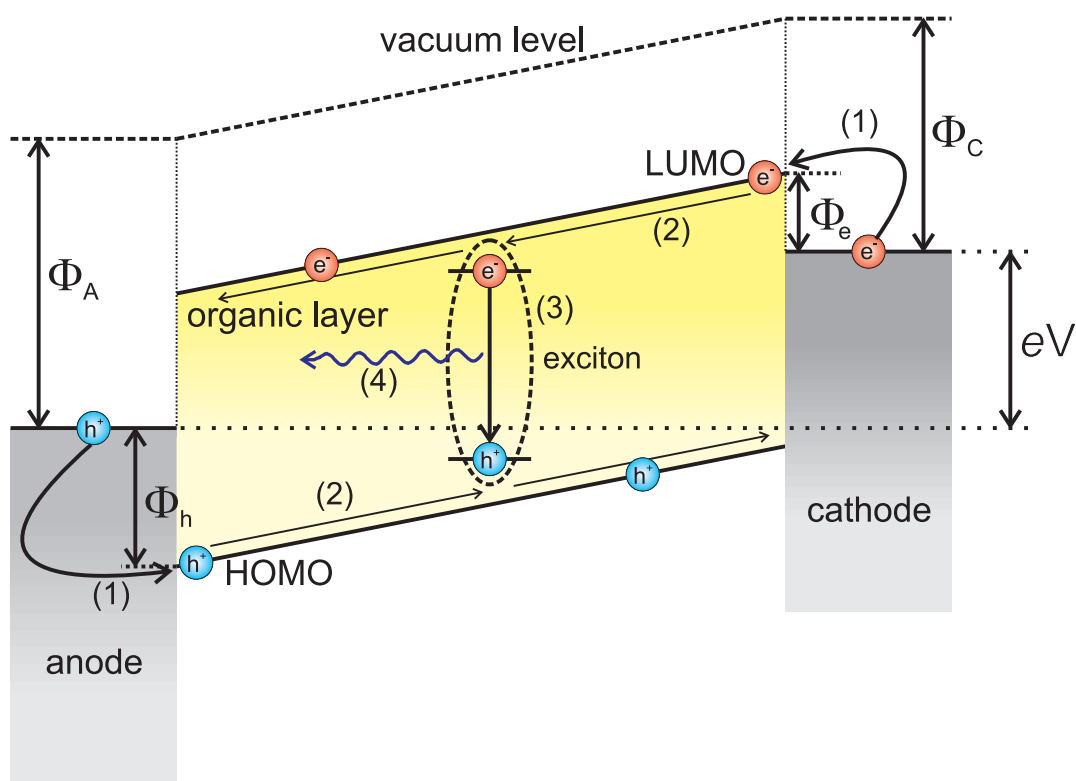


Figure 2.10: Simplified illustration of OLED device operation. Only one organic layer is sandwiched between an anode and a cathode. Applying a voltage higher than the built-in voltage of the device results in: (1) charge carrier injection from the electrodes, (2) transport of the electrons and holes following the applied electrical field, (3) recombination of the charges forming an excitonic state and finally (4) decay of the excited state under radiation of light.

other in the organic layer. Hence, these charge carriers are lost and do not contribute to light emission from the organic light-emitting diode, and therewith are reducing device efficiency. Furthermore, the emission zone is not fixed in such devices and can be spread over the whole device, especially near both contact interfaces resulting in quenching of excited states at the electrodes [22–24]. Moreover, the recombination zone can shift inside the organic layer with the applied voltage due to different injection barriers at the electrodes followed by variation of the emitted color and in efficiency of the device [23].

Thus, it is mandatory to use different layers that are tailored for their special function in modern OLEDs. Figure 2.11 illustrates the energy level diagram of the different organic layers for an ideal monochromatic OLED consisting of three organic layers. A semitransparent anode is subsequently covered by a hole transport layer (HTL), followed by the emission layer (EML) and an electron transport layer (ETL). Finally, a metallic cathode is deposited onto the device. Due to perfect energy alignment of the work func-

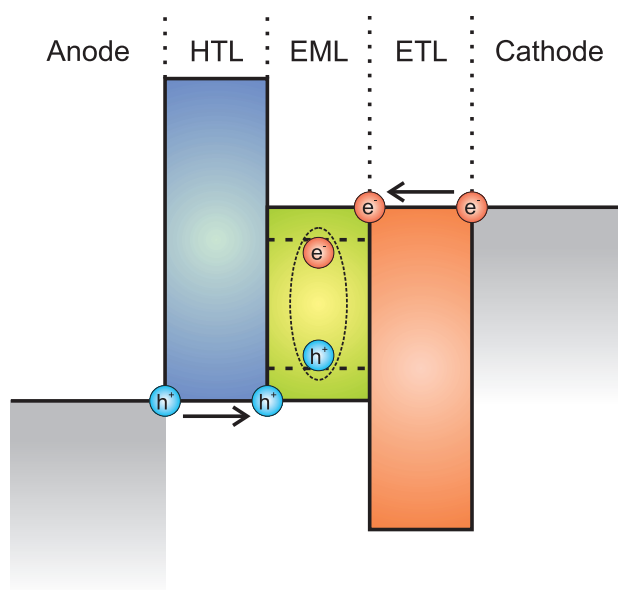


Figure 2.11: Schematic energy level diagram of the different organic layers for an ideal monochromatic OLED, if the built-in voltage is applied to the device. The acronyms are explained in the text.

tion of the anode and the HOMO level of the HTL, holes are injected instantly from the anode into the HTL if a voltage in forward direction is applied to the device. The same situation is present for electron injection from the metallic cathode into the LUMO of the ETL. A reasonable manner is a chemical conductivity doping of both transport layers to achieve a high conductivity [15]. Therewith, it is possible to optimize the thicknesses of the transport layers in terms of outcoupling efficiency enhancement without changing the electrical properties of the device [25–27]. This optimization process is discussed in detail later in chapter 5. Furthermore, it is important to use wide energy gap materials as transport layers to avoid absorption of light that is created inside the emission layer of the OLED. Additionally, both transport layers are also acting as charge carrier blocking layers [28]. As can clearly be seen from Fig. 2.11 the energy discrepancy of the LUMO levels of the EML and the HTL is strongly pronounced. Therefore, electrons that are traveling in the LUMO of the EML towards the EML/HTL interface cannot overcome this energy barrier and are blocked. The same situation is obvious for the holes at the EML/ETL interface due to a huge energy gap between both HOMO levels. Thus, charge carriers that are traveling in the EML of the device cannot reach the opposite charged electrode and remain in the EML until they are recombining under the formation of an exciton.

The emission layer of an ideal monochromatic OLED consists of a composite of two different organic materials, an emitter doped with some weight-percent into a matrix. Thus, the matrix material is solely responsible for the charge injection and the transport through the emission layer, while the emitting molecule is only contributing to the radiation of light. Therewith, the creation of excitons is separated from the charge transport as well as possible, and thus the undesirable interaction between an isolated charge carrier and a formed exciton is almost suppressed. Moreover, the excitons are separated from each other to prevent unwanted bimolecular processes. Another crucial point of energy alignment is that both, the HOMO and the LUMO level of the emitting species have to be located inside the energy gap of the matrix material. Hence, an effective trapping of charge carriers on the emitting molecules and therewith a good creation of excitons can take place. Nevertheless, also the energy transfer from excitons that are formed on the matrix to the emitting molecules (as described in section 2.1.1) is emphasized.

2.2.2 External quantum efficiency (EQE)

In terms of device physics the most important value of an OLED is its external quantum efficiency (EQE) that is given by the ratio between actually emitted photons (in the visible spectral region) from the device and the amount of injected charge carriers (see Fig. 2.12). The EQE of an OLED can be calculated using [29]

$$\text{EQE} = \gamma \cdot \eta_r \cdot q_{\text{eff}}(q) \cdot \eta_{\text{out}}. \quad (2.9)$$

The first factor of this equation (γ) represents the charge carrier balance of the device. It is determined by the fraction of formed excitons and injected charge carriers and can be brought close to unity if appropriate injection and blocking layers are used in the corresponding OLED in order to provide a balanced amount of both types of charge carriers [15, 30].

The second factor (η_r) is the so-called radiative exciton fraction and accounts for the fraction of generated excitons that are allowed to decay under radiation of light with respect to spin selection rules as already depicted in section 2.1.1. Therefore, if the EQE is measured for an electrically driven OLED, η_r becomes 1 for phosphorescent [31–33] and 1/4 for fluorescent emitting systems [34, 35], due to the formation of one singlet exciton per three triplet excitons.

Due to strong spin-orbit coupling induced by heavy metal atoms incorporated in phosphorescent emitting molecules, all excited singlet excitons are directly converted to the

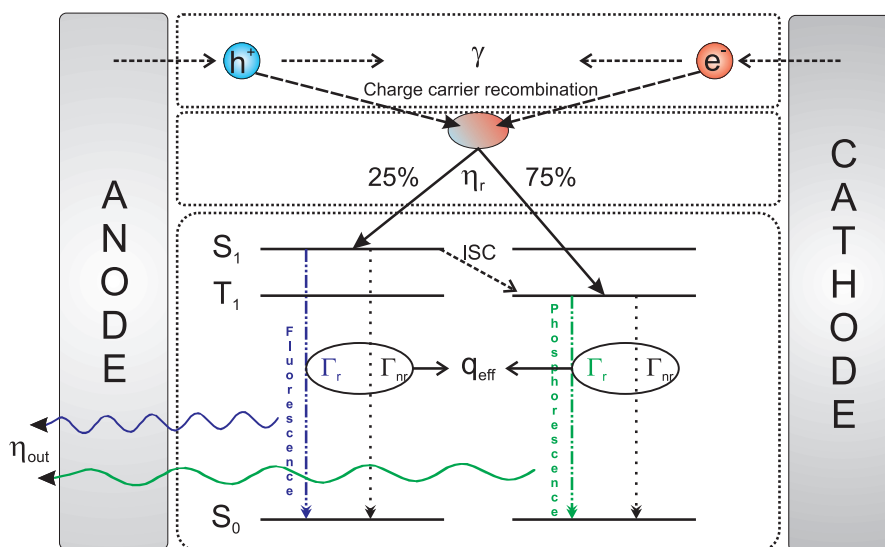


Figure 2.12: Schematic illustration of the different factors determining the external quantum efficiency of organic light-emitting diodes. The acronyms are explained in the text.

triplet state of the molecule due to the so-called intersystem crossing (ISC) process, resulting in a radiative exciton fraction of unity.

Strictly speaking, η_r is not totally fixed for fluorescent materials and can be increased by two different effects, triplet-triplet-annihilation (TTA) [36–39] and thermally activated delayed fluorescence (TADF) [40, 41]. Both effects are shown as a schematic sketch in Fig. 2.13. Molecules, showing strong TADF, exhibit only a small energy gap between the singlet and the triplet state. Therefore, not only intersystem crossing such as for phosphorescent materials appears but also the reverse intersystem crossing (RISC) that describes the thermally activated energy transfer from the triplet state (back) to the singlet of the molecule. This process can be very pronounced for energy gaps in the range of the thermal energy ($\approx 100 \text{ meV}$). Hence, triplet excitons are harvested and converted to singlets emitting at the same wavelength as the prompt fluorescence but with some orders of magnitude higher excited states lifetimes.

The second effect that is affecting the radiative exciton fraction in fluorescent emitting systems is triplet-triplet-annihilation. Here, two triplet excitons are interacting with each other forming one excited singlet state and one ground state of the molecule. Due to the very weak transition from the triplet to the ground state in fluorescent materials, triplet excitons exhibit very long excited states lifetimes resulting in a high TTA probability, that can remarkably increase the radiative exciton fraction [13]. The emission resulting from TTA shows, such as for TADF, the same spectrum as the prompt fluorescence but the excited states lifetime of this delayed emission is, again, some orders

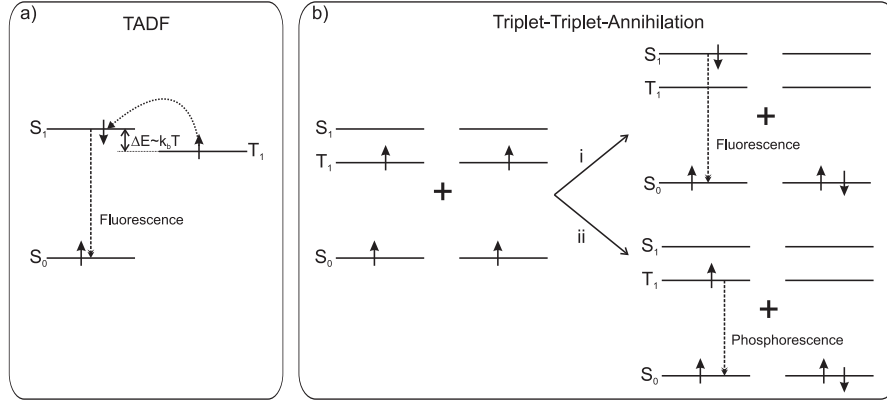


Figure 2.13: Schematic illustration of the two effects influencing the radiative exciton fraction in fluorescent materials. a) Thermally activated delayed fluorescence (TADF) and b) the bimolecular triplet-triplet-annihilation, where (i) describes the delayed fluorescence with an enhanced radiative exciton fraction and (ii) illustrates the decrease of the effective radiative quantum efficiency of a phosphorescent emitting system.

of magnitude higher.

The third factor determining the external quantum efficiency of organic light-emitting diodes is the effective radiative quantum efficiency, which is a function of the intrinsic radiative quantum efficiency (RQE) - often denoted as q - for an infinite layer of the emitting system. However, the quantum efficiency of an emitting system is changed due to its surrounding, especially if the emitter is embedded in a microcavity such as an OLED [23, 25, 42]. The intrinsic radiative quantum efficiency of an emitting system is determined by its radiative and non-radiative decay rates, Γ_r and Γ_{nr} , respectively, and is given by:

$$q = \frac{\Gamma_r}{\Gamma_r + \Gamma_{nr}}. \quad (2.10)$$

This equation is only valid for low excitation densities (to avoid e.g. bimolecular processes) and an infinite bulk of the emitting system. If the emitting species is embedded in a microcavity (or if interfaces are adjacent), such as an OLED, the radiative rate of the emitting molecules is changed by the so-called Purcell effect [43], resulting in an effective RQE given by:

$$q_{\text{eff}} = \frac{F \cdot \Gamma_r}{F \cdot \Gamma_r + \Gamma_{nr}}. \quad (2.11)$$

Therein, F represents the Purcell factor, that is only influencing the radiative but not the non-radiative rate of the emitter, and can be larger or smaller than unity [44–46].

Therefore, the effective RQE of an emitting system inside an OLED cavity can be increased or decreased compared to the intrinsic one. Moreover, the effective RQE can be strongly influenced by quenching effects during electrical operation. Especially at high current densities, TTA and triplet-polaron-quenching (TPQ) can drastically reduce the effective RQE if the emitting species is a phosphorescent molecule [47–49]. The mechanism of TTA is already shown as a schematic sketch in Fig. 2.13. Unfortunately, TPQ is a more complex phenomenon based on a shift of the energy levels of molecules adjacent to a charged state and the exact underlying mechanism will not be discussed in detail. For fluorescent materials, singlet-polaron-quenching (SPQ) or singlet-singlet-annihilation (SSA) are only very weakly pronounced due to the comparably short excited states lifetimes and can typically be neglected. However, introducing an effective RQE for the emitting system is mandatory in terms of device optimization by layer thickness adjustment, as will be discussed in detail later.

The last factor determining the EQE is the so-called outcoupling factor of the device, η_{out} . It is defined as the ratio of photons that can reach the surrounding media (air) of the OLED to the total amount of generated photons inside the device. Due to the multi-layered stack layout and the used materials this factor is typically in the range of 15–20 % for bottom-emitting OLEDs using isotropically oriented emitting systems. The rest of the generated power cannot escape the OLED structure to the outside world and is trapped in substrate modes or waveguided modes in the organic layers [50,51], or is dissipated from the emitting molecules by near-field coupling to surface plasmon polaritons (SPPs) at the metal/organic interface [22,52]. Substrate and waveguided modes originate from total internal reflection due to mismatch of the refractive indices at the air/substrate and the substrate/organic (including the anode) interface, respectively.

However, the outcoupling factor can strongly be influenced by orientation effects of the emissive dipole moments of the emitting species due to changes in power dissipation into the different optical modes of an OLED [53]. Thus, it is mandatory taking emitter orientation, a well-known phenomenon for polymeric emitters [54,55], into account for OLEDs based on dye-doped small molecules, too. Recent studies have shown the existence of both, fluorescent and phosphorescent oriented dye-doped emitting systems influencing the efficiency analysis in terms of optical simulations [56–58]. If this feature is not considered in an adequate way, the simulations would be erroneous resulting in wrong estimations of the outcoupling efficiency and therewith of the effective RQE of the emitting system [59] and, in the case of fluorescent emitters, the radiative exciton fraction of the device. A detailed discussion of the energetic coupling of the emitting molecules to the different optical modes of an OLED will be given in the next section.

2.3 Optical modeling

A powerful tool for understanding optical losses in organic light-emitting diodes is the modeling of power dissipation channels and the combination of these models with numerical simulations. This section describes the optical loss channels in multi-layered microcavity-like structures, such as OLEDs, and gives a rough overview over the simulations used in this thesis. It should be noted, that the simulation tool was not developed by the author of this thesis and hence only the basics of the physical background are presented without concrete discussions of the underlying algorithms or programming language. For more informations about simulation tools, please check the PhD theses of Nils Reinke [60], Stefan Nowy [61], Jörg Frischeisen [62] and Bert Scholz [63], who have written, completed and upgraded the used simulation tool at the University of Augsburg in recent years. The following two subsections are based on Refs. [64] and [65].

2.3.1 Optical modes

Figure 2.14 illustrates the different optical modes of a simplified organic light-emitting diode to which an excited molecule can dissipate its energy. Here, one can distinguish between four different channels. The first mode is the direct emission to air. The amount of power that is coupled to this channel is determined by total internal reflection at the substrate/air interface and therewith by the refractive index of the (glass) substrate and the angular dependent emission profile of the emissive molecules. Strictly speaking, the refractive index of the emissive layer can influence the outcoupling efficiency, too, particularly if a matrix material with a low refractive index can be used. However, in a typical OLED with an isotropic emitter orientation the internal light escape cone is about 30° from the surface normal and less than 20 % of the total power is radiated into this optical channel. Light that is emitted under higher angles is guided in substrate modes until it reaches the angle of total internal reflection due to the refractive index mismatch at the organic/substrate interface. For the sake of simplicity, we do not distinguish between the organic layers and the indium tin oxide (ITO) anode, that is typically used in bottom emitting OLEDs, in this discussion. However, substrate modes are easily extracted by light outcoupling structures based on ray optics, such as glass hemispheres or outcoupling foils. The residual light, that is not coupled into one of the first two optical channels is captured inside the organic layers as waveguided modes or is absorbed by the organic layers. The remaining consumed (electrical) power is dissipated (non-radiatively) into vibronic modes of the molecules and/or the molecular lattice or

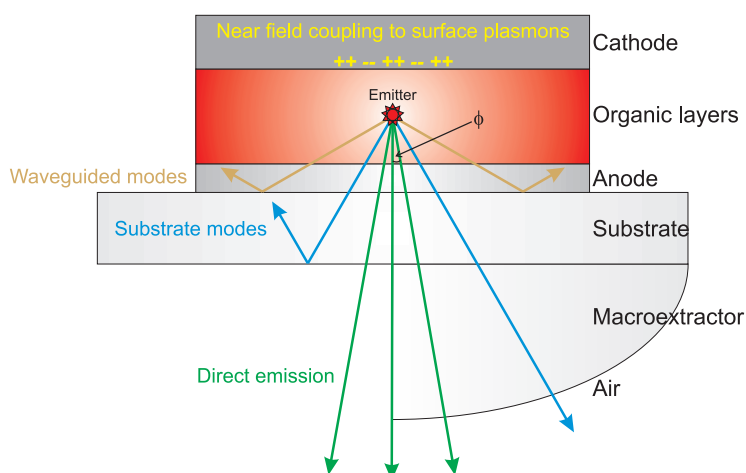


Figure 2.14: Schematic illustration of the different optical modes in a simplified OLED structure. On the right half of the OLED a macroscopic index-matched outcoupling structure is attached to extract the substrate modes of the device. With this outcoupling enhancement a huge boost in the EQE can be achieved.

is near-field coupled (radiatively) to surface plasmon polaritons at the organic/metal interface. The latter is one of the major optical loss channels in organic light-emitting diodes, especially if the emitting species is located close to metallic layers. Calculating the optical losses in a typical planar OLED stack with isotropic emitter orientation by integrating over the coupled power to waveguided modes and to SPPs results in values as high as 50 % of the radiatively generated energy of the excited molecules [42, 51, 52].

2.3.2 Optical simulation

As mentioned before, one has to distinguish between an excited molecule in an infinite bulk material and in stratified media embedded in a microcavity structure, like an OLED. In the latter case, the emission of the molecules (fluorescence and/or phosphorescence) is modified by its optical surroundings by the so-called Purcell effect, that has been originally investigated in magnetic resonance experiments [43]. Later, the importance of this effect for excited molecules near (reflecting) interfaces has been pointed out [66, 67]. The first theoretical principle of the situation of an excited molecule near a surface have been developed by Chance, Prock, and Silbey. In their approach the emitting molecules are treated as classical oscillating electrical dipoles near a dielectric interface [68, 69]. This is possible because the radiated power of a classical dipole antenna corresponds to the quantum mechanical probability of the radiative decay under light emission of an excited molecule. This theoretical model was later expanded for ensembles of molecules

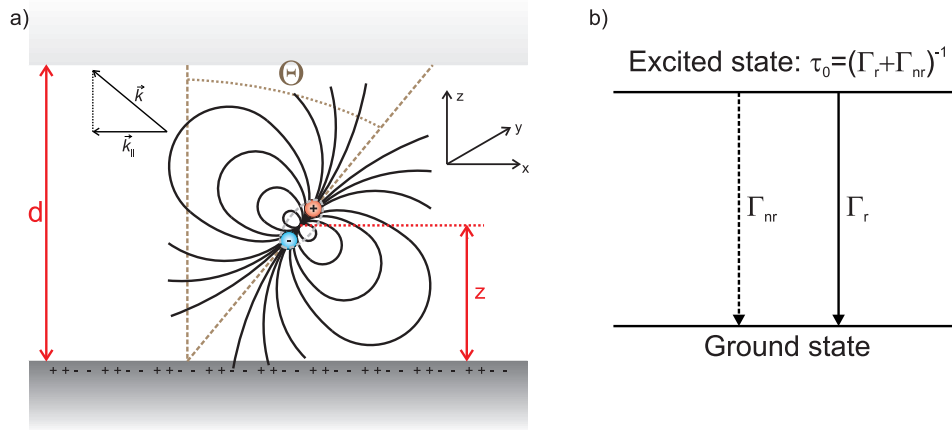


Figure 2.15: a) Sketch of an oscillating electrical dipole embedded in a (dielectric) layer, which is sandwiched between two interfaces. Near-field coupling to surface plasmons appears at the interface to the lower layer, due to its metallic character. Parameters that are influencing the emission from the radiating dipole are the cavity length d , the distance z of the dipole to the metal, the relative orientation Θ of the transition dipole moment to the surface normal, the wavevector \vec{k} of the emitted electromagnetic wave, its in-plane component $k_{||}$ and the optical constants of the surrounding media. The coordinate system used for the theoretical considerations is shown as inset. b) Quantum mechanical analogue. The two-level system consists of an excited state of the molecule and the ground state with radiative and non-radiative decay rates between them, leading to a finite lifetime of the excited state. If the dipole is embedded in a cavity, the radiative rate will be modified by the Purcell factor F : $\Gamma_r^* = F \cdot \Gamma_r$. Hence, the excited state lifetime can be described by $\tau = (\Gamma_r^* + \Gamma_{nr})^{-1}$.

embedded in multiple layer stacks with different optical constants and near metallic interfaces [22, 44, 70].

The optical simulation used in this study follows the formalism of Barnes and Wasey, which solves the 3-dimensional Maxwell equations for an excited dipole emitter ensemble surrounded by multiple thin and planar layers with respect to electromagnetic boundary conditions [24]. Physical input parameters are the layer thicknesses (d_i , where $\sum d_i$ is the cavity length of the OLED), the complex refractive indices (n_i and κ_i), the position of the excited molecule with respect to the different interfaces (especially the emitter/metal distance z), the emitter orientation Θ and the intrinsic radiative quantum efficiency (q) of the emitting (guest/host) system (see Fig. 2.15). Using a transfer-matrix-formalism and taking into account the Fresnel reflection and transmission coefficients at the involved interfaces allows to calculate the power dissipation spectrum for a given dipole ensemble.

If the emitting system is embedded in an OLED stack, the presence of a microcavity changes two important emission parameters of the ensemble of emitter molecules. First,

the radiative decay rate is changed by the Purcell factor F , resulting in an effective RQE of the emitting system as mentioned before (see Eq. 2.11). This is equivalent to a changed excited states lifetime of the molecules given by

$$\tau = \frac{1}{F \cdot \Gamma_r + \Gamma_{nr}} \equiv \Gamma^{-1} \quad (2.12)$$

as compared to $\tau_0 = (\Gamma_r + \Gamma_{nr})^{-1} \equiv \Gamma_0^{-1}$ in the absence of a cavity. Thereby, Γ represents the sum of the modified radiative decay rate $\Gamma_r^* = F \cdot \Gamma_r$ and the non-radiative decay rate Γ_{nr} of the emitting system embedded in the OLED cavity and Γ_0 stands for the sum of the intrinsic decay rates in an infinite bulk.

Second, the microcavity changes the power distribution between the different optical channels, such as direct emission and substrates modes, determining the outcoupling factor of the device η_{out} .

Following from these basic principles, the radiated power can be expressed as the relative decay rate of an isotropically oriented ensemble of non-interacting excited molecules emitting at one distinct wavelength inside a cavity (Γ) as compared to in an infinite bulk (Γ_0) [24]

$$\tilde{P} = \frac{\Gamma}{\Gamma_0} = (1 - q) + q \cdot \int_0^\infty P(k_{||}, \lambda, z) dk_{||}, \quad (2.13)$$

wherein $P(k_{||}, \lambda, z)$ is the specific power dissipation function, which depends on the component of the wavevector that is projected onto the plane of the device surface $k_{||}$, the emitted wavelength, and the emitter position in the OLED stack z (see Fig. 2.15). Due to the very small thickness of the emission layer ($\approx 10 - 20$ nm) typically used in OLEDs based on small molecules, a δ -shaped emission zone was assumed in all simulations presented in this theses. However, it is straightforward to implement spatial profiles such as Gaussian or exponential functions for the emission zone, which will be very important for (one-layered) polymeric OLEDs, just by simulating δ -shaped emission profiles at different positions (z) inside the OLED cavity and averaging these results with the pre-defined shape function [71].

Figure 2.16 shows the power dissipation spectrum of a typical red state-of-the-art OLED stack. In this simulation a δ -shaped emission zone was assumed, the RQE was set to unity and an isotropic orientation of the emissive dipole moments of the emitter was supposed. The power dissipation spectrum was first calculated for a "white" spectrum, for which the intensity at each wavelength has been set to the same value between 400 nm to 800 nm and was later on weighted with the normalized intrinsic emitter spectrum $S(\lambda)$.

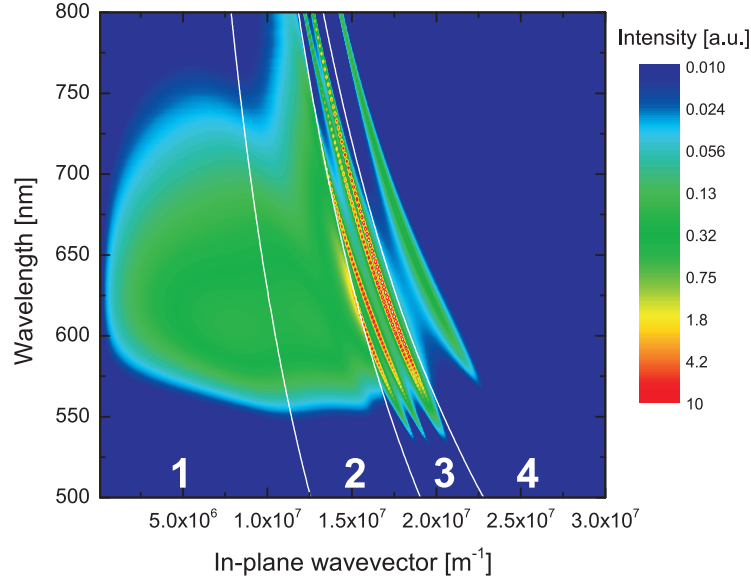


Figure 2.16: Simulated power dissipation spectra of a typical red state-of-the-art OLED stack as a function of the emitted wavelength and the in-plane wavevector. Colored areas indicate different intensities of the emission. The dashed white lines represent the different optical modes of the device; 1: direct emission to air, 2: light that is captured in the substrate, 3: waveguided modes, and 4: coupled energy to surface plasmons polaritons at the cathode/ETL interface.

In agreement with Eq. 2.13 one can now calculate the total emitted power of the emissive system by using the simulated power dissipation spectrum and integrating over all relevant wavelengths and in-plane wavevectors:

$$\tilde{P}_{\text{tot}} = (1 - q) + q \cdot \int_{\lambda_1}^{\lambda_2} S(\lambda) \int_0^\infty P(k_{||}, \lambda, z) dk_{||} d\lambda. \quad (2.14)$$

With the definitions of the intrinsic and the modified total decay rates in an infinite medium and inside a cavity, respectively, it follows that the spectrally weighted integral over the power dissipation directly yields the Purcell factor F . Thus Eq. 2.14 can be rewritten as

$$\tilde{P}_{\text{tot}} = (1 - q) + q \cdot F. \quad (2.15)$$

Therewith, the relative changes of the radiative quantum efficiency are given by:

$$\frac{q_{\text{eff}}}{q} = \frac{F \cdot (\Gamma_r + \Gamma_{\text{nr}})}{F \cdot \Gamma_r + \Gamma_{\text{nr}}} = F \cdot \frac{\Gamma_0}{\Gamma} = \frac{F}{F \cdot q + (1 - q)}. \quad (2.16)$$

Please note that in this terminology the coupling of the excited molecules to modes

of the cavity that do a priori not radiate into the far-field, such as waveguided modes or surface plasmons, are radiative processes, since they contribute to F and thus change the radiative decay rate Γ_r . Furthermore, in practice the integration over $k_{||}$ is only carried out up to a finite cutoff value, where the contribution of surface plasmons has dropped to sufficiently small values (in most cases at around $4 \cdot 10^7 \text{ m}^{-1}$).

With the simulated power dissipation spectra, it is also possible to derive the fraction of power that is dissipated to the different optical modes – to be understood in the first instance as the internal power contribution of a mode inside the cavity – as discussed at the beginning of this section:

$$\tilde{P}_{\text{mode}} = q \cdot \int_{\lambda_1}^{\lambda_2} S(\lambda) \int_{u_1}^{u_2} P(k_{||}, \lambda, z) dk_{||} d\lambda. \quad (2.17)$$

In this equation u_i denotes the limits for the in-plane wavevector between which power is coupled to the different optical channels as is already indicated by the white lines in Fig. 2.16. To arrive at the power that is actually coupled to far-field radiation in air $P_{\text{air}}^{\text{out}}$ (coresponding to region 1 in Fig. 2.16), a modified specific power dissipation function $P'(k_{||}, \lambda, z)$ has to be used, including the transmittance of radiation through the relevant interfaces and layers between the emitter position and the outside world (for details see Ref. [24]). In this case, the in-plane wavevector has to fulfill the condition $0 \leq k_{||} \leq n_{\text{air}} \cdot k_0$, with n_{air} being the refractive index of air and k_0 is the wavevector in air for a given wavelength ($k_0 = 2\pi/\lambda$). Moreover, the simulation then directly yields the outcoupling factor η_{out} for the device without light extraction modifications, if the radiative quantum efficiency of the emitting system is set to unity:

$$\eta_{\text{out}} = \frac{P_{\text{air}}^{\text{out}}}{\tilde{P}_{\text{tot}}}; \text{ if } q \equiv 1. \quad (2.18)$$

Otherwise, if $q < 1$, one has to consider the effective RQE, too, leading to the following equation:

$$q_{\text{eff}} \cdot \eta_{\text{out}} = \frac{P_{\text{air}}^{\text{out}}}{\tilde{P}_{\text{tot}}}; \text{ if } q \neq 1. \quad (2.19)$$

However, even in this case it is straightforward to obtain η_{out} by using Eq. 2.16. Furthermore, it is also possible to calculate the outcoupling efficiency of the device if macroscopic outcoupling enhancements such as index-matched glass hemispheres are used. If so, one has to change the upper limit of the integration over the in-plane wavevector

from $n_{\text{air}} \cdot k_0$ to $n_{\text{substrate}} \cdot k_0$, with $n_{\text{substrate}}$ being the refractive index of the used substrate (corresponding to regions 1 + 2 in Fig. 2.16). Please note that in case of an incoherent, i.e. optically thick, substrate the power that is outcoupled to air has to be calculated by an incoherent addition of multiple beam intensities, as outlined in Ref. [72].

Another challenge for simulation tools exists for non-isotropic emitter orientations. In this case, one has to distinguish between three different fundamental orientations of transition dipole moments inside the OLED and perform the simulation for each of these three dipoles. The differently oriented dipoles are denoted with respect to the y - z -plane for the coordinate system shown in Fig 2.15, as

- $P_{\perp, \text{TM}}$: dipoles oriented perpendicular to the substrate plane (vertical; z -direction), which emit p-polarized (transverse magnetic (TM)) light,
- $P_{\parallel, \text{TM}}$: dipoles oriented parallel to the substrate plane (horizontal; x - y plane), which emit p-polarized (TM) light,
- $P_{\parallel, \text{TE}}$: dipoles oriented parallel to the substrate plane (horizontal; x - y plane), which emit s-polarized (transverse electric (TE)) light.

Due to symmetry aspects the two horizontally oriented dipole orientations are equivalent, because the plane of observation is chosen arbitrarily. Therefore, in the case of isotropic emitter orientation the total emitted power by an ensemble of excited molecules inside the OLED cavity can be written as:

$$P_{\text{iso}} = \frac{2}{3}P_{\parallel} + \frac{1}{3}P_{\perp}. \quad (2.20)$$

To account for orientation effects, it is helpful to introduce an anisotropy factor θ that is defined as the ratio between the amount of vertical dipoles and the total number of dipoles [59]. According to this definition, $\theta = \frac{N_z}{N_x + N_y + N_z}$ becomes 1/3 for isotropic emitter orientation, 1 for only vertical dipoles (dipoles in z -direction) and 0 for totally horizontal emitter orientation (all dipoles are lying in the x - y -plane). With this information the weighted Purcell factor can be calculated as

$$F(\theta) = \frac{1 - \theta}{2} (F_x + F_y) + \theta \cdot F_z. \quad (2.21)$$

By this means separate Purcell factors F_i are introduced for each of the three orthogonal dipole orientations (x , y , and z)

$$F_i = \int_{\lambda_1}^{\lambda_2} S(\lambda) \int_0^\infty P_i(k_{||}, \lambda, z) dk_{||} d\lambda. \quad (2.22)$$

Finally, the relative change of the excited states lifetime with respect to the value τ_0 , measured in the absence of the cavity ($F_i \equiv 1$), is obtained by taking into account the radiative quantum efficiency of the emitter material q from Eq. 2.10

$$\frac{\tau(\theta)}{\tau_0} = \frac{\Gamma_0}{\Gamma(\theta)} = \frac{1}{F(\theta) \cdot q + (1 - q)}. \quad (2.23)$$

CHAPTER 3

DEVICE PREPARATION, MATERIALS AND STACK DESIGN

The previous section has illustrated the basic principles of device performance of organic light-emitting diodes. This chapter will describe the device preparation, the used materials and the stack design of two different types of devices, that are either fabricated at the University of Augsburg (UNA) or are provided by the concern OSRAM Opto Semiconductors (OOS), Regensburg, within a framework of a cooperation.

3.1 Devices fabricated at University of Augsburg

Figure 3.1 demonstrates a typical multilayered OLED stack layout comprising different organic layers to achieve improved device performance compared to one-layered OLEDs. Four different organic layers are subsequently evaporated on an indium tin oxide (ITO; 140 nm thickness) covered glass substrate, that was pre-cleaned by several solvents (acetone, isopropanol) in ultrasonic baths and by an UV-ozone treatment under cleanroom conditions. The UV-ozone treatment is not only a cleaning process but is also activating the surface of the ITO resulting in an increase of its workfunction what is advantageous for hole injection into the organic layers [73, 78]. After the cleaning steps the samples are transferred to a nitrogen glovebox protecting the organic materials and the later fabricated OLEDs from moisture and air. An ultra-high vacuum (UHV) evaporating chamber is directly connected to the glovebox to prevent a contamination of the pre-cleaned samples and the OLEDs after the fabrication process. This evaporation chamber

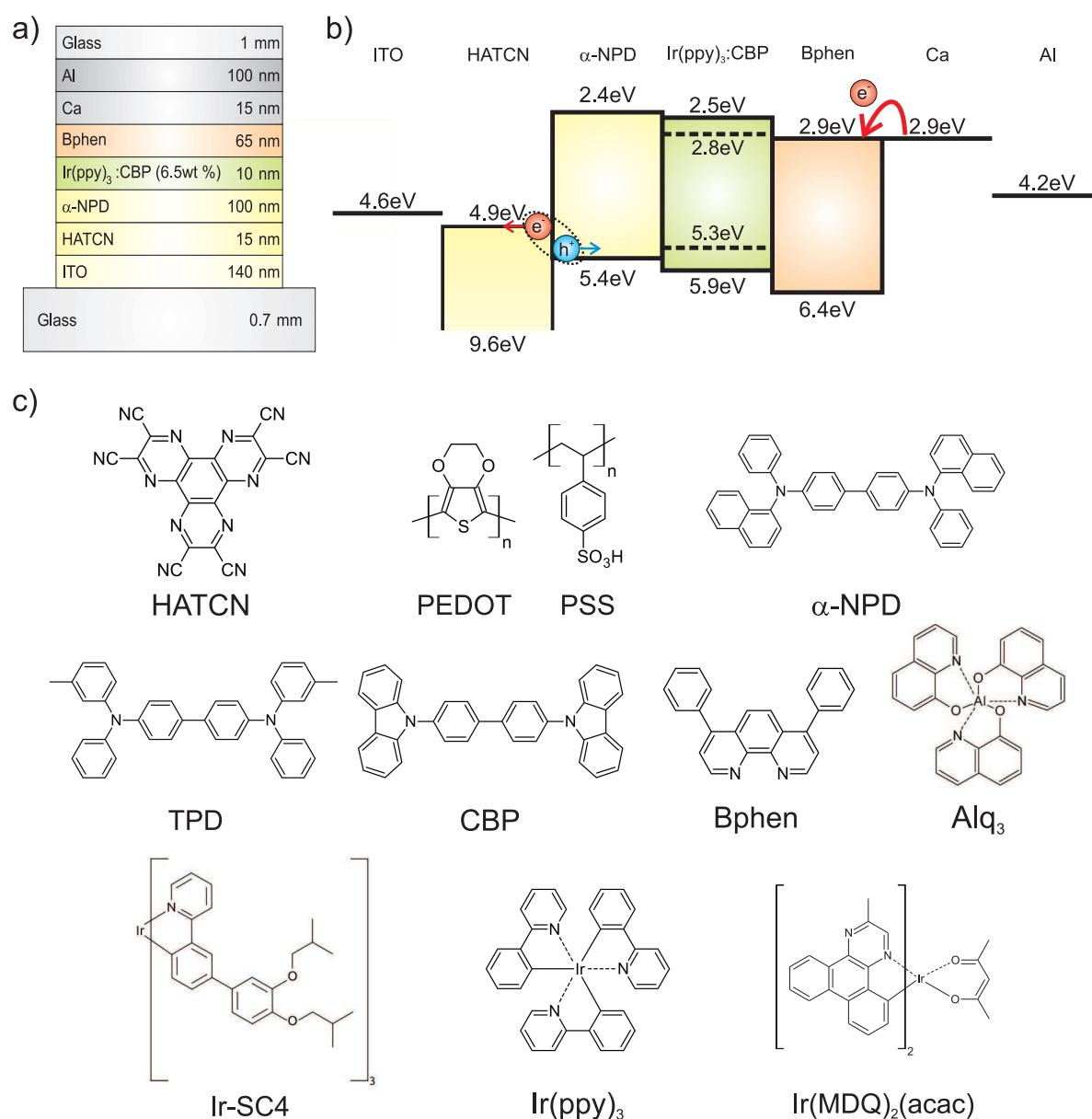


Figure 3.1: a) Stack design of a modern OLED. Strictly speaking, the encapsulation glass at the top of the device is not directly lying on the cathode of the OLED and therewith a little amount of the inert gas atmosphere of a glovebox is captured between the cathode and the glass lid. b) Schematic energy diagram of the HOMO and LUMO levels of the used organic molecules. (Values are taken from Refs. [73–77].) c) Molecular structure of the used organic materials.

allows to prepare devices with six different organic materials and three different metals without breaking the vacuum (base pressure is about $2 \cdot 10^{-7}$ mbar). The deposition rates (typical in the range of 1 Å/s) and layer thicknesses of all materials are detected by

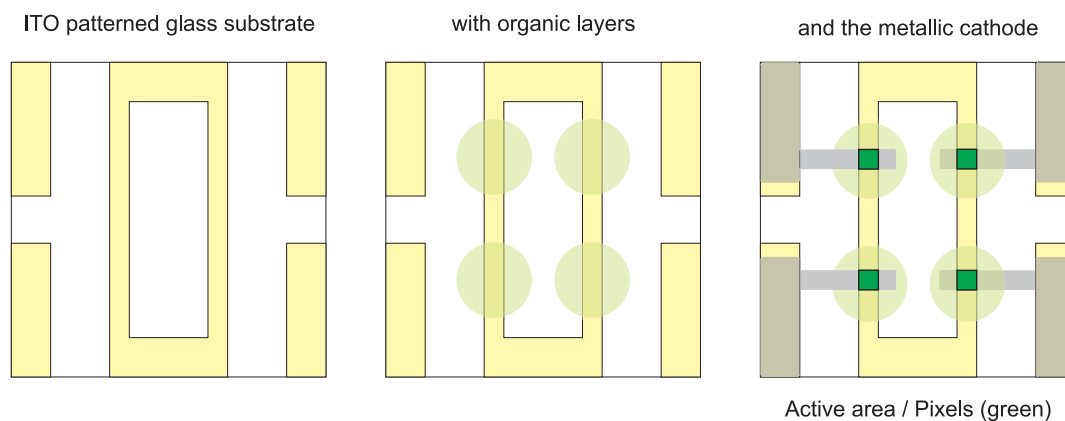


Figure 3.2: Macroscopic device structure of samples fabricated at UNA. Colored areas represent the different materials. Yellow: ITO; greenish cycles: organic layers; gray: metallic cathode; green squares: active pixel. Fabrication steps are shown from left to right.

quartz-microbalances. The macroscopic structure of the OLEDs is given by the layout of both electrodes and by shadow-masks used during the evaporation of the organic materials. The OLED layout of samples fabricated at UNA is shown as a sketch in Fig. 3.2 resulting in four equal pixels with an active area of 1 mm^2 each on one common substrate.

However, for the device under investigation shown in Fig. 3.1, first 15 nm of hexazatriphenylene-hexanitrile (HATCN) as a hole generation layer, followed by 100 nm of N,N'-bis(1-naphthyl)-N,N'-diphenyl-1,1'-biphenyl-4,4'-diamine (α -NPD) acting as hole transport layer (HTL) are evaporated on the ITO covered glass substrate. The next layer is a compound of two different organic molecules and forms the thin emission layer (EML) of the device, with 4,4'-bis(N-carbazolyl)-1,1'-biphenyl (CBP) acting as matrix doped with 6.5 wt% of the green phosphorescent emitter fac-tris(2-phenylpyridine)iridium ($\text{Ir}(\text{ppy})_3$). The EML is subsequently followed by a 65 nm thick electron transport layer (ETL) consisting of the organic molecule 4,7-diphenyl-1,10-phenanthroline (Bphen). Finally, a 15 nm thick calcium cathode was deposited, protected by a thick aluminum layer. In order to protect the organic layers and the cathode from moisture and ambient air, the whole device was encapsulated in a nitrogen glovebox by a second glass substrate connected with the bottom substrate by an epoxy adhesive.

The schematic energy diagram of HOMO and LUMO levels of the different organic layers, shown in Fig. 3.1 (values are taken from Refs. [73–77]), clearly illustrates the specific functions of the organic layers. Due to the nearly fixed work functions of the usable electrodes, one has to choose the organic layers with respect to these energy values properly. Hence, HATCN was chosen as hole generation layer. This molecule

exhibits a very large energy gap of 4.7 eV , prohibiting the absorption of light that is generated in the emission layer of the device. Moreover, HATCN shows a very high electron affinity due to its deep lying LUMO energy level. Thus, electrons can easily travel from the HOMO of the adjacent hole transporting material into the LUMO of the HATCN, creating holes in the α -NPD layer. The electrons in the LUMO of the HATCN are then traveling (due to the applied electric field) to the ITO anode and are extracted there. The holes in the HOMO of the HTL are traveling to the opposite side and are later injected into the emission layer. On the other side, electrons are injected from the cathode directly into the LUMO of the electron transporting layer due to appropriate energy level alignment at the interface between calcium and Bphen, and can travel towards the emission layer easily. The emission layer of this device consists of two simultaneously evaporated materials. CPB should act as transport layer, while Ir(ppy)_3 is the emitting species. Therefore, it is very important that HOMO and LUMO energy levels of the emitter are lying inside the energy gap of the matrix, as can clearly be seen from Fig. 3.1. Hence, the emitter is acting as trap for both charge carrier species that are injected from the HTL and the ETL and a good population of excitons on the emitting molecules will follow. However, if excitons are created on the matrix, energy transfer processes as depicted in section 2.1.1 will occur due to energy minimization. In the device shown in Fig. 3.1 the HTL and the ETL are additionally acting as electron and hole blocking layers, respectively. This effect is accomplished due to the high energy barriers between the LUMO of the HTL and of the EML resulting in blocking of electrons at this interface and in the same manner for the HOMO energy levels of the ETL and the EML achieving a blocking of holes. The implementation of blocking layers into an OLED device is an important step to achieve high external quantum efficiencies as the charge carriers are confined in the EML and thus, are not lost for recombination to excitons and radiation of light. This crucial point will be discussed in detail in the following section. However, the device shown in Fig. 3.1 is not a state-of-the-art OLED as the energy alignment of the different organic layers is not ideal and the transport layers are not modified in terms of conductivity doping, but represents a typical OLED in the scope of the possibilities of fabrication at the University of Augsburg.

3.2 Devices provided by OSRAM Opto Semiconductors

In the scope of a research project in collaboration with OSRAM Opto Semiconductors, Regensburg, investigations on both, monochromatic and white OLEDs provided by OOS have been performed. The stack design of three different types of monochromatic OLEDs and a white hybrid system using phosphorescent red and green emitters while the blue emitter is a fluorescent one is shown in Fig. 3.3. The white OLED stacks under investigation are similar to the monochromatic ones but consist of one emission unit with a red, green and blue (RGB) emitting system stacked on top of each other. A rough discussion of white OLEDs will be given later in this thesis.

The principle stack design of the three different monochromatic devices shown in Fig. 3.3 is rather similar. They only differ in their layer thicknesses and emitting systems. The 100 nm thick ITO anode is subsequently covered by a hole transport layer, an electron blocking layer (EBL), the emitting system consisting of a matrix doped by some weight-percent with a phosphorescent (green and red) or a fluorescent (blue) dye, a hole blocking layer (HBL) and an electron transport layer and is finally followed by a thick silver (Ag) cathode. Both transport layers are modified in terms of conductivity doping (for more information see also Ref. [79, 80]). Hence, the layer thickness of these layers has no influence on the electrical performance of the devices and can be chosen arbitrarily. Therefore, an appropriate variation of the ETL thickness for all three devices was performed to investigate the influence of the cavity length of the OLED on the efficiency and the excited states lifetime, as will be discussed in detail in the following chapters of this thesis.

The fabrication process of these OLEDs is similar to the one used at UNA. For more information about the fabrication process it should be referred to Ref. [26]. All layer thicknesses have been checked by comparison of measured data with optical simulations [26]. All OLEDs from OOS in this thesis possess an identical macroscopic structure with sixteen pixels on each sample. The active area of one pixel was either 1 mm² or 4 mm². However, if it is not explicitly mentioned in the text, pixels with a size of 4 mm² have been used for all performed experiments in this thesis.

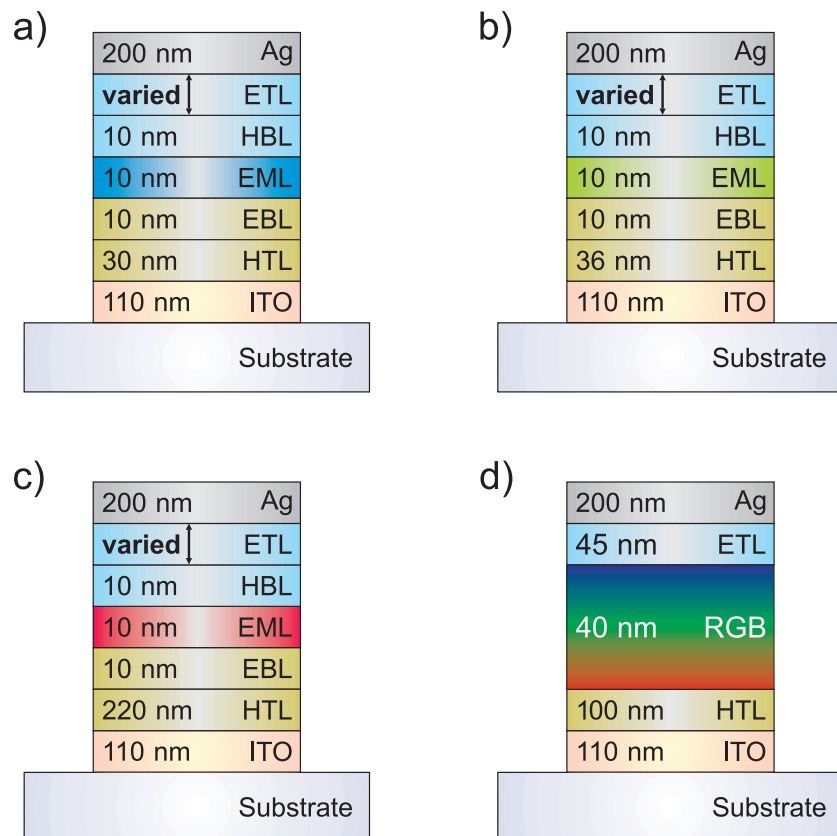


Figure 3.3: different OLEDs under investigation provided by OSRAM OS. a) Blue, b) green and c) red emitting devices. d) White emitting device using one red-green-blue (RGB) hybrid (red and green phosphorescent, blue fluorescent) unit as EML.

CHAPTER 4

EXPERIMENTAL TECHNIQUES

This chapter describes the most important experimental techniques used for the characterization of OLEDs and organic materials in this thesis.

4.1 Current-voltage-luminance characteristics

The current-voltage-luminance (IVL) characteristic is a simple but powerful tool for OLED characterization. Therefore, a voltage is applied to the device and both the current through the diode and the luminous intensity is detected simultaneously. The measurement is performed by a dual source meter (Keithley 2612) controlled via a LabView computer program. This allows for measuring the current through and the luminous output from the device stepwise by applying a voltage to the OLED, which is fixed in a measuring box. The luminance is converted to an electrical signal detected by the source meter by a Si-photodiode (Hamamatsu S2281) combined with a photometric filter (Gigahertz Optik PD-93VL) positioned directly above the device in the cover plate of the measuring box. Figure 4.1 shows representative IVL characteristics of a red phosphorescent OLED provided by OOS and of a green phosphorescent OLED fabricated at UNA (see Fig. 3.3 c) and 3.1 a) for device structure, respectively). Both samples show a typical diode behavior. This type of graphics normally shows the applied voltage on a linear scale, while the current density is plotted logarithmically. The detected luminance can be displayed in both types. Please note, that in Fig 4.1 b) the forward and the reverse direction sweep of the measurement are shown at once, whereas Fig 4.1 a) illustrates only the forward direction from -1.5 .. 4.7 V. It can clearly be seen, that

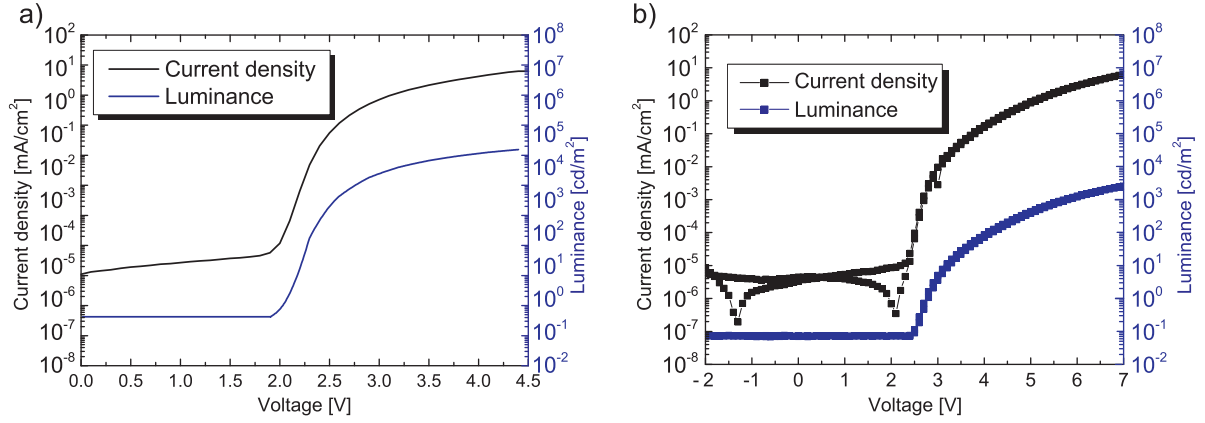


Figure 4.1: Typical IVL characteristics of a) a red OLED provided by OOS and b) a green OLED fabricated at UNA.

the performance of the OLED provided from OOS is considerably better than that of UNA (faster increase of the current density and higher luminance). However, the basic behavior is very similar and both the current density rises significantly and the light output starts for both OLEDs at about 2.5 V. At this voltage charge carrier injection from both electrodes appears and therewith accompanying radiative recombination in the emission layer.

Furthermore, the photodiode can be replaced by a collimator lens connected via fiber optics to a spectrometer (Sphere Optics SMS–500) in order to detect the emission spectrum of the sample e.g. for different current densities.

Additionally, this setup is appropriate to perform degradation protocols in terms of electrical stressing. Thereby, a constant current flow is applied to the device under investigation and simultaneously the required voltage and the actually emitted luminance can be detected during the whole aging time. The underlying photo-physical degradation processes will be analyzed for different OLEDs later in this thesis.

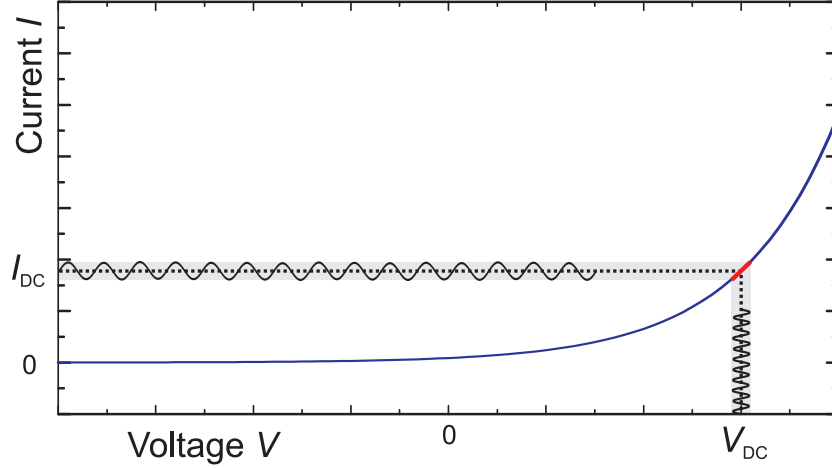


Figure 4.2: Schematic sketch of an impedance spectroscopy measurement of an ideal diode.

4.2 Impedance spectroscopy

A further electrical characterization method used in this thesis is impedance spectroscopy (IS). Therefore, a small alternating voltage (V_{AC}) with a variable frequency (f) is superposed to a constant bias voltage (V_{DC}) which defines the working point of the measurement as can be seen in Fig. 4.2. Hence the applied voltage in an IS experiment can be written as

$$\hat{V}(t) = V_{DC} + \hat{V}_{AC}(t) = V_{DC} + V_{AC} \cdot \exp(i2\pi f \cdot t), \quad (4.1)$$

leading to a constant current through the device overlain by a small alternating current with a phase shift ϕ to the applied voltage:

$$\hat{I}(t) = I_{DC} + \hat{I}_{AC}(t) = I_{DC} + I_{AC} \cdot \exp(i2\pi f \cdot t + i\phi). \quad (4.2)$$

It should be noted that the applied voltage in the measurement is not a complex quantity and the alternating voltage can be described by trigonometric functions such as sine or cosine waves, but it is more practicable to explain the theoretical behavior with a complex exponential function (e.g. Eq. 4.1).

If the alternating voltage is chosen small enough, the current response in this region is almost linear. This allows for a differential analysis of the signal which is mandatory for investigation of e.g. the capacitance of the device.

The impedance ($\hat{Z}(f)$) is a complex quantity and can be written as the ratio of voltage and current:

$$\hat{Z}(f) = \frac{\hat{V}}{\hat{I}} = \frac{V_{AC}}{I_{AC}} \cdot \exp(i\phi) = \text{Re}(\hat{Z}) + i \cdot \text{Im}(\hat{Z}). \quad (4.3)$$

Therewith, it is possible to define the capacitance of a device as follows:

$$C(f) = \frac{1}{2\pi f} \cdot \frac{-\text{Im}(\hat{Z})}{\text{Re}^2(\hat{Z}) + \text{Im}^2(\hat{Z})}. \quad (4.4)$$

There exist several different measurement approaches for IS. However, only two different procedures, the C-V and the C-f sweeps have been used in this thesis. Thereby, the capacitance of the device is measured while the frequency of the alternating voltage is fixed during a voltage sweep, or the voltage is fixed during a frequency sweep for the C-V and the C-f mode, respectively. This subsection is based on the principles presented in Ref. [61].

Impedance spectroscopy measurements have been performed with an impedance analyzer (Solatron Impedance/Gain-Phase Analyzer SI 1260) combined with a dielectric interface (Solatron 1296). The range of available frequencies and applicable voltages is between 10^{-2} to 10^7 Hz and -7 to 7 V for this setup, respectively, and the amplitude of the alternating voltage was set to 0.1 V for all measurements presented in this thesis. Figure 4.3 illustrates a typical IS measurement performed for a simplified OLED stack consisting of three organic layers. The ITO anode is covered with 50 nm of HIL1.3 (commercial available by HC Starck Clevios, chemical formula and/or structure unknown), followed by 50 nm α -NPD acting as HTL. Subsequently, a 60 nm thick tris-(8-hydroxyquinoline) (Alq_3 , chemical structure shown in Fig. 3.1) layer as ETL and EML and a LiF/Al cathode are evaporated. Finally the OLED was encapsulated with a glass lid. Due to its high conductivity, the HIL layer cannot be detected in the impedance measurements. The geometrical capacitance (C_{geo}) of the device can be determined for voltages below -1.5 V in the CV plot. This capacitance represents the total thickness of all insulating layers for reverse bias conditions:

$$C_{\text{geo}} = \frac{\epsilon_0 \epsilon_r A}{d}. \quad (4.5)$$

Therein ϵ_0 and ϵ_r represents the permittivity of free space and the relative permittivity of the organic layers, respectively, A stands for the area of the active pixel and d is the total thickness of the insulating layers, here $d = d_{\text{HTL}} + d_{\text{ETL}}$. This equation is true, because all organic layers have comparable relative permittivities of about $\epsilon_r \approx 3$ [61, 81].

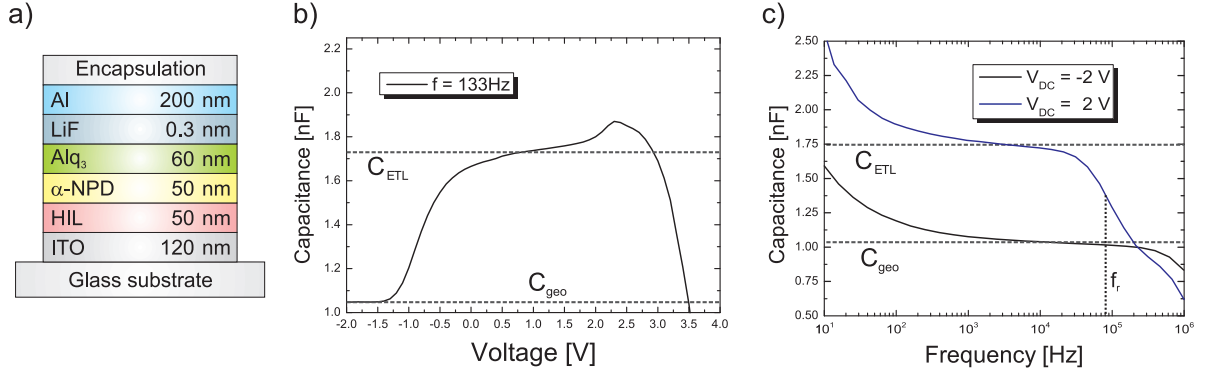


Figure 4.3: a) Stack layout of a three layered OLED. b) C-V-measurement of the device under investigation with a constant alternating frequency of 133 Hz. Holes are injected into the α -NPD layer for voltages higher than -1.3 V and accumulate at the α -NPD/Alq₃ interface until electrons are injected, too, for voltages higher than 2.5 V. c) C-f-measurement for constant DC-voltages of -2 V (black line) and 2 V (blue line). The relaxation frequency is in the range of 10^5 Hz.

Previous investigations of our group have shown that there exists an interface charge between the α -NPD and the Alq₃ layer, resulting in hole injection even for negative voltages [82, 83], as can be seen in Fig. 4.3 b) from the increase of the capacitance at about -1.3 V. This effect was demonstrated for other material systems, too [84]. The capacitance decreases rapidly for voltages higher than 2.5 V due to electron injection from the cathode and subsequent charge carrier recombination. Figure. 4.3 c) shows the frequency sweep of the same sample for fixed voltages of ± 2 V. At -2 V, in accordance to the CV-measurement, no charge carriers are injected into the device and one is measuring the geometrical capacitance. However, for an applied voltage of 2 V, holes are already injected into the HTL, but no electron injection from the cathode into the ETL is detectable. Therefore, the middle of the transition from C_{geo} to C_{ETL} , according to eq. 4.5 with $d = d_{\text{ETL}}$, represents the relaxation frequency for the holes in the HTL and is proportional to their conductivity [61].

Thus, impedance spectroscopy measurements can detect charge carrier injection, charge accumulation processes, and charge carrier conductivities. Moreover, it depicts a simple tool for layer thickness determination after the fabrication process of multi-layered OLED structures.

4.3 Time-resolved luminescence spectroscopy

The main focus of the experimental techniques used in this thesis is placed on time-resolved luminescence spectroscopy. This is a powerful tool to analyze excitonic processes in organic materials and light-emitting diodes, since several effects, depicted in the former chapters, such as the Purcell effect or TPQ, can influence the excited states lifetime of the emitting molecules. Furthermore, it is possible to analyze degradation induced changes of the transition rates in complex OLED structures as will be discussed in detail later.

4.3.1 Basic principles

The centerpiece of the time-resolved measurement setup is represented by a streak camera system (Hamamatsu C5680) as depicted schematically in Fig. 4.4, which allows to detect the time-dependent decay of the excited state population in an organic solid and the energy distribution of the emitted photons simultaneously. Therefore, it is essential to excite the molecules under investigation with a short pulse. If the excitation is accomplished with a laser-pulse one can detect the photoluminescence lifetime of the excited states, while one calls this phenomena electroluminescence if the excitation is induced by an electrical pulse. However, if laser excitation is used, it is mandatory that the pulse duration is significantly shorter than the excited states lifetime of the emitting molecules. Otherwise the analysis of the measured data will be very difficult to interpret or even erroneous. Whereas for the electrical excitation a crucial point represents the edge steepness of the square wave voltage pulse and the RC time of the sample as limiting factor for consistent excited states lifetime determination by means of analysis of the electroluminescence decay after the pulse.

To allow for an optimal photoluminescence excitation process for a huge variation of materials and OLEDs, several laser systems are available at the University of Augsburg, that differ in pulse energy output (E_p), repetition frequency (f_{rep}), pulse duration (t_p) and excitation wavelength (λ) as can be seen in detail in the following enumeration:

- Hamamatsu Picosecond Light Pulser PLP10-038: $E_p \approx 1 \text{ nJ}$, $f_{\text{rep}} = 2 \text{ Hz} - 100 \text{ MHz}$, $t_p = 80 \text{ ps}$, $\lambda = 375 \text{ nm}$
- Laser Technik Berlin MNL 200 Nitrogen Laser: $E_p \approx 10 - 100 \text{ }\mu\text{J}$, $f_{\text{rep}} = 20 \text{ Hz}$, $t_p = 700 \text{ ps}$, $\lambda = 337.1 \text{ nm}$; changeable with dye laser automatic tuning module (LTB ATM200/UV1) between 375 and 950 nm.

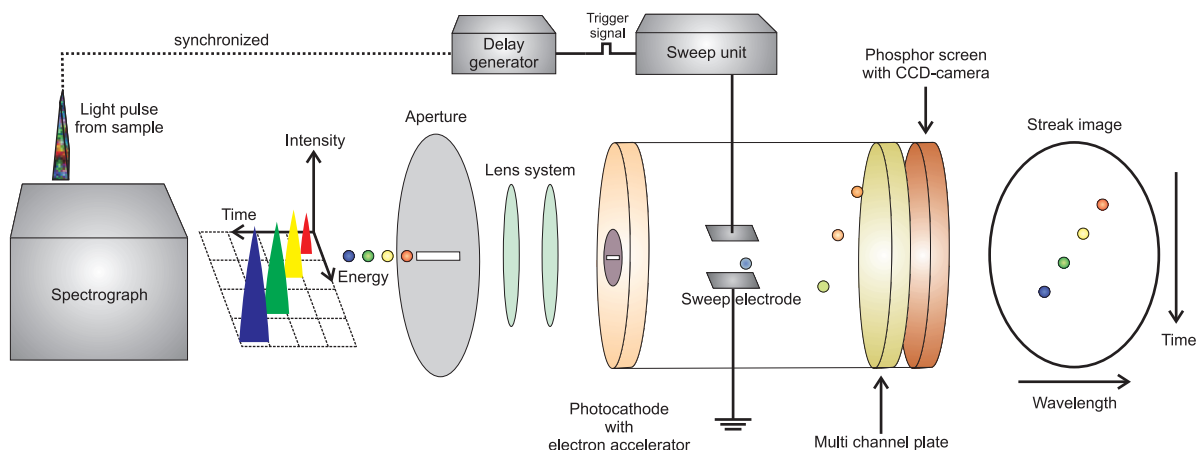


Figure 4.4: Schematic sketch of the operating mode of a streak camera system.

The pulsed electrical excitation of OLED structures was performed by an arbitrary waveform generator (Tabor Electronics WW2571A) with repetition frequencies between 10 Hz and 1 Hz with pulse durations of some microseconds depending on the duty cycle that can be varied in the range of 0.1 % to 100 %. The maximum pulse height for square waves constitutes up to 16 Vpp and the rise/fall time is below 4 ns from a constant offset voltage to 10 Vpp and 5 ns from 10 Vpp to 16 Vpp. This allows for an electrically pumped excited states lifetime analysis for almost all phosphorescent organic emitting systems, if the OLED structure is optimized in terms of its RC-time as will be discussed later in detail.

In all cases, the excitation signal was synchronized with the streak camera system by a multichannel delay generator (Stanford Research Systems DG535).

Figure 4.4 shows the working principle of the used streak camera system as a sketch which will be explained in detail in the following. After a short excitation pulse, the exponential decay of the emitted light from the sample under investigation is collected with fiber optics and collimator lenses and is afterwards coupled to a grating spectrograph (Princeton Instruments Acton SpectraPro 2300i). Thus, the light that is emitted from the sample, is separated in the horizontal direction due to different interference conditions for different wavelengths inside the spectrograph. Thereby, photons with different energies leave the spectrograph at different horizontal positions and hence it is possible to determine the time-dependence independently from the energy distribution of the emission spectrum. Accordingly, the photons are passing an aperture and are focused by a lens system on a photocathode, which converts the photons to electrons by the so-called photoeffect. The electrons are subsequently accelerated by an electric field

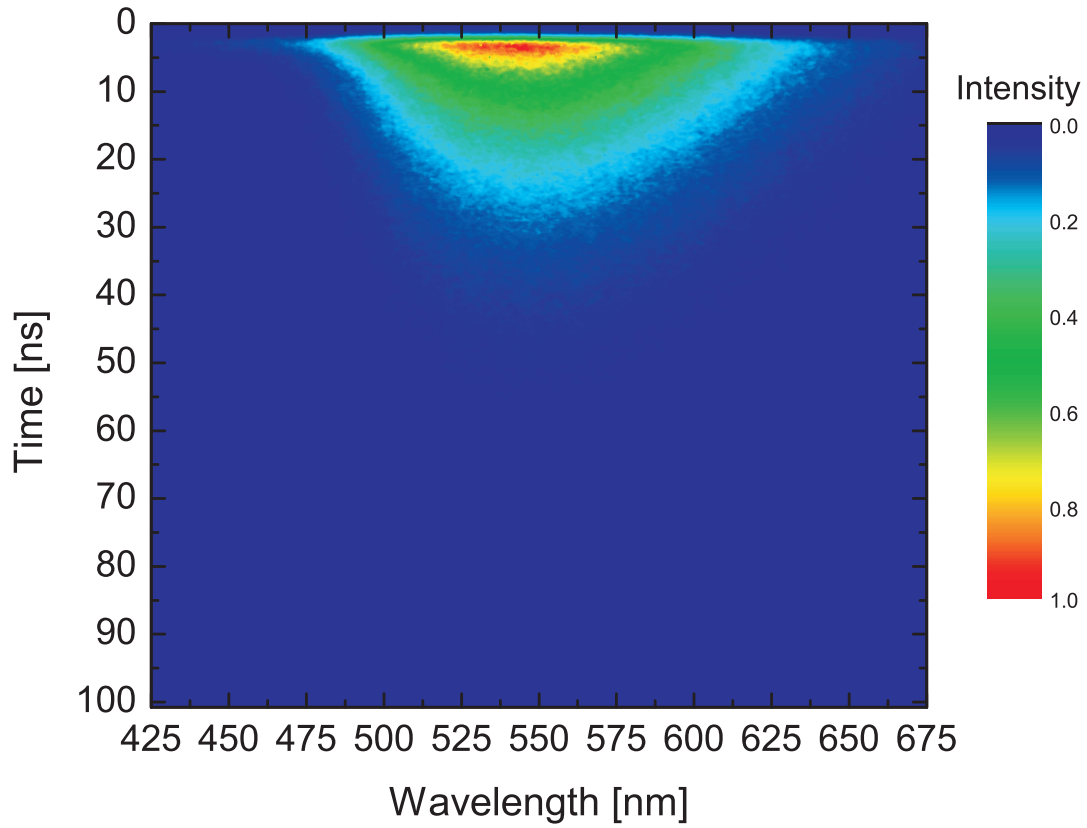


Figure 4.5: Exemplarily streak camera image of a 10 nm thick Alq_3 film on a glass substrate. The excitation was performed by a short laser pulse with a wavelength of 337.1 nm.

of several thousand Volts to minimize velocity differences due to the variable kinetic energy of electrons, with different wavelength after extraction from the cathode by the photoeffect. Thereafter, the electrons are traveling through a vertical capacitor in which the electrical field is swept within a certain time leading to a temporal resolution of the primary optical signal from the sample. Afterwards, the distracted electrons traverse a micro-channel plate where they are getting multiplied in order to amplify the signal. Finally, the electrons are hitting a phosphor screen and are reconverted to photons again. The image on this screen is determined by the wavelength and the time at which the photons have been emitted by the organic emitting system. The phosphor screen is recorded with a CCD camera system converting the optical signal in an electrical one that can be analyzed by a special computer program.

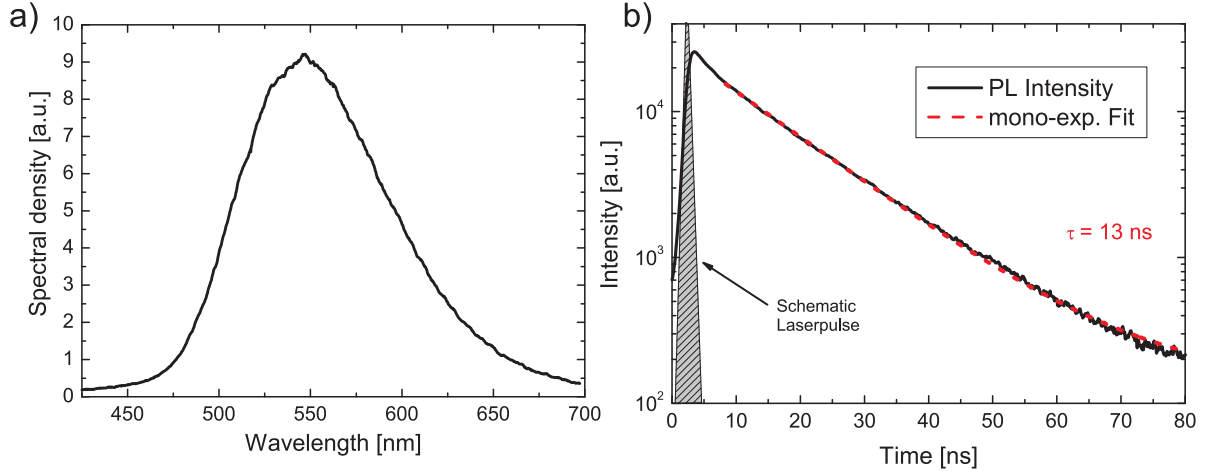


Figure 4.6: Interpretation of the measured data depicted in Fig. 4.4. a) Integrating over the time results in the emission spectrum of the Alq₃ sample. b) Integrating over all wavelengths leads to the time-dependent intensity behavior, that can be fitted by a mono-exponential decay yielding an excited states lifetime of 13 ns. The gray area drafts the position of laser excitation that is not detected with the streak camera system..

Figure 4.5 shows a typical result of a streak camera photoluminescence measurement of a 10 nm thick film of the organic molecule Alq₃ on a glass substrate excited with a nitrogen laser pulse. The analysis of this image is shown in Fig. 4.6. The emission peak wavelength is about 545 nm and the excited states lifetime can be determined by integrating the spectrum over the time and fitting this result with a mono-exponential decay to 13 ns. The fitting function can be written as

$$I(t) = I_0 \cdot \exp(-t/\tau_0) + C, \quad (4.6)$$

wherein $I(t)$ represents the time-dependent intensity of the signal, I_0 stands for the initial value of the intensity and τ_0 is the excited states lifetime of the emitting system under investigation. The constant C describes the offset of the detected signal caused by background noise.

Furthermore, it is possible to integrate only over certain parts of the streak camera image. This allows for a separation of e.g. two signals from different emitters excited at the same time and therewith simplifies the analysis of emission signals of complex OLED structures.

4.3.2 Examples of time-resolved measurement concepts

In order to emphasize the possibilities of the introduced time-resolved measurement setup, two exemplarily experiments without the demand of completeness will be presented in the following.

Energy transfer via near-field coupling

The first result is part of a more comprehensive experiment, which was performed in cooperation with Jörg Frischeisen, that investigates the energy transfer from one organic material to another via near-field coupling to surface plasmon polaritons (SPPs) [85]. SPPs are electron density waves at the interface between a metal and an insulator inside the conductor [86–88]. The electrical field of a surface plasmon polariton has its maximum at the interface and the evanescent field is decreasing exponentially in both directions into the metal and the dielectric. Thereby, the reduction of the field intensity is much stronger in the metal compared to the insulator [62]. If the excited emitting molecules of an organic compound are close to a metallic layer, the electrical field of the oscillating dipole and the evanescent field of the SPP can significantly overlap. Hence, a direct energy transfer from the excited electronic state of the molecule to an SPP via near-field coupling can follow. However, the other way round is possible, too, and thus the excited SPPs can transfer their energy back to molecules next to the metal/organic interface [22]. This type of experiment was first proposed by Andrew and Barnes [89]. With this approach it is possible to recycle part of the lost energy that is captured in SPPs in organic light-emitting diodes resulting in an efficiency enhancement.

In order to verify this concept, three different samples shown in Fig. 4.7 have been fabricated. The basic stack design of all samples consists of a 67 nm thick silver layer sandwiched between two poly(methyl methacrylate) (PMMA; Sigma-Aldrich, Mw = 996.000) layers, each with a thickness of 90 nm, on a glass substrate. The two PMMA layers are acting as host materials for two different molecular dyes, Alq₃ and Lumogen Red (LR; commercially available from BASF). Subsequently, for the first sample (A), the PMMA layer between the silver layer and the glass substrate was doped with 10 wt% Alq₃, while the PMMA capping layer was undoped. For the second sample (B), the PMMA capping layer was doped with 2 wt% LR and the other PMMA layer remained undoped. Finally, a third sample (C), a combination of the first two samples, for which both PMMA layers are separately doped with the mentioned organic dyes, was fabricated to analyze the energy transfer mechanism via near-field coupling by SPPs. Thus, due to

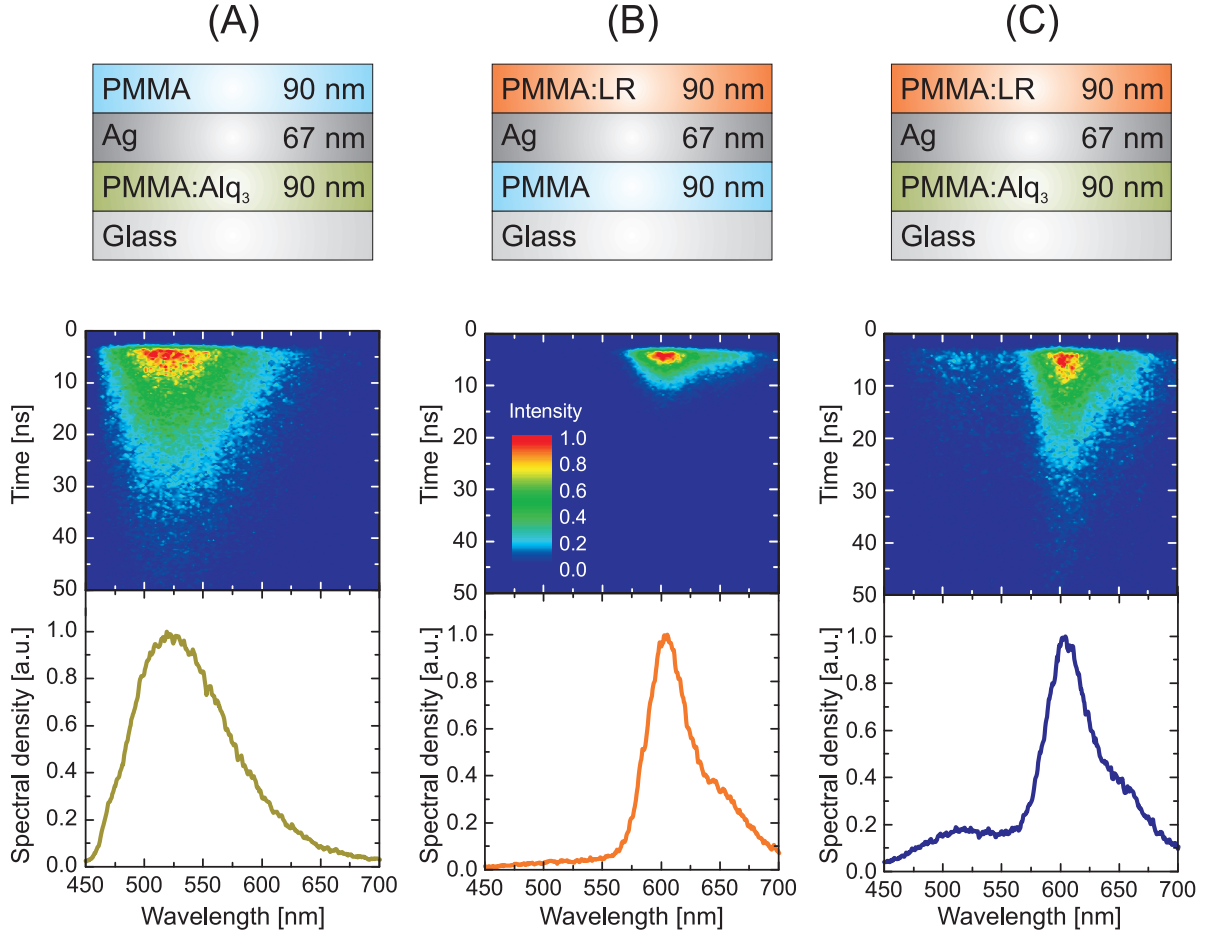


Figure 4.7: Energy transfer via near-field coupling by surface plasmon polaritons. The upper row shows the three different samples consisting of a 67 nm thick silver layer sandwiched between two PMMA layers. The stacks have been fabricated on a glass substrate. For the stack in (A) one PMMA layer is doped with Alq₃ molecules while in (B) one PMMA layer is doped with LR. The second PMMA layer is not doped for (A) and (B). The sample in (C) contains two doped PMMA layers, one with Alq₃ molecules and one with LR, acting as energy donor and acceptor, respectively. The middle row shows streak camera images of the photoluminescent decay of the excited states for the three different samples under investigation. The lower row represents the measured spectral density of the photoluminescence integrated over the whole time-resolution of the streak camera image. Sample C exhibits simultaneous emission from both organic dyes. Graphics taken from Ref. [62].

the overlap of the emission spectra of Alq₃ with the absorption spectra of LR doped into the PMMA matrix, the green emitting Alq₃ dye can act as an energy donor for the red emitting LR molecules on the other side of the silver mirror [85]. For more information about sample preparation it should be referred to Ref. [62].

However, the verification of the functionality of this approach was first required by measuring the photoluminescence emission spectra of the presented three samples under continuous wave (cw) laser excitation at a wavelength of 375 nm under an incident angle of 45° from the glass substrate side. The results of these measurements give a hint, that the demonstration of the energy transfer from Alq₃ to LR via near-field coupling by the SPPs in the metallic layer was successful [85] and no or only marginal direct energy transfer via a Förster mechanism [90] (please also see sec. 2.2.1) is present. Unfortunately, a clear evidence for the near-field coupling process via SPPs is still missing. Hence, time-resolved photoluminescence spectroscopy was performed for the three different samples. To ensure the comparability to the former measurements the samples have been excited by a nitrogen laser coupled with an automatic tuning module equipped with a proper laser dye resulting in an excitation wavelength of 375 nm and a pulse length of 1.2 ns. The samples have been transferred to a vacuum cryostat to minimize degradation processes during the measurement. Fig. 4.7 demonstrates the results of the time-dependent decay of the emission spectra for the different emitting dye molecules. The middle row of Fig. 4.7 shows the streak camera images of samples A, B and C, which are normalized to the highest intensity of each detected emission, respectively. It can clearly be seen from the images of sample A and B, that the excited states lifetimes of Alq₃ (sample A) and LR (sample B) differ strongly. Moreover, the emission spectra can be extracted from the streak camera images by integrating the measured intensities over time for each separate wavelength. Thus, it is obvious from the lower row in Fig. 4.7 that the emission spectra of both, Alq₃ and LR, can be measured simultaneously for sample C, what is in good agreement with the results from the cw experiment mentioned before.

Furthermore, it is possible to determine the excited states lifetimes for both organic dyes for the different samples. Figure 4.8 illustrates the time-dependent behavior of the emission intensities of the emitting molecules. Thereby, the integration over the wavelength was performed over the whole emission spectrum for sample A and B, while only the range between 600 nm and 700 nm (emission of LR) was used in the case of sample C. Using mono-exponential decay functions (see Eq. 4.6) for samples A and B results in appropriate fits yielding excited states lifetimes of 14.8 ns and 3.3 ns for Alq₃ and LR, respectively, although the emission zone is very broad and not fixed in the thick PMMA layers due to laser excitation, and the decay time depends on the emitter/metal distance, as will be discussed in detail in chapter 5. However, the determined excited states lifetime of Alq₃ is very close to the published value (14.7 ns) of Andrew and Barnes

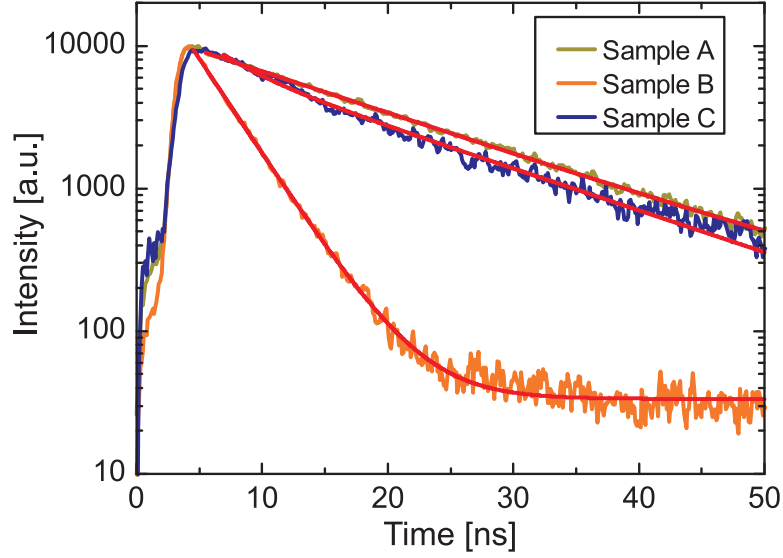


Figure 4.8: Measured time-dependent intensities for the three different samples presented in Fig. 4.7. The excited states lifetime of Alq₃ was determined to 14.8 ns (sample A, green line). Lumogen Red exhibits an excited states lifetime of 3.3 ns in the case of sample B (orange line). The excited states lifetime of LR for sample C (blue line) cannot be fitted in a satisfactory way with a mono-exponential function, but the result is suitable using a bi-exponential decay function resulting in a short excited states lifetime of 3.3 ns and a long-living contribution with an excited states lifetime of 14.7 ns. This clearly gives a strong evidence for the assumed energy transfer process via near-field coupling by SPPs. The red lines represent the fits for the excited states lifetime determination for each curve. Graphic taken from Ref. [62]

for a similar experiment [89]. It should be noted, that the excitation of sample C was performed through the glass substrate and only little laser intensity should be absorbed by the PMMA:LR emitting system due to the reflecting silver layer, while the emission was detected on the LR-side. However, a strong emission in the range between 600 nm and 700 nm is clearly detectable (see Fig. 4.7). Analyzing this photoluminescence decay signal in more detail leads to the result that a mono-exponential fitting curve does not represent the measured emission data of the LR molecules in a proper way. Therefore, a bi-exponential ansatz for the fitting process was assumed, leading to the following fit function:

$$I(t) = I_1 \cdot \exp(-t/\tau_1) + I_2 \cdot \exp(-t/\tau_2) + C. \quad (4.7)$$

Therein, analogous to Eq. 4.6, I_1 and I_2 represent the intrinsic intensities of two processes with different lifetimes τ_1 and τ_2 , respectively, emitting in the same wavelength region. Fitting the measured photoluminescence time-dependent behavior of sample C in

the LR wavelength region with Eq. 4.7 results in a short excited states lifetime of 3.3 ns and a much longer decay time of 14.7 ns. As can clearly be seen from Fig. 4.8 and as a result from the fitting procedure, the intensity of the long-living part of the LR emission is much higher as the fraction exhibiting a short excited states lifetime. This means, that a (small) amount of LR molecules is excited directly by the incident laser light decaying with its intrinsic excited states lifetime of 3.3 ns, as was measured for sample B, which only contains LR as emitting molecules, and a huge part of the measured photoluminescence signal originates from the energy absorbed by the PMMA:Alq₃ layer and afterwards transferred via near-field coupling by SPPs at the organic/metal interface to the LR molecules located near the silver layer. If this transfer process would be much faster than both decay times of the emitting molecules, one would expect, that there exists a LR signal with an excited states lifetime in the range of the Alq₃ molecules. This is obviously the case, and thus this is a very strong evidence for the assumed energy transfer mechanism in perfect agreement with the cw measurements mentioned before [85] and already published results [89,91].

Triplet-Polaron-Quenching

A second exemplary measurement type allows to analyze quenching processes at high current densities in organic light-emitting diodes as already mentioned in section 2.2.2. Therefore, a combination of electrically and laser induced excitation as it was first published by Giebink and Forrest [48] is essential. With an electrical square wave pulse it is possible to choose a working point of the OLED without stressing the device too much in order to preclude degradation effects. The laser pulse during the electrical excitation is then probing the excitonic processes for an adjusted current density. A schematic sketch of the pulse sequence in a combined EL-PL-experiment is given in Fig. 4.9. Here, the time-resolved luminescence signal of a green phosphorescent OLED containing Ir(ppy)₃ as emitter is demonstrated. A 50 μ s long electrical pulse was superimposed by a short laser excitation with a repetition rate of 20 Hz. It is mandatory to choose the pulse length of the electrical excitation in a proper way. It should be long enough to ensure steady state conditions due to the slow rising of the current through the device as a result of the long RC-times ($\approx 1 \mu$ s) of the devices used in this study, on the other side it should be short enough to minimize degradation effects during the measurement. Moreover, the optical excitation should not increase the exciton density inside the emission layer strongly to avoid additional bi-molecular quenching processes. To clarify the pulse sequence, the electrical and the optical excitations are marked in Fig. 4.9 as dashed lines.

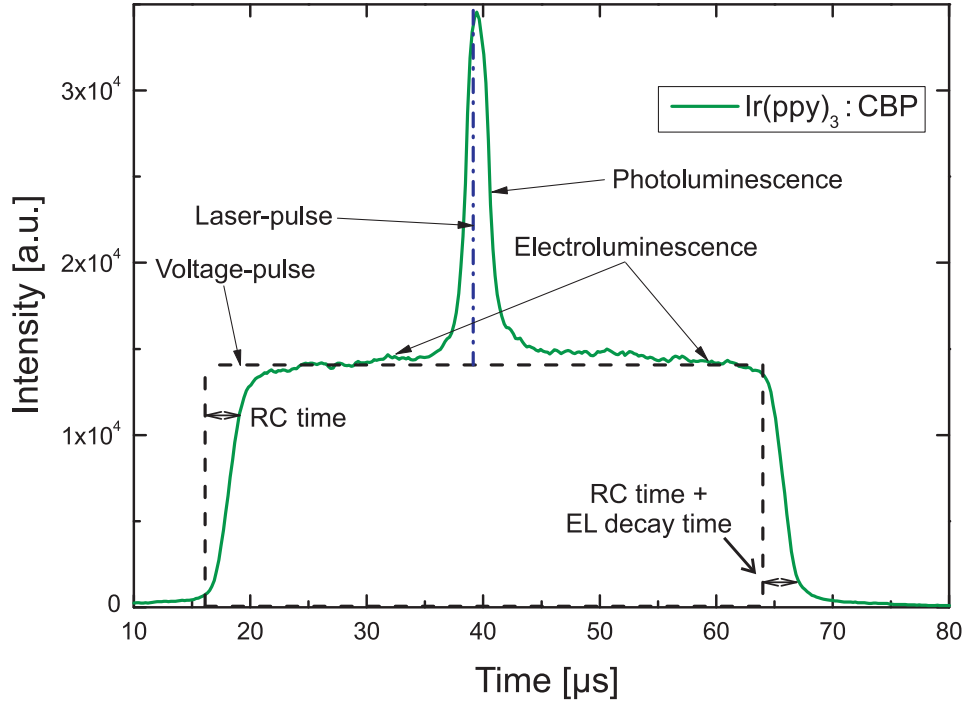


Figure 4.9: Time-resolved luminescence signal of a phosphorescent green OLED containing Ir(ppy)_3 as emitter during combined pulsed electrical and optical excitation. The width of the photoluminescence signal in this diagram is artificially enhanced due to the limited pixel density of the streak camera system. In order to detect the photoluminescence decay in a proper way, a shorter time-resolution was chosen in the actual experiment.

In order to analyze triplet-polaron-quenching processes in UNA OLEDs, a device very similar to that in Fig. 3.1 was fabricated. For more information about the detailed stack layout and fabrication process it should be referred to Ref. [92]. The device under investigation exhibits an active pixel size of 4 mm^2 to simplify the optical excitation. The measurement sequence presented in Fig. 4.9 was used to analyze the excited states lifetime behavior as a function of the current density through the device. Therefore, a variable square wave voltage pulse with a duration of $25\text{ }\mu\text{s}$ and a repetition rate of 20 Hz was applied to the device. The pulse length was chosen shorter than for the example in Fig. 4.9 to avoid degradation effects due to electrical stressing. During the electrical excitation a short laser pulse (337.1 nm wavelength, 700 ps pulse length) was superimposed in the middle of the electrical pulse. Afterwards the time-resolved photoluminescence signal was detected with the streak camera system. This allows for an analysis of the excited states lifetime inside the OLED stack during electrical excitation.

Figure 4.10 shows the IVL characteristics of the device before and after the pulsed measurement sequence for several different current densities. Obviously, the device was

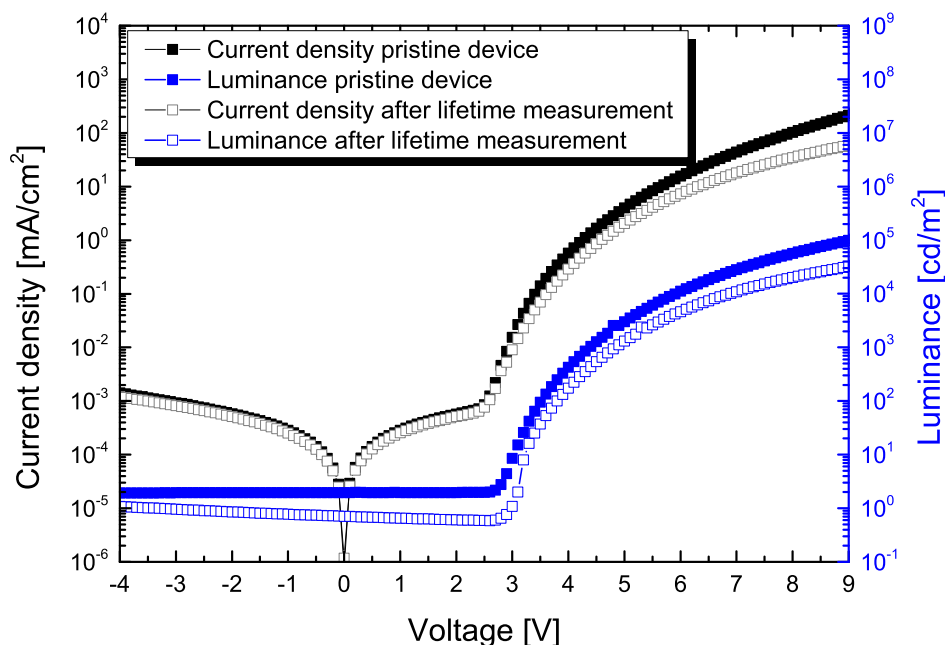


Figure 4.10: Comparison of the IVL characteristics before and after the pulsed lifetime measurements. Although the electrical excitation was quite short, a clear degradation due to the measuring process is detectable. Graphic taken from Ref. [92].

stressed by the measurement and degradation is clearly detectable. Not only the current density, but also the luminance output for a certain voltage decreases. Therefore, an appropriate error estimation for the current density should be used in the analysis of the excited states lifetime behavior.

The exemplary comparison of two photoluminescence decay curves for different applied voltages is presented in Fig. 4.11 a). For a better comparability the intensities have been normalized. However, a clear difference in the excited states lifetime of the emitting molecules is detectable. While Ir(ppy)_3 exhibits an excited states lifetime of $0.7\text{ }\mu\text{s}$ if no voltage is applied to the device, this value decreases to $0.5\text{ }\mu\text{s}$ for an applied voltage of 3.3 V resulting in a current flow of $j \approx 7 \cdot 10^{-3}\text{ mA/cm}^2$ through the OLED. This decrease can be explained by a quenching-induced increase of the non-radiative rate of the emitting species [48]. This is a remarkable reduction of about $1/3$ of the initial value of the excited states lifetime even for very low current densities. This gives a hint for a very susceptible device for current induced quenching processes. Moreover, all determined excited states lifetimes could be analyzed by mono-exponential fit functions,

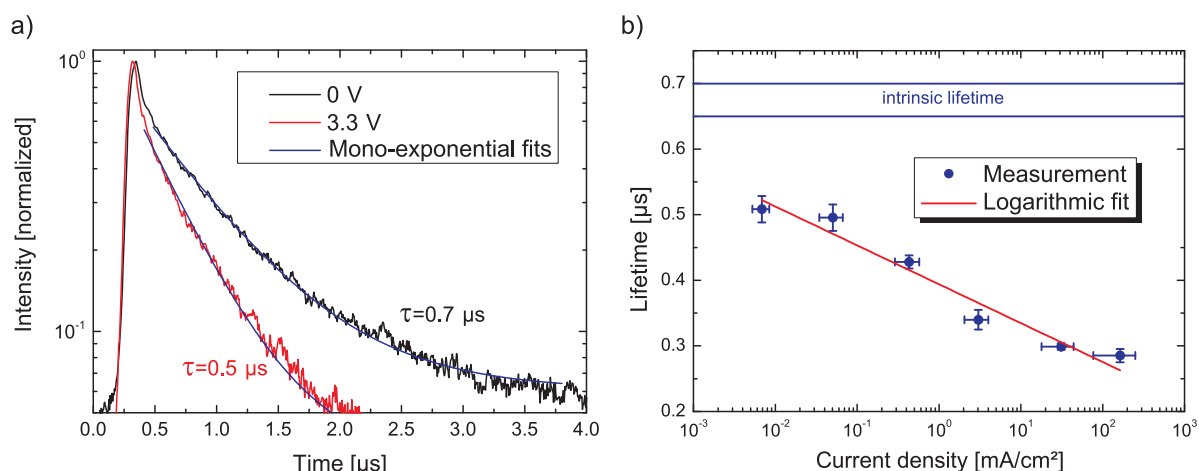


Figure 4.11: a) Time-resolved intensity behavior without applied voltage (black) and with an applied voltage of 3.3 V (red). The blue lines represent mono-exponential fits resulting in an excited states lifetime of $0.7 \mu\text{s}$ and $0.5 \mu\text{s}$ for the measurement without and with applied voltage, respectively. b) Decrease of the excited states lifetime (blue points) with current density. The red line is a logarithmic fit. Error bars in horizontal direction originate from the degradation process during the measurement (see. Fig 4.10). Graphics taken from Ref. [92].

which is an evidence that TPQ is the predominant quenching effect for high current densities in the device under investigation and other quenching processes such as TTA, which would result in a bi-exponential photoluminescence decay, are only playing a secondary role.

The excited states lifetime behavior as a function of the current density through the device is illustrated in Fig. 4.11 b). For a better visualization, the intrinsic lifetime of the Ir(ppy)_3 molecules inside the OLED structure without an applied external voltage is shown as horizontal solid line. Interestingly, the intrinsic excited states lifetime is not reached even for current densities of about $10^{-2} \text{ mA}/\text{cm}^2$. This gives a hint for strong current induced and/or field induced quenching effects for this devices. However, it can clearly be seen, that the decrease of the excited states lifetime can be fitted in a reasonable way with a logarithmic function. This gives evidence that there is a direct correlation between efficiency decrease in organic light-emitting diodes at high current densities and the triplet-polaron-quenching induced reduction of the excitonic lifetime due to an increase of the non-radiative rate of the emitting species. This is in a qualitatively good agreement with previously published results [48].

COMPREHENSIVE EFFICIENCY ANALYSIS OF OLEDs

This chapter examines the key parameters that have to be considered to achieve a comprehensive efficiency analysis of state-of-the-art organic light-emitting diodes. If only the external quantum efficiency of OLEDs is measured, e.g. in an integrating sphere or by a zero degree measurement with a calibrated photodiode assuming a lambertian emission profile [93], one would not have clear information about the individual contributions of the four determining factors (charge carrier balance, radiative exciton fraction, effective radiative quantum efficiency and outcoupling factor; see Eq. 2.9). Therefore, it is a crucial point for the efficiency analysis of OLEDs to investigate each of the four factors precisely for a deep understanding of the underlying (photo-)physical processes, in order to improve device performance. Thus, this chapter will present methods to analyze all four factors in a proper way.

First, the problems of a determination of the radiative quantum efficiency of an emitting system via simple integrating sphere measurements will be discussed for both electro- and photoluminescence experiments.

Second, an approach to determine the intrinsic radiative quantum efficiency (RQE) of an emitting guest/host system for simplified structures will be presented. Therefore, it is essential to perform excited states lifetime measurements for an ensemble of samples with a subsequent variation of the distance of the emitter to a highly reflecting interface such as a metallic layer. Hence, an optical spacer that is not absorbing in the (visible) range of the luminescence spectrum of the emitting species is required. Thus, two differ-

ent optical spacers, SiO_2 and LiF , with a variable thickness, which have been sandwiched between a silver and the emitting layer, have been used in this study. Comparing the measured excited states lifetimes for the varying emitter/metal distance with optical simulations presented in sec. 2.3.2 results in a determination of the RQE of the used emitting guest/host system.

However, the intention of this chapter is to analyze complex OLED structures. For this reason a similar experiment using a complete OLED will be illustrated in the third section. Here, an additional highly reflecting layer is introduced to a standard stack. This layer is placed between the transparent anode and the emission layer of the device and is acting as a second mirror (the first mirror is the metallic cathode) in order to enhance the microcavity induced Purcell effect. With a variation of the reflectivity of this (silver) layer, what is accomplished by its thickness, it is possible to determine the radiative quantum efficiency and the intrinsic excited states lifetime of the emitting system under investigation by, again, a comparison of simulations with measured time-resolved data points.

The problems of this procedure are the strong changes of the electrical characteristics of the samples with varying microcavity strength, which is impractical for state-of-the-art OLEDs. Thus, the first presented approach was modified to provide electrical compatibility of the different samples and a determination of the RQE of an emitting system with optical time-resolved spectroscopy. Additionally, this method allows for an electrical investigation of the radiative quantum efficiency, too. Therefore, a subsequent variation of the emitter/cathode distance is achieved by introducing diverse layer thicknesses of a conductivity doped electron transporting material. Due to the doping of the ETL, the conductivity of this layer is independent of its actual thickness and therefore the electrical properties are not changing for devices with unequal ETL thicknesses. Hence, measuring both the electrical driven EQE, with and without an outcoupling enhancement to get access to the substrate modes of the OLED, and the (optical) excited states lifetime and comparing these findings with simulations allows for an analysis of the charge carrier balance and the radiative quantum efficiency of the used guest/host system.

Therewith, the influence of the matrix material on the RQE of the emitting species will be investigated, first. Afterwards, the current dependent decrease of the RQE of a state-of-the-art OLED will be analyzed by measurements of the external quantum efficiency.

With a more detailed consideration of the observed investigations it is furthermore possible to account for changes of the outcoupling factor of the device due to orientation effects of the transition dipole moment of the emitting molecules. Ignoring this feature would lead to wrong estimations of the outcoupling factor and therewith of the radiative quantum efficiency for (phosphorescent) OLEDs, resulting in an erroneous simulation of the power dissipation into the different optical modes. The situation will become even more complex in fluorescent devices, because additionally the radiative exciton fraction could be evaluated in a wrong way if emitter orientation is not taken into account properly. Moreover, the possible efficiency enhancement due to the introduction of horizontally oriented emitting systems will be pointed out.

In order to complete the presented method, an efficiency analysis for an oriented, fluorescent emitter will be performed, including a possible deviation of the classically assumed radiative exciton fraction due to triplet-triplet-annihilation or thermally activated delayed fluorescence. Therewith, it is possible to get access to all four factors determining the external quantum efficiency of organic light emitting diodes. Therefore, the elaborated approach allows for calculating the power dissipation into the different optical energy channels for an OLED stack with arbitrary layer thicknesses and hence an optimization of the device is possible.

Figure 5.1 shows a schematic sketch of the experimental techniques used in this chapter. Time-resolved photo- and electroluminescence spectroscopy was applied to investigate the excitonic lifetimes inside different emitting systems. With a systematic variation of the cavity strength at the position of the emitter it is possible to determine the radiative quantum efficiency of guest/host emitting systems. This is essential to achieve a consistent efficiency analysis. Therefore, samples with increasing complexity, from simplified stacks to complete state-of-the-art OLED structures, have been investigated (see Fig. 5.1 a). With the complete OLEDs it is additionally possible to compare the findings from the excited states lifetime experiments with EQE measurements performed in integrating spheres (see Fig. 5.1 b)). Thus, more precise results for the efficiency analysis can be achieved, in particular if non-isotropic emitter orientation is present. Furthermore, for the efficiency analysis of fluorescent OLEDs (see sec. 5.5) it is essential to combine both techniques. If only one method is used for the efficiency analysis, wrong estimation especially for the radiative exciton fraction of the devices may follow. This results in erroneous calculation of power dissipation to the different optical modes. With this approach it was possible to perform a consistent, comprehensive efficiency analysis of OLEDs consisting of a blue fluorescent emitting material showing thermally activated delayed fluorescence, without requirement of adhoc predictions.

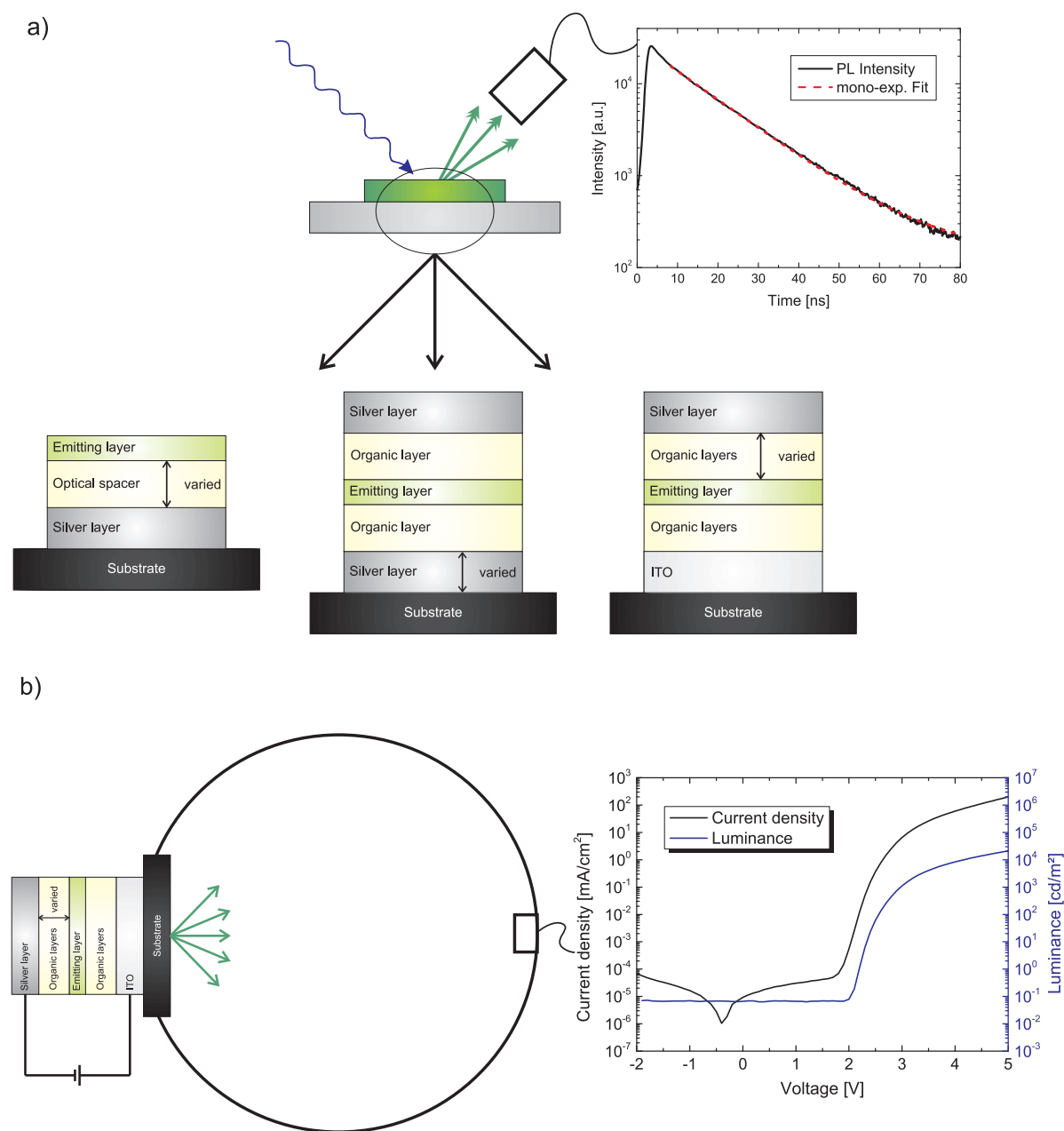


Figure 5.1: Schematic sketch of the primarily used experimental techniques in this section. a) Time-resolved photoluminescence spectroscopy for samples with different complexity for investigating the excited states lifetime of the emitting molecules. b) Integrating sphere measurements of the external quantum efficiency of complex state-of-the-art OLEDs.

5.1 RQE determination via integrating sphere measurements

The determination of the radiative quantum efficiency q of an organic emitting system is essential for a comprehensive efficiency analysis in organic light-emitting diodes. Typically, the RQE of an emitting molecule is measured in a simple photoluminescence experiment using an integrating sphere. Usually, the molecules are therewith diluted in a solvent and the emitted photons divided by the number of absorbed photons yields the PL quantum efficiency. However, the situation can change drastically in a thin film [94]. Hence, the RQE of thin films of a pure organic material or solid solutions should be investigated [95]. Although, a thin film experiment is much closer to the real situation in an OLED, there are some important aspects, that have to be taken into account to achieve consistent results. First, the influence of interference effects and the power dissipation to different optical modes is not neglectable. Due to the Purcell effect, an effective RQE is measured in this experiment (see sec. 2.2.2 and 2.3.2) and an additional reduction of the real value of emitted photons by coupling to waveguided or substrate modes is possible (see sec. 2.3.1). Moreover, if orientation effects occur for the emitting system under investigation, the analysis becomes more complicated. Indeed, the angle and the polarization of the incident optical excitation beam can play an unexpected role, because a certain emitter orientation could be preferred [96], which would not be the case for an electrically driven experiment (e.g. for an OLED). Furthermore, the power distribution between the different optical modes is strongly depending on the orientation of the transition dipole moments of the emitting molecules. This could lead to a significant underestimation of the RQE of an emitting system, if a prevailing vertical emitter orientation is present.

In order to demonstrate the problems with PL quantum efficiency measurements in an integrating sphere using thin films on a glass substrate, simulations of the power dissipation spectra for different emitter orientations have been performed for a 20 nm thick CBP film doped with 6.5 wt% of the green phosphorescent emitting molecule Ir(ppy)₃. The results are presented in Fig. 5.2. The amount of dissipated energy is indicated by different colored areas. White lines represent the borders of the optical modes (1: direct emission to air, 2: substrate modes, 3: waveguided modes, 4: surface plasmon polaritons). Certainly, no waveguided modes and no coupling to SPPs is present in the simulated results, due to the (too) small layer thickness of the organic material and the missing metal layer, respectively. However, it can clearly be seen that, especially for a vertical emitter orientation, a huge part of the power dissipated by the emitting

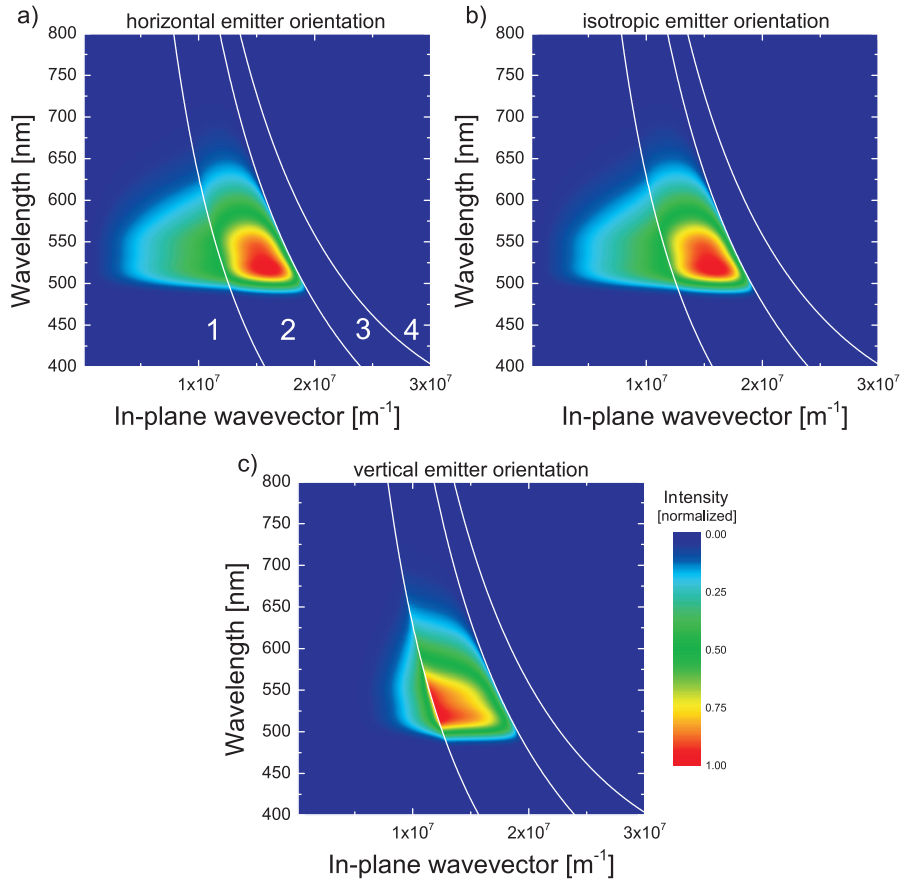


Figure 5.2: Simulations of the power dissipation spectra of a 20 nm thick CBP film doped with 6.5 wt% Ir(ppy)₃ on a glass substrate for a) horizontal, b) isotropic and c) vertical emitter orientation. The color is representing the intensity of emission. White lines are illustrating the borders of the different optical modes. Area 1: direct emission to air, 2: substrate modes, 3: waveguided modes, 4: surface plasmon polaritons. While the situation is rather similar for horizontally and isotropically oriented transition dipole moments, the power distribution between the two present optical modes, namely emission to air and substrate modes, is strongly differing for an assumed vertical emitter orientation.

molecules is coupled to substrate modes and is therewith primarily lost for the measurement. Indeed, if the edges of the glass substrate are not blackened, a major part of the captured light can be extracted there, but some photons are (re)absorbed by the organic layer or by the glass substrate and cannot contribute to the PL quantum efficiency. Furthermore, quenching effects at surfaces or interfaces [97], especially for thin organic layers, should be considered in such experiments. Strictly speaking, the coupling to substrate modes does not effect the measurement to a great extent, but should be taken into account especially if vertical emitter orientation is present, whereas the

influence of the mentioned Purcell effect can be distorting the result in a reasonable way. The Purcell effect changes the intrinsic RQE of an emitting system to an effective one and has the highest absolute impact for moderate quantum efficiencies in the range of 30–70 %. Due to total internal reflection, especially caused by the huge refractive index discrepancy at the organic/air interface, the Purcell factors for all three different emitter orientations are considerably smaller than unity ($F_{\theta=0} = 0.59$, $F_{\theta=1/3} = 0.64$ and $F_{\theta=1} = 0.06$), resulting in a decrease of the radiative rate of the emitting molecules and therewith a reduction of the effective RQE. Particularly, in the case of vertically oriented transition dipole moments the radiative rate would be almost completely suppressed, yielding a very low effective RQE even if the intrinsic value were be very high. These results clarify the importance of taking the Purcell effect into account, actually for such a simple experiment as the determination of the RQE of an emitting (guest/host) system via integrating sphere measurements. It should be noted, that the error for this approach is highest if a (prevailing) vertical orientation of the emissive dipole moments of the emitting molecules is present. However, the destructive interference conditions are predominantly caused by the very low thickness of the organic material and can be strongly reduced, if a higher thickness is used for this experiment. Though, other effects such as coupling of energy to waveguided modes can appear which strongly influences the investigated effective RQE.

Moreover, the RQE of an emitting system can be influenced by different layer growth induced by the underlying materials [98,99], such as it is the situation inside an OLED. Therefore, the determination of the RQE in an integrating sphere is not practicable for complex OLED structures. In an electrically driven experiment, it would be very difficult to extract the RQE of the emitting system, because the measured EQE is determined by four factors (see Eq. 2.9), which are not a priori known for every OLED stack. In a photoluminescence experiment, other layers than the emission layer can also absorb light, which would lead to erroneous results. Hence, another method should be used for investigations of the RQE of an emitting system inside OLED structures, which will be presented in the next sections.

5.2 RQE determination using simplified structures

As mentioned in the former section, it is essential to determine the radiative quantum efficiency of an emitting system inside a complex OLED structure to ensure a consistent efficiency analysis, which is a crucial point in terms of device optimization by layer thickness adjustment. Hence, an approach suggested by Drexhage et al. [69], who analyzed the RQE of an emitter via excited states lifetime measurements, is verified by simplified structures in order to extend and modify the procedure for emitting molecules embedded in an OLED. This experiment is based on a systematic variation of the distance of an emitting system to a highly reflecting interface (e.g. a metal layer) via an optical spacer, resulting in a Purcell effect induced modification of the excited states lifetime. As can be seen from Eq. 2.23 the relative changes of the excitonic lifetimes for different emitter/metal distances are a function of the Purcell factor and the intrinsic radiative quantum efficiency of the emitting molecules. Thus, comparing time-resolved measurements with simulations yields the RQE of the emitting system under investigation. Figure 5.3 shows the principle stack layout of the used simplified structures.

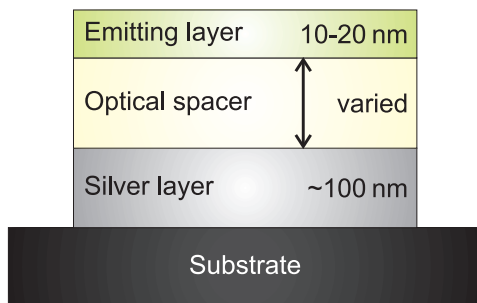


Figure 5.3: a) Stack layout of simplified structures used for the RQE determination of an emitting system via changes of the excited states lifetime. A substrate (e.g. a Si wafer or glass) is coated with an adhesion layer (e.g. titanium or a polymer) to achieve good connection of the following silver layer. The thick silver layer (≈ 100 nm) is acting as a nearly ideal mirror. The mirror is followed by an optical spacer (e.g. SiO_2 or LiF) with a variable thickness. Finally the emitting system under investigation is superimposed by spin coating or evaporation techniques.

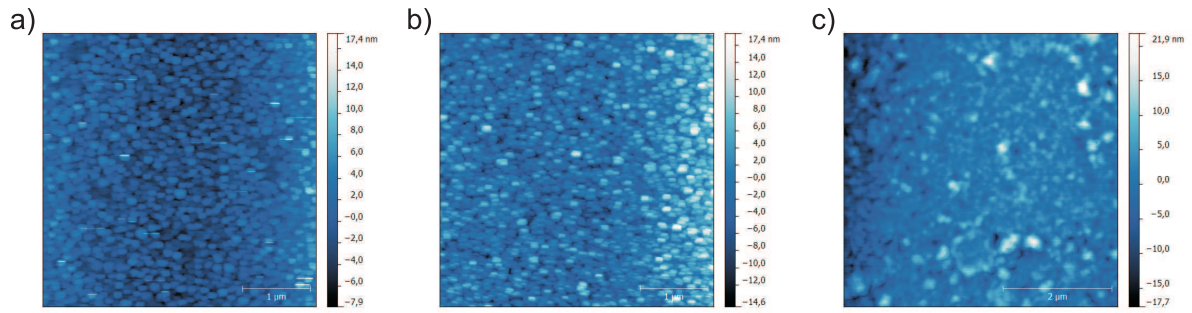


Figure 5.4: AFM images of the surfaces of a) the silver layer, b) the SiO₂ spacer and c) Ir-SC4 doped into a PMMA matrix. Graphics were taken from Ref. [100].

5.2.1 Using SiO₂ as optical spacer

All results of this subsection have been accomplished in cooperation with Benjamin Lebsanft in the scope of his diploma thesis [100].

In order to investigate the radiative quantum efficiencies of different emitting systems, the stack presented in Fig. 5.3 has been fabricated for different spacer thicknesses. A silicon wafer was used as substrate, covered with a thin titanium layer (1 nm) as adhesion layer for the following silver layer (100 nm). Both layers have been fabricated by electron beam deposition. Thereafter, the optical spacer (SiO₂) with differing thickness was sputtered on top of the silver, which was subsequently capped with the organic material under investigation. For more details about the fabrication process, please refer to Ref. [100]. Exemplarily, the RQE investigation of the phosphorescent Ir(ppy)₃ derivative fac-tris[2-(2-pyridinyl-kN)(5-(3,4-bis(2-methylpropyloxy)phenyl)phenyl)-kC]-iridium(III) (Ir-SC4, molecular structure shown in Fig. 3.1) is discussed in the following. This material is very stable even in ambient atmosphere and can easily be dissolved in e.g. chloroform. Hence, the emitting molecules have been spin coated on top of the SiO₂ layer, doped with 4.5 wt% in a PMMA matrix using a mixture of chloroform and methylbenzene as solvents. This concentration was chosen to avoid concentration induced decrease of the energy transfer from the matrix to the emitting molecules [101] and bi-molecular quenching effects such as TTA.

To ensure that the investigations are not influenced by unintended scattering and quenching effects due to very rough surfaces of the different materials and because the simulation tool can only simulate perfectly smooth interfaces, atomic force microscopy (AFM) measurements of the silver mirror, the optical spacer (SiO₂) and the emitting system have been performed. The results are shown in Fig. 5.4, yielding root-mean-squar (RMS) roughnesses of 1.8 nm for the silver layer and 3.2 nm for the following SiO₂

spacer. However, the final Ir-SC4:PMMA layer exhibits a smoother RMS roughness than the underlying SiO₂ layer due to the spin coating process. Therewith, an appropriate smoothness is provided for the used fabrication process and hence the basis for the intended experiment is given.

The next crucial point is an acceptable determination of the layer thicknesses of the optical spacer of the samples under investigation. The silver layer thickness is of no consequence, if it is thicker than ≈ 100 nm, because beyond that value one can treat this layer as a nearly perfect mirror in the visible range of light. More important is the thickness of the emitting system. It should be thick enough to ensure an appropriate photoluminescence signal but has to be as thin as possible to provide the accuracy to perform the simulations with a δ -shaped emission zone. Both thicknesses have been checked by profilometry (Veeco Dektak). Due to the spin coating process of the Ir-SC4:PMMA layer, it was not possible to fabricate thinner layers than 50 nm that would be self-contained over the whole sample area. Nevertheless, the simulation was performed with an infinitely narrow emission zone in the middle of the organic layer and the mistake caused by the real thickness (50 nm) was considered by an error estimation in the analysis of the results. However, the most significant value is the thickness of the optical spacer. First, the thicknesses of the sputtered SiO₂ layers were determined by ellipsometry (Sentech SE850). Unfortunately, the fits of the measurements that are required for thickness determination have been ambiguous due to the underlying silver layer, and hence the accuracy was not acceptable. Thus, an approach for the determination of the SiO₂ thickness from photoluminescence 0°-spectra was established. Therefore, a computer program compared the peak positions of the measurements with the simulated emission spectra from the simulation tool. Therewith, it was possible to determine the optical spacer thickness with an accuracy of ± 2.5 nm, because the simulation was performed with a 5 nm step width of the SiO₂ thickness. Figure 5.5 demonstrates this method, resulting in an optical spacer thickness of 375 nm. The measured and the simulated photoluminescence spectra show a very good agreement.

With these preliminary considerations it is now possible to determine the radiative quantum efficiency of the emitting system via the changes of its excited states lifetime. The excitation was performed by a nitrogen laser (see sec. 4.3.1) with a wavelength of 337.1 nm. Hence, predominantly the matrix material PMMA is excited by the laser pulse due to the low doping concentration of the Ir-SC4 molecules [100]. After the excitation of the PMMA matrix, the absorbed energy is transferred via a singlet-singlet transfer to the emitting molecules. Typically, this transfer process is in the range of nanoseconds [90], depending on the efficiency of the transfer and the energetic position

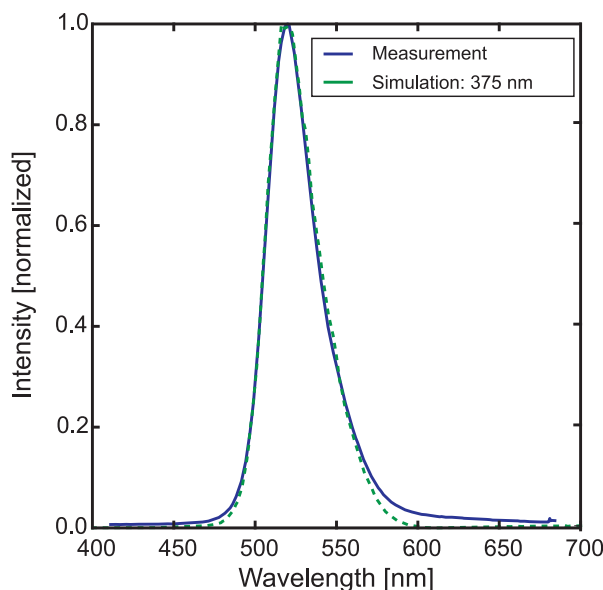


Figure 5.5: Determination of the SiO_2 layer thickness via comparison of the emission spectra with simulated data for samples with the structure $(\text{Si}/\text{Ag}/\text{SiO}_2/\text{Ir-SC4:PMMA})$. Graphic was taken from Ref. [100].

of the excited and ground states of matrix and emitter. In the case of the emitting system under investigation, the intrinsic lifetime of the Ir-SC4 molecules ($1.49 \mu\text{s}$) is increased due to a suboptimal energy transfer [102], which leads to the assumption of a reduced RQE of the Ir-SC4 molecules compared to a measurement in a solvent.

The results of the time-resolved photoluminescence measurements are shown in Fig. 5.6. The excited states lifetimes of the emitting molecules are determined by exponential fits for the different optical spacer thicknesses. Due to the mono-exponential decay behavior for all measured samples, bi-molecular quenching processes can be excluded. Exemplarily, the photoluminescence decay and the mono-exponential fit for the sample exhibiting a SiO_2 thickness of 250 nm are illustrated in Fig. 5.6 a), showing a very good agreement of the fit with the measured signal for more than three orders of magnitude. Hence, the estimated error for the excited states lifetimes is very low. Moreover, photoluminescence spectra for the different SiO_2 thicknesses have been extracted from the time-resolved measurements. These spectra are used for the spacer thickness determination mentioned before. It can clearly be seen from Fig. 5.6 b), that the spectra change remarkably, not only in the intensity but also in their shape and peak positions, with the variation of the emitter/mirror distance as a result of the interference effects explained in sec. 2.3.

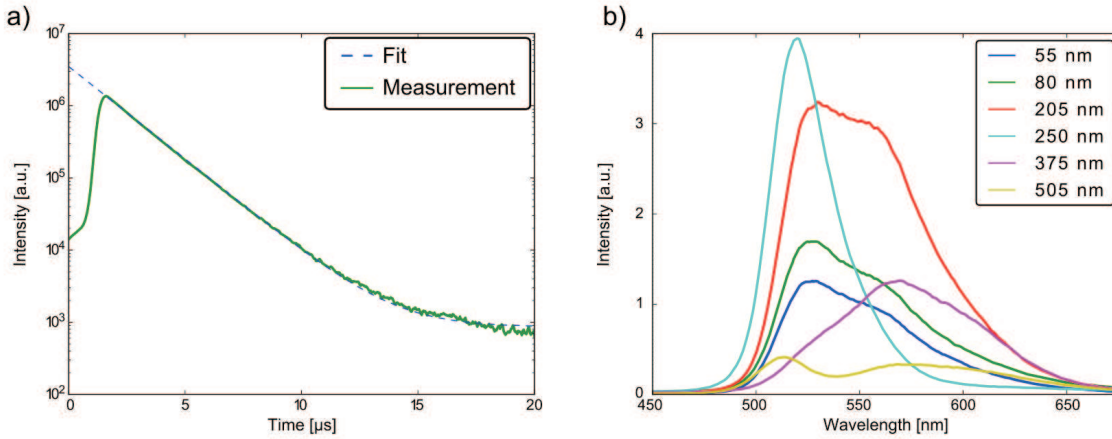


Figure 5.6: a) Exemplary photoluminescence signal of the Ir-SC4 emission for an optical spacer thickness of 250 nm (sample structure: Si/Ag/SiO₂/Ir-SC4:PMMA). The excited states lifetime could be fitted with a mono-exponential fit resulting in $\tau = 1.67 \mu\text{s}$. b) Photoluminescence spectra for the available spacer thicknesses. The relative heights of the spectra can differ from the simulated behavior due to the setting of the samples. Graphics are taken from Ref. [100].

With these results, it is now possible to perform the determination of the RQE of the emitting system via a comparison of the measured data with simulations. Figure 5.7 a) shows the simulated behavior of the Purcell factor as a function of the optical spacer thickness assuming a δ -shaped emission zone in the middle of the organic layer and an isotropic emitter orientation. The isotropic orientation was assumed due to the very similar chemical structure of Ir-SC4 and Ir(ppy)₃, which shows isotropic orientation of its emissive dipole moments. However, the simulation shows considerable oscillation with the SiO₂ thickness as a result of e.g. constructive and destructive interference effects and the different coupling to optical modes for different emitter/mirror distances. Using these simulated values for the calculation of the relative lifetime changes as a function of the radiative quantum efficiency of the emitting system (see Eq. 2.23) and the SiO₂ thickness, and comparing the obtained characteristics with the measured excited states lifetimes normalized by the intrinsic value of the emitting species yields an estimation of its intrinsic radiative quantum efficiency. As can be seen from Fig. 5.7 b) the measured data points are not following one of the simulated lines over the whole SiO₂ thickness variation, but they are oscillating between the simulation for an RQE of 80 % and 60 %. Hence, the RQE of Ir-SC4 doped in a PMMA matrix can be rated to $(70 \pm 10) \%$. Due to a lack of a larger number of available data points, especially in the range of 100 – 350 nm SiO₂ thickness, it is not possible to determine a more precise value for the RQE. Due to

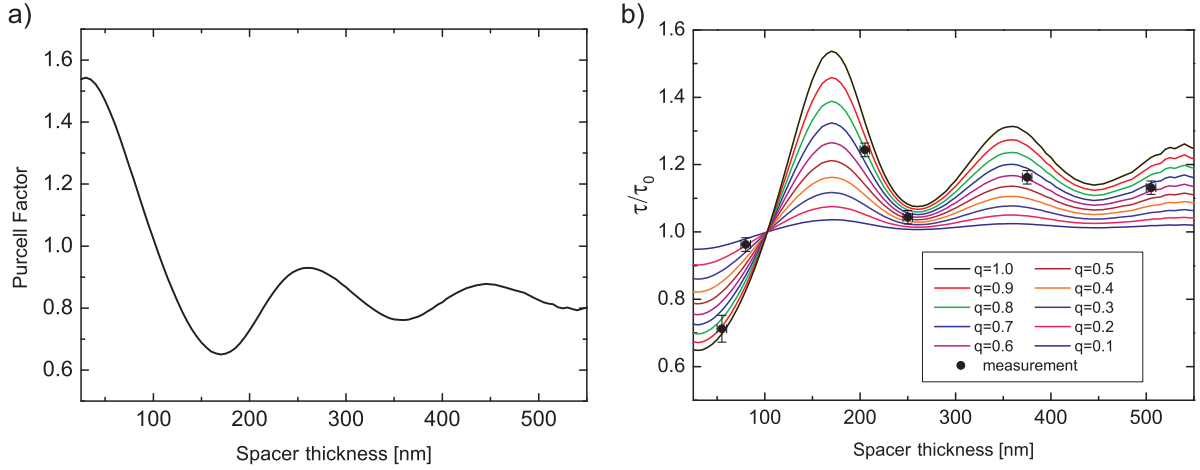


Figure 5.7: a) Simulation of the Purcell factor of the simplified structure under investigation (Si/Ag/SiO₂/Ir-SC4:PMMA) as a function of the SiO₂ thickness. b) Determination of the radiative quantum efficiency of Ir-SC4 doped in a PMMA matrix. Dots represent measured lifetimes normalized with the intrinsic value ($\tau_0 = 1.60 \mu\text{s}$), while solid lines illustrate the simulated behavior of the relative changes of the excited states lifetimes with spacer thickness and for different RQEs. Graphic 5.6 b) was taken from Ref. [100].

protracted problems with the sputter chamber, it was not possible to fabricate samples with the required optical spacer thicknesses. Therefore, another material than SiO₂ has to be used for this kind of experiment. As an alternative, LiF was chosen as optical spacer, as will be discussed in detail in the following subsection.

5.2.2 Using LiF as optical spacer

Corresponding to the previous section, the radiative quantum efficiency of an organic emitting guest/host system was analyzed using the simplified sample structure shown in Fig. 5.3 with LiF instead of SiO₂ acting as optical spacer. The emitting system under investigation was Ir(ppy)₃ doped with 2 wt% in a CBP matrix. All results of this subsection have been accomplished in cooperation with Johannes Braun in the scope of his bachelor thesis [103].

LiF was the material of choice, due to the possibility of evaporation in the already available vacuum chamber. Therewith, it is possible to fabricate 16 samples exhibiting a thick silver layer acting as mirror, different LiF layer thicknesses as optical spacer and the emitting guest/host system without breaking the vacuum. In order to simplify the sample preparation, the adhesion layer titanium was substituted by a compound of two polymers poly(3,4-ethylenedioxythiophene):poly(styrenesulfonate) (PEDOT:PSS, struc-

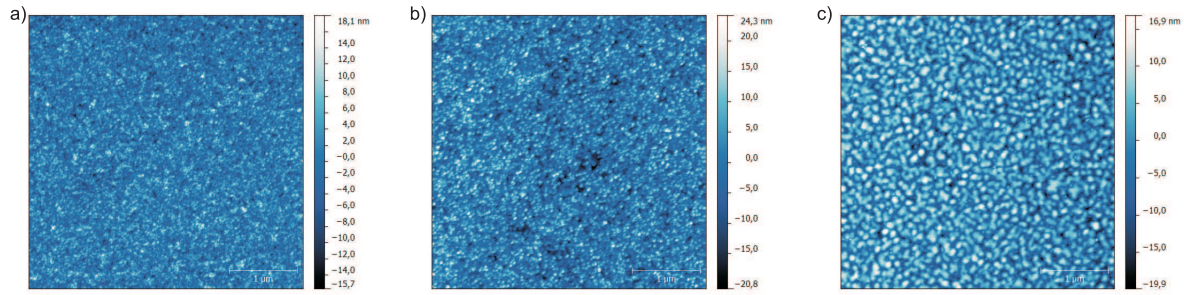


Figure 5.8: AFM images of the surfaces of a) the silver layer, b) the LiF spacer and c) Ir(ppy)₃ doped into a CBP matrix. Graphics were taken from Ref. [103].

ture shown in Fig. 3.1) that can be spincoated on a glass substrate and should smoothen the growth of the following silver layer [104]. For more information about the fabrication process of the samples, please refer to Ref. [103].

One additional advantage of using LiF is that it is possible to fabricate patterned samples, that allow for a thickness determination of all used layers after the measuring process with simple profilometry, and do not need complicate approaches as developing computer programs or in this case the often inaccurate ellipsometry.

However, in order to analyze the functionality of LiF as optical spacer, the RMS roughness (R_{RMS}) of the surfaces of the important layers has been checked via AFM measurements. According to the results of sec. 5.2.1, the RMS roughness of all layers are acceptable ($R_{\text{RMS,Ag}} = 3.9 \text{ nm}$, $R_{\text{RMS,LiF}} = 6.1 \text{ nm}$ and $R_{\text{RMS,Ir(ppy)}_3\text{:CBP}} = 5.7 \text{ nm}$). The AFM images of the relevant surfaces are shown in Fig. 5.8.

Due to the much easier fabrication process, it was possible to produce 25 samples with different optical spacer thicknesses between 17 and 305 nm on top of the 100 nm thick silver layer. The emitting system was excited with a 337.1 nm laser pulse for the time-resolved measurements. Unfortunately, inaccuracies during the measurement complicated the analysis of the excited states lifetimes from the time-resolved photoluminescence measurements, because detected scattered laser light and/or CBP fluorescence lead to a bi-exponential decay of the extracted curves. Other effects that can cause a bi-exponential decrease of the photoluminescence, such as TTA, can be excluded, due to the independent short lifetime of the decay over all optical spacer thicknesses [103]. If the bi-exponential decay would be caused by TTA, the short-living decay time should be, for rough estimations, half the long-living excited states lifetime [11], and therewith should be changed with the emitter/mirror distance. The long-living component of the bi-exponential fits has been used for the efficiency analysis presented in the previous section. This excited states lifetime is comparable to other publications [105–108]. Figure

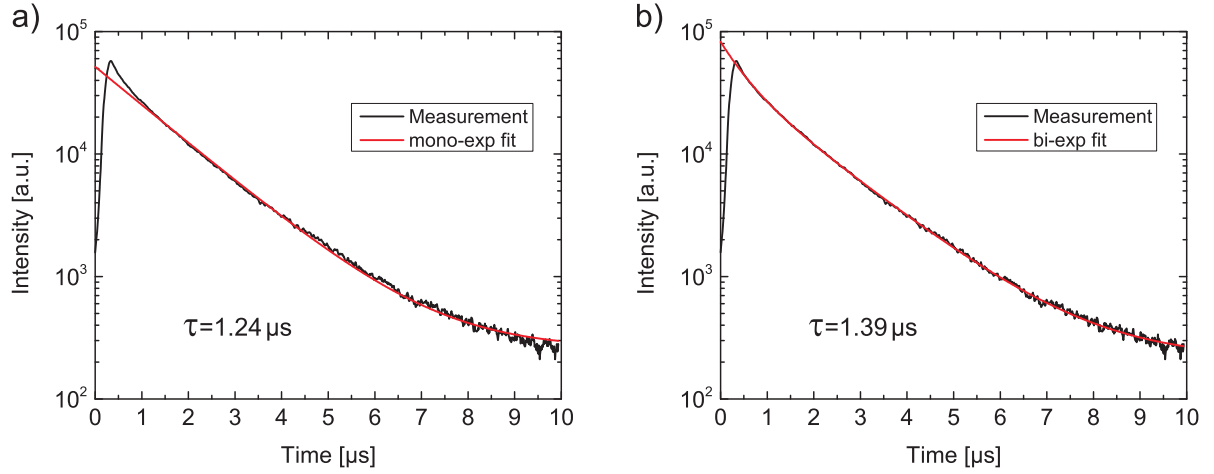


Figure 5.9: Exemplary photoluminescence decay curves for a LiF thickness of 305 nm with a) a mono- and b) a bi-exponential fit function yielding different excited states lifetimes. For the sake of simplicity, the short-living lifetime of the bi-exponential fit is not shown.

5.9 illustrates the comparison of a mono- and a bi-exponential fit for the same measured photoluminescence decay curve for an optical spacer thickness of 305 nm, resulting in excited states lifetimes $\tau_{\text{mono}} = 1.24 \mu\text{s}$ and $\tau_{\text{bi, long}} = 1.39 \mu\text{s}$, respectively. Obviously the bi-exponential function describes the measured behavior much better than the mono-exponential one. With this measured data it is now possible to determine the radiative quantum efficiency of the emitting guest/host system via a comparison with the calculated behavior of the relative lifetime changes as a function of the LiF thickness and the RQE. Therefore, simulations for different radiative quantum efficiencies have been performed, setting a δ -shaped emission zone in the middle of the 10 nm thick emission layer and assuming an isotropic emitter orientation. Figure 5.10 demonstrates the comparison of the measured excited states lifetimes with the simulated curves. Actually, the measured data points do not match with one simulated curve perfectly, but it is possible to determine the RQE of the emitting species to $q = 0.85 \pm 0.05$ in an appropriate way. It should be noted, that the scattering of the simulated curves for high ETL thicknesses result from sharp waveguided modes combined with a too rough step width for the in-plane wavevector used for the calculations.

However, the determination of the radiative quantum efficiency via the excited states lifetime changes with this method is not fully satisfactory. Hence, a fitting process of the measured data points was established. Therefore, it is essential to describe the simulated Purcell factor data with a mathematic function. Due to the oscillating appearance in most simulated cases, a polynomial with an order higher than seven turns out to be the most practicable fitting function. Figure 5.11 a) illustrates the fit of the simulated

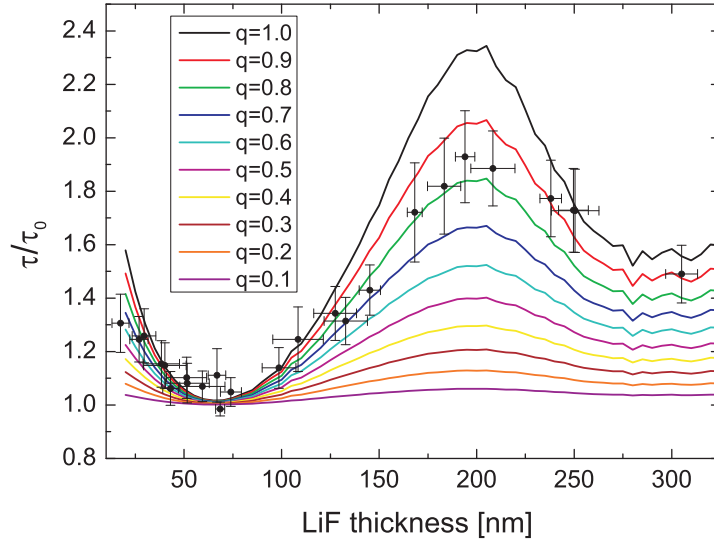


Figure 5.10: Determination of the radiative quantum efficiency of the emitting guest/host system Ir(ppy)₃:CBP. Dots represent measurements of the excited states lifetime normalized with the intrinsic value of 1.0 μ s (fitting variable). Solid lines illustrate the simulated behavior of the relative excited states lifetime changes as a function of the spacer thickness and of the RQE of the emitting system. Error bars result from the fitting procedure of the photoluminescence decay curves and from the profilometry measurements. The comparison of simulations and the measured data points yields a radiative quantum efficiency of 0.85 ± 0.05 .

Purcell factor for the samples under investigation with a polynomial function of 9th order showing a nearly perfect agreement. With this parametrization it is now possible to fit the measured excited states lifetime data with the following function:

$$\tau = \frac{\tau_0}{F(d_{\text{LiF}}) \cdot q + (1 - q)}. \quad (5.1)$$

Therein the Purcell factor $F(d_{\text{LiF}})$ is substituted by the determined polynomial function. The intrinsic excited states lifetime (τ_0) and the radiative quantum efficiency (q) remain as fitting parameters of the measured photoluminescence lifetimes as a function of the LiF thickness.

The results of this procedure are demonstrated in Fig. 5.11 b). It can clearly be seen, that the fit reproduces the measured data in an appropriate way, resulting in a radiative quantum efficiency of $q = 0.83 \pm 0.03$ and an intrinsic excited states lifetime of $\tau_0 = (1.00 \pm 0.01) \mu$ s. These values are in a very good agreement with the results from Fig. 5.10 and previous publications [108]. It should be noted that it is typically assumed that the Purcell factor oscillates about unity and the amplitude is decreasing with an increasing emitter/mirror distance. This is obviously not the case for these

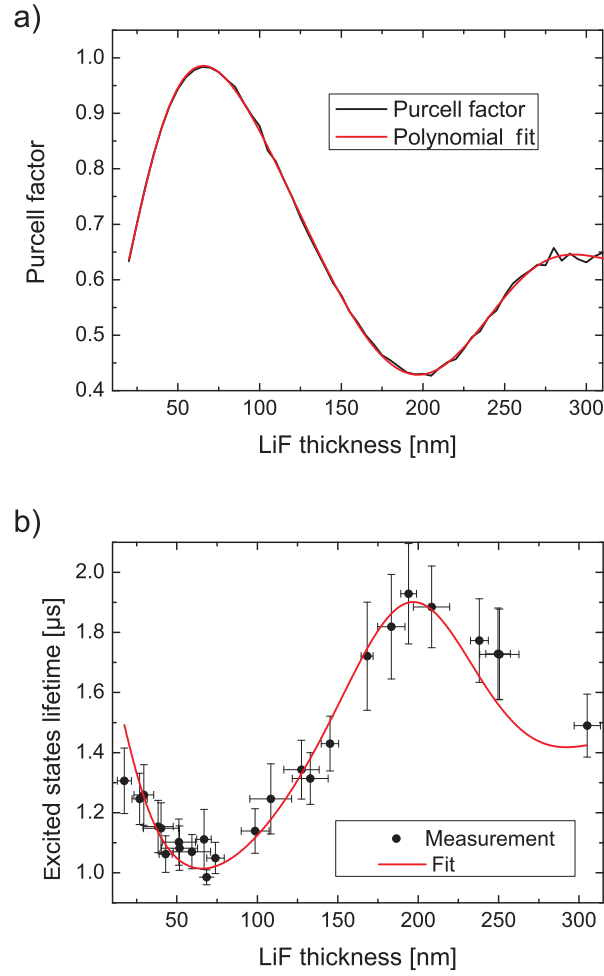


Figure 5.11: a) Polynomial fit (9th order) of the simulated Purcell factor. The nearly perfect result of this fit yields a functional description of the Purcell factor needed for an improvement of the determination of the radiative quantum efficiency of emitting systems via the excited states lifetime. b) Fit of measured excited states lifetimes for different LiF thicknesses using the results of a) with the RQE and the intrinsic excitonic lifetime as fitting parameters yielding an RQE of $q = 0.83 \pm 0.03$ and a $\tau_0 = (1.00 \pm 0.01) \mu\text{s}$.

simplified structures and can be explained by the huge refractive index mismatch at the organic/air interface resulting in destructive interference.

Therewith, an approach is demonstrated to determine the radiative quantum efficiencies of organic light-emitting guest/host systems with a simplified stack using two different optical spacers. Subsequently, a modification of this concept, which is based on a variation of the cavity strength at the position of the emitter, is needed to investigate the RQE of an emitting system inside complex OLED structures, as will be discussed in the following sections.

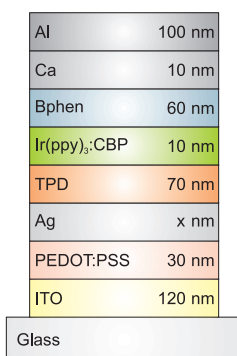


Figure 5.12: Schematic sketch of the used microcavity OLED stack under investigation. The thickness of the silver layer was varied in the range of 0–30 nm.

5.3 RQE determination via microcavity OLEDs

In the previous section, an approach to determine the radiative quantum efficiency of an organic light-emitting guest/host system via simplified structures was implemented using two different optical spacers that changed the distance of the emitting molecules to a highly reflecting mirror. Hence, the cavity strength at the emitter position was varied leading to a change of the excited states lifetimes. In order to implement this concept for complex OLED structures, a different manner to change the microcavity strength was established, that should allow to investigate the radiative quantum efficiency of the emitting system by electrically driven experiments, too. Therefore, a second metal layer was introduced to a typical OLED stack to enhance the electrical field at the position of the emitter inside the OLED. This approach was developed in cooperation with Thomas Wehlus in the scope of his PhD thesis [104].

The OLED stack under investigation is shown in Fig. 5.12. In principle, this stack is very similar with the standard stack presented in Fig. 3.1, which is only changed for the hole transporting side of the OLED. Therefore, the hole injection polymer PEDOT:PSS was used instead of HATCN, covered by a thin silver layer with a variable thickness, that should not affect the electrical performance of the OLED in a considerable way, but has a strong influence on the optical properties. This additional (to the metallic cathode) mirror enhances the cavity strength at the emitter position with increasing silver layer thickness, which allows for a determination of the RQE related to the method presented in the previous section. Finally, the silver layer was covered with 70 nm of N,N'-diphenyl-N,N'-bis(3-methylphenyl)-1,1'-biphenyl-4,4-diamine (TPD, chemical structure shown in Fig. 3.1) a hole transporting material to optimize the influence of the second mirror in terms of symmetry aspects. The emitting system under

investigation was, again, Ir(ppy)₃ doped with 10 wt% in a CBP matrix. The δ -shaped emission zone was set in the middle of the 10 nm thick emission layer and an isotropic emitter orientation was assumed for the simulation performed for different silver layer thicknesses.

Measuring the photoluminescence lifetimes for a variation of the silver layer thickness (0–30 nm) and comparing these results with simulations allows for a determination of the radiative quantum efficiency of the emitting guest/host system by transposing Eq. 2.23 resulting in

$$\frac{\tau_0}{\tau} = F(d_{\text{Ag}}) \cdot q + (1 - q). \quad (5.2)$$

The Purcell factor $F(d_{\text{Ag}})$ is simulated for the stacks exhibiting different silver thicknesses, resulting in the behavior of the relative lifetime changes presented in Fig. 5.13 a). Measuring the photoluminescence excited states lifetimes for every silver thickness using a nitrogen laser with a wavelength of 337.1 nm and multiplying the results with the calculated relative lifetimes allows for a determination of both, the intrinsic excitonic lifetime and the radiative quantum efficiency of the emitting system as it is illustrated in Fig. 5.13 b). The measured values of the excited states lifetime vary between 0.68 μs and 0.48 μs for the samples with a silver thickness of 0 nm and 30 nm, respectively, clearly demonstrating the huge influence of the microcavity on the excitonic lifetime. Because the intrinsic values of τ and q have to be identical, independently from the silver thickness of the sample, the intercept of the calculated curves from the simulations combined with the measurements represent the intrinsic τ_0 and the radiative quantum efficiency. This method yields values for $\tau_0 = 0.9 \pm 0.1 \mu\text{s}$ and $q = 0.75 \pm 0.07$, respectively. This is in very good agreement with the results of the previous section and with already published values [109].

These results should be verified by electrically driven EQE measurements to ensure a consistent determination of the RQE of the emitting system. However, due to an undesirable destabilization of the electrical characteristics of the fabricated microcavity OLEDs, it was not possible to perform external quantum efficiency measurements for a varying silver thickness. Additionally, the analysis of the excited states lifetime gets more and more complicated for an increase of the cavity strength due to strong intensity and angular dependence changes by the microcavity [110, 111], resulting in a lack of available data points. Hence, another approach for the determination of the radiative quantum efficiency of emitting systems embedded in complex OLED structures has to be found.

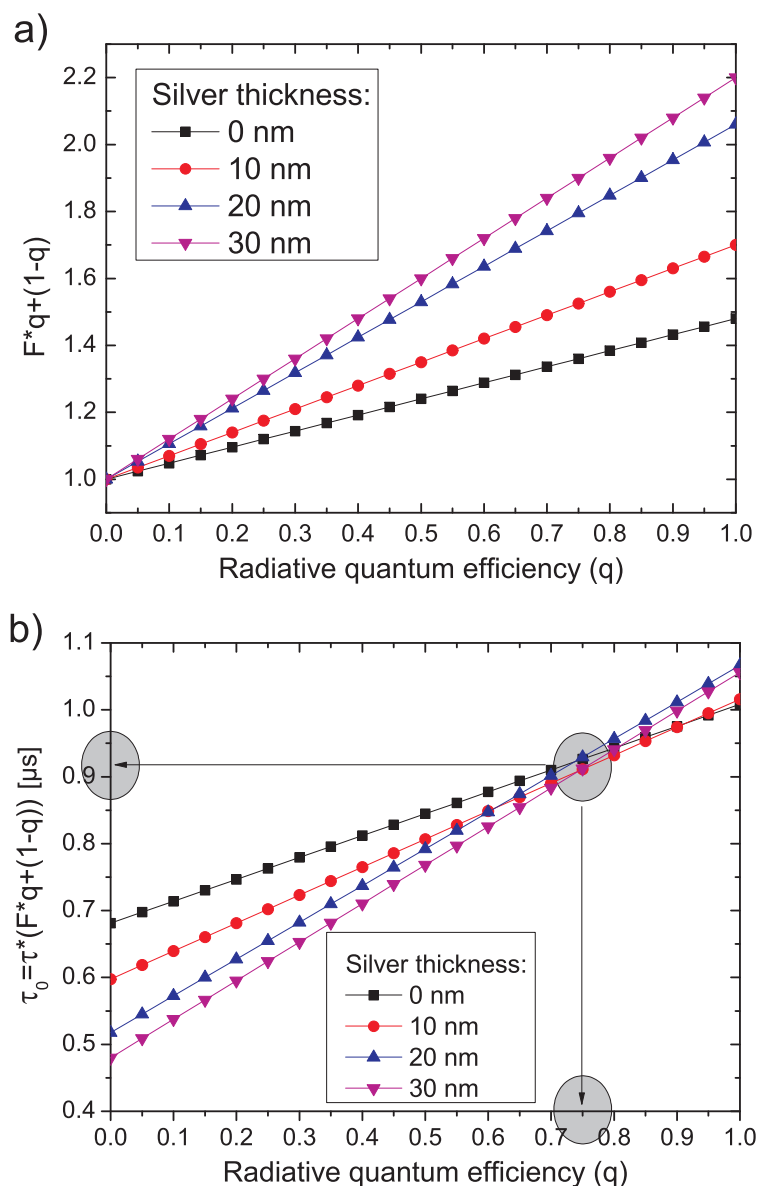


Figure 5.13: a) Calculated behavior of the relative lifetime changes for different silver thicknesses as a function of the radiative quantum efficiency. b) Using the simulations from a) and multiplying the curves with measured excited states lifetimes for the different silver thicknesses allows for a determination of the intrinsic excitonic lifetime and the radiative quantum efficiency of the emitting system under investigation resulting in $\tau_0 = 0.9 \pm 0.1 \mu\text{s}$ and $q = 0.75 \pm 0.07$, respectively. Sample structure: Glass/ITO/PEDOT:PSS/Ag/TPD/Ir(ppy)₃:CBP/Bphen/ca/Al.

5.4 Efficiency analysis of state-of-the-art phosphorescent OLEDs

The former sections have analyzed and presented methods for a radiative quantum efficiency determination in simplified structures and in microcavity OLEDs. Unfortunately, it was not possible to integrate external quantum efficiency measurements in the investigation of the RQE of emitting systems, due to the electrical instability of the microcavity devices. However, measuring the EQE of complete OLED stacks as a function of the cavity strength at the emitters position in addition to the excited states lifetime analysis would yield more precise results and facilitate advanced investigations.

Hence, another method to vary the cavity strength at the emitter position inside the OLED, but which is not modifying the electrical properties, is prospected. Changing the cavity length of the OLED in terms of a subsequent variation of the electron transport layer thickness results in an appropriate modification of the cavity strength at the emitter position. Figure 3.3 shows some of the investigated state-of-the-art OLED structures with a variation of their ETL thickness. To ensure that the electron transport layer thickness does not influence the electrical characteristics, but the optical resonator of the fabricated OLEDs, the resistivity of (both) transport layers was decoupled from their thickness by means of well established chemical conductivity doping [15, 112, 113]. Therewith, it is possible to analyze the radiative quantum efficiency of the organic light-emitting guest/host system embedded in a complete OLED stack with electrically driven EQE and time-resolved photoluminescence measurements. Please note, that all samples which are presented in section 5.4 have been provided by OSRAM OS. Figure 5.14 a) shows a state-of-the-art OLED stack under investigation using the green phosphorescent emitter $\text{Ir}(\text{ppy})_3$, such as in the previous sections. Unfortunately, the chemical structures of the matrix and the other organic materials can not be disclosed. However, due to the knowledge of the refractive indices and the absorption coefficients, it is possible to perform optical simulations resulting in power dissipation spectra and the Purcell factors for the varying ETL thickness. The results of these calculations for an isotropic emitter orientation are shown in Fig. 5.14 b)–d). The behavior of the relative changes of the excited states lifetimes is very similar to the already presented oscillations in section 5.2. Figure 5.14 b) illustrates the calculated excited states lifetimes for the OLED stack shown in Fig. 5.14 a) as a function of the ETL thickness and for different radiative quantum efficiencies of the emitting system.

Additionally, the behavior of the external quantum efficiency for both, the direct emission and the substrate modes, if macroscopic outcoupling structures are index matched

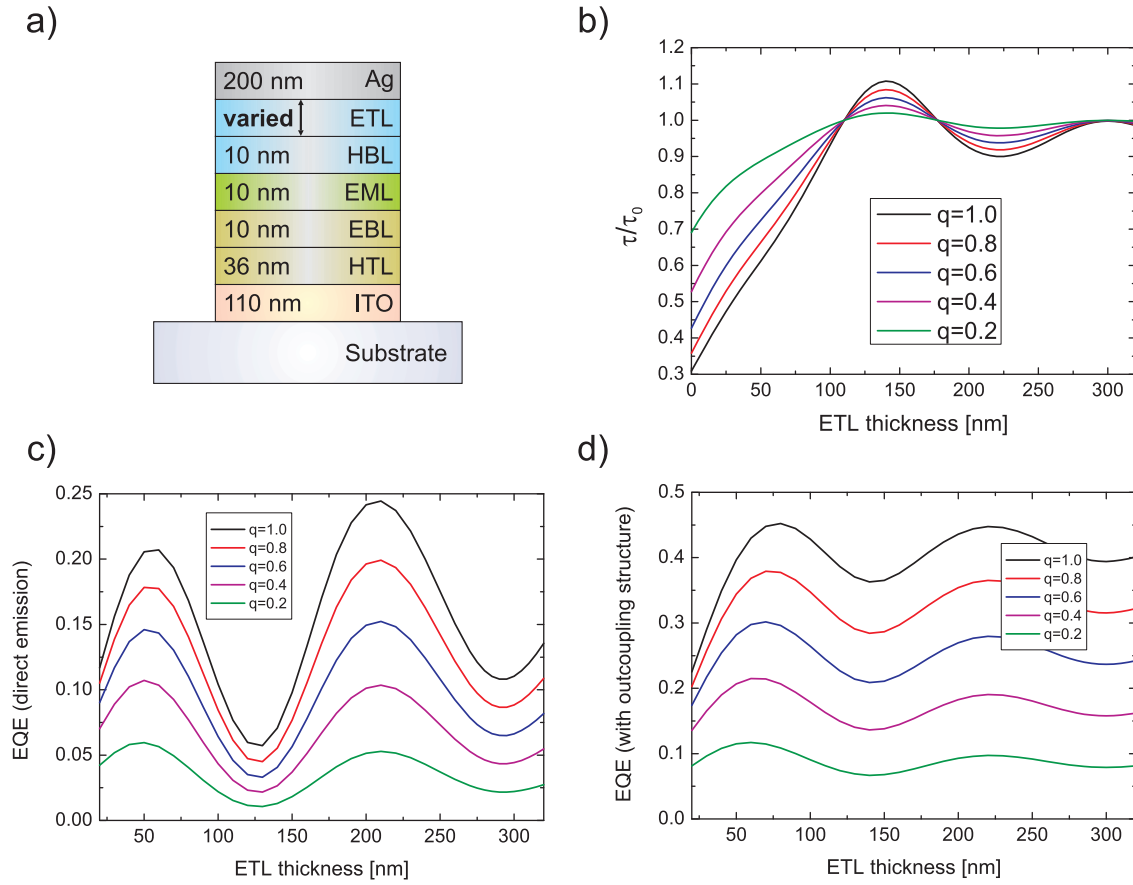


Figure 5.14: a) Schematic sketch of the state-of-the-art OLED stack under investigation. Ir(ppy)₃ is acting as the emitting species and the distance of the mainly electron transporting emission layer to the metallic cathode is varied by the ETL thickness. b) Calculated relative excited states lifetime changes as a function of the ETL thickness for different RQE values. c) Simulations of the external quantum efficiency as a function of the ETL thickness and for different RQE values for direct emission, and d) if a macroscopic outcoupling enhancement is used.

to the glass substrate, can be extracted from these simulations and are shown in Fig. 5.14 c) and d), respectively. The simulations of the external quantum efficiencies have been performed for an ideal charge carrier balance (γ) and a radiative exciton fraction (η_r) of unity. Hence, the calculations exclusively show the dependence of the EQE on the outcoupling factor and the effective radiative quantum efficiency of the emitting system as a function of the ETL thickness. Moreover, the simulations for an intrinsic RQE of unity directly represent the outcoupling factor of the devices.

As a first result, it is obvious from Fig. 5.14 c) that the second maximum of the EQE is the favorable one, if only direct emission is of interest and if the RQE of the used

emitting system is higher than about 0.5. Otherwise, the first maximum would yield higher EQE values. This is in good agreement with previously reported results from other groups using different OLED stacks [42, 52, 114], and is a direct consequence of the changes of the effective radiative quantum efficiency of the emitting system, because the outcoupling factor is not influenced by this factor.

Indeed, if macroscopic outcoupling structures, such as glass hemispheres index matched on the substrate, are used and the main part of the substrate modes can be extracted by this method, the first maximum always yields the highest values and the position is only slightly changed to smaller emitter/cathode distances for a decrease of the RQE of the emitting guest/host system. However, it is very important to know the RQE of the emitting system if the OLED should be optimized in terms of efficiency enhancement via layer thickness adjustment. Additionally, the influence of the matrix material and quenching effects that are reducing the RQE especially at high current densities should be considered, and the cavity length has to be chosen appropriately for the planned operation current density, as will be discussed later in detail.

5.4.1 Influence of the matrix material

Typically, the charge carriers in an organic light-emitting diode are initially residing on the matrix material, as polarons or already forming an exciton, and are accordingly transferred to the light-emitting guest molecules. This energy transfer process can strongly influence the radiative quantum efficiency of the emitting species. Hence, the RQE is always specified for the emitting guest/host system and not only for the emitting molecules. Thus, the influence of the matrix material on the RQE of the emitting molecule Ir(ppy)₃ will be analyzed and quantified in this section.

As already presented in this thesis, the RQE of the emitting system Ir(ppy)₃:CBP was determined to $q = 0.83 \pm 0.03$ and $q = 0.75 \pm 0.07$ in a simplified stack and in a microcavity OLED, respectively. The discrepancy of the result of these two methods could be caused by the different doping concentration of the emitting molecules and therewith concentration induced quenching effects. However, the RQEs of emitting systems used in state-of-the-art OLEDs are of interest. Nevertheless, the previous results are the basis of the following investigations.

In modern OLEDs, the standard CBP matrix for the often used emitter Ir(ppy)₃ is replaced by other materials, that achieve a significant increase in long-term stability of the devices. Therefore, the RQE of Ir(ppy)₃ is analyzed for two different matrices (chemical structure unknown). First, the stack already shown in Fig. 5.14 a) exhibiting a mainly electron transporting matrix material was investigated. With the previously illustrated

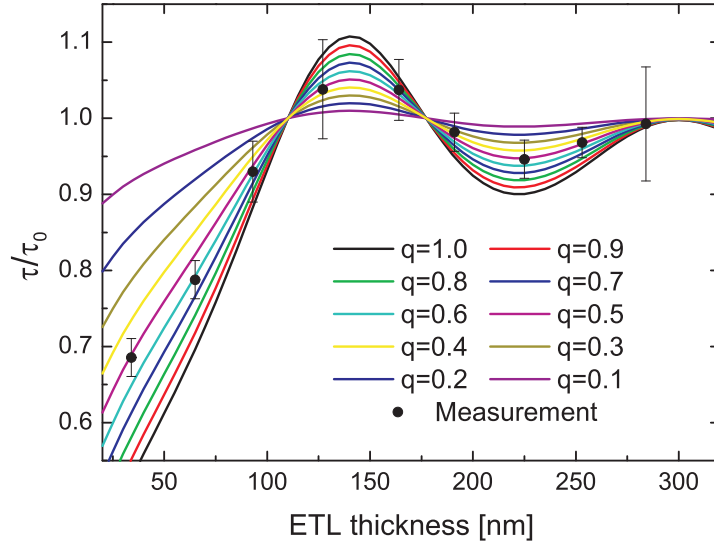


Figure 5.15: Comparison of the relative excited states lifetime changes (dots) with optical simulations for a variation of the RQE as a function of the ETL thickness (solid lines), resulting in $q = 0.50 \pm 0.075$. All measured excited states lifetimes have been normalized with the intrinsic value of $0.69 \mu\text{s}$. Graphic was taken from Ref. [26]. Sample structure: Glass/ITO/HTL/EBL/EML ($\text{Ir}(\text{ppy})_3$, electron transporting matrix)/HBL/ETL/Ag.

simulations it is possible to determine the RQE of this emitting system via excited states lifetime measurements and electrically driven EQE measurements of nine devices exhibiting different ETL thicknesses. All layer thicknesses have been provided by OSRAM OS by a method, based of a comparison of optical simulations and measurements of the 0° -spectra.

The results of the excited states lifetime measurements (excitation via nitrogen laser, 337.1 nm) are illustrated in Fig. 5.15. The measured data points show the expected oscillation as a consequence of the modified radiative rate by the Purcell effect. It should be noted that the huge error bars, especially in the cavity minimum (e.g. at an ETL thickness of 125 nm) result from low photoluminescence intensities and an overlap of the emission spectrum of the $\text{Ir}(\text{ppy})_3$ molecules with that of the blocking layers. All measured excited state lifetimes have been normalized with an intrinsic value of $0.69 \mu\text{s}$ (fitting parameter). This result is slightly shorter than the values determined for the $\text{Ir}(\text{ppy})_3$ molecules embedded in a CBP matrix, due to an increase of the non-radiative rate induced by the matrix material, resulting in a reduced RQE for this emitting system of $(50 \pm 7.5) \%$. This value is remarkably reduced by a factor of 1.6 compared to the RQE of the emitting system using CBP as matrix molecules.

The situation changes, if the analysis of the electrically driven external quantum effi-

ciency measurements is considered, too. The optical simulations and the measured data points for a low current density of $j = 1 \text{ mA/cm}^2$ are illustrated in Fig. 5.16 a) and b), for the direct emission and if a macroscopic glass hemisphere index matched to the glass substrate, acting as outcoupling enhancement, is used, respectively.

The measurements show an oscillation as a function of the ETL thickness as a result of the Purcell effect affecting both, the effective radiative quantum efficiency of the emitting system and the outcoupling factor of the device. The charge carrier balance was set to unity, due to the use of appropriate blocking and conductivity doped transport layers. However, the comparison of the simulated behavior and the measured EQE values results in an RQE of $q = 0.40 \pm 0.05$, although a low current density was used, and therefore current induced quenching processes such as TPQ can be excluded. Hence, another effect must be responsible for the differences of the RQE determined by photoluminescence and electroluminescence measurements. One possible explanation are changes in the profile of the emission zone for the different excitation methods. While almost the complete emission layer is excited by the laser pulse with a nearly constant exciton density because of its low thickness of only 10 nm, the emission zone is very narrow and located close to the EBL/EML interface, due to the much better electron conductivity of the used matrix material [116]. This results in high exciton densities even for low current densities. Hence, exciton density induced quenching [49] and non-radiative processes near the EBL/EML-interface [117] could lower the RQE of the emitting system, resulting in the determined lower values as for the excited states lifetime interpretation. To emphasize the influence of the matrix material on the RQE of an emitting system, another OLED stack exhibiting Ir(ppy)_3 as emitting molecule embedded in a third matrix (chemical structure unknown) was investigated.

The stack layout is shown as a schematic sketch in Fig. 5.17 a). In principle, this stack is very similar to the OLED stack shown in Fig. 5.14 a) and exhibits only slightly different layer thicknesses. The most important difference is the implementation of a thicker emission layer consisting of a dual matrix. Hence, the EML consists of 10 nm of a mainly hole transporting followed by 10 nm of a mainly electron transporting matrix material in order to place the emission zone in the middle of the EML. However, this allows for an identical determination of the RQE of the emitting system as presented for the previous state-of-the-art OLED. Again, nine devices with a systematic variation of the ETL thickness have been fabricated and simulations of the power dissipation have been performed assuming a δ -shaped emission zone in the middle of the emission layer and an isotropic emitter orientation. The results of the excited states lifetime measurements and the comparison with the simulated behavior for different RQE values as a

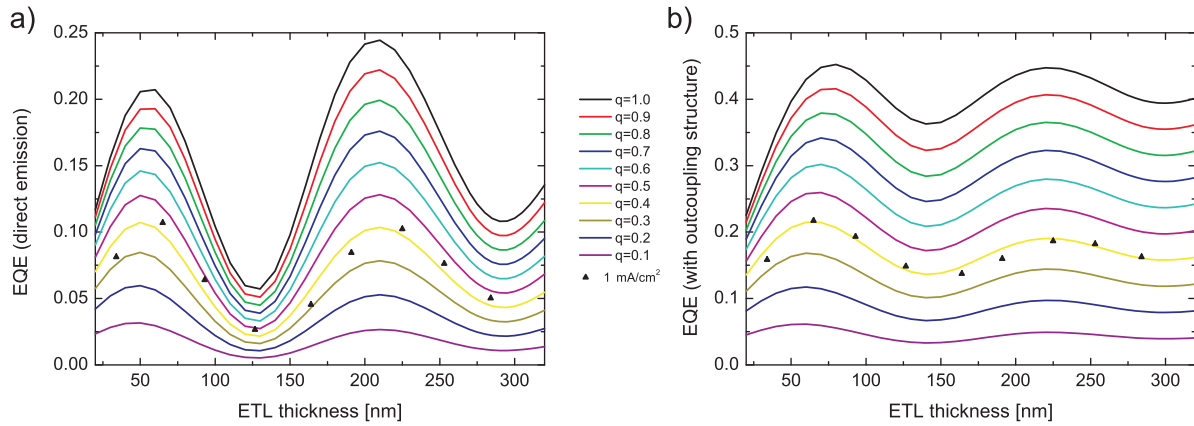


Figure 5.16: Simulations and measurements ($j = 1 \text{ mA/cm}^2$) of the external quantum efficiency for a) direct emission and b) if a macroscopic outcoupling enhancement is used, as a function of the ETL thickness. Triangles represent measurements of the devices exhibiting nine different ETL thicknesses, while solid lines are illustrating the simulated behavior for different RQE values. A comparison of simulations and measurements yields an RQE of $q = 0.40 \pm 0.05$. Graphic was taken from Ref. [26,61]. Sample structure: Glass/ITO/HTL/EBL/EML (Ir(ppy)_3 , electron transporting matrix)/HBL/ETL/Ag.

function of the emitter/cathode distance is illustrated in Fig. 5.17 b). It can clearly be seen, that the simulated curves do not describe the measured data in an excellent way, nevertheless the RQE of the emitting system can be estimated to $q = (60 \pm 10) \%$. The large error bars and the spreading of the measured excited states lifetimes originate from low photoluminescence signals resulting in ambiguous fits with considerable uncertainties. Additionally, the strong deviation of the measured excited states lifetimes and the simulation for the devices with an ETL thickness smaller than 50 nm could result from not taking into account a distinction between near-field coupling to surface plasmons and non-radiative energy transfer to lossy surface waves, that appears especially for very short emitter/cathode distances [22,23,118]. Another explanation could be the strong superposition of the emission from the EML and other layers, that would influence the analysis most for short excited states lifetimes of the emitting molecules, in particular for small ETL thicknesses.

In contrast, the determination of the radiative quantum efficiency of the emitting system via electrically driven external quantum efficiency measurements yields much better results compared to the values extracted from the changes of the excited states lifetime measurements. Figure 5.18 a) and b) demonstrate the simulated and measured EQE ($j = 1 \text{ mA/cm}^2$) behavior as a function of the ETL thickness for the direct emission and if the substrate modes of the devices are extracted, respectively. In contrast to the

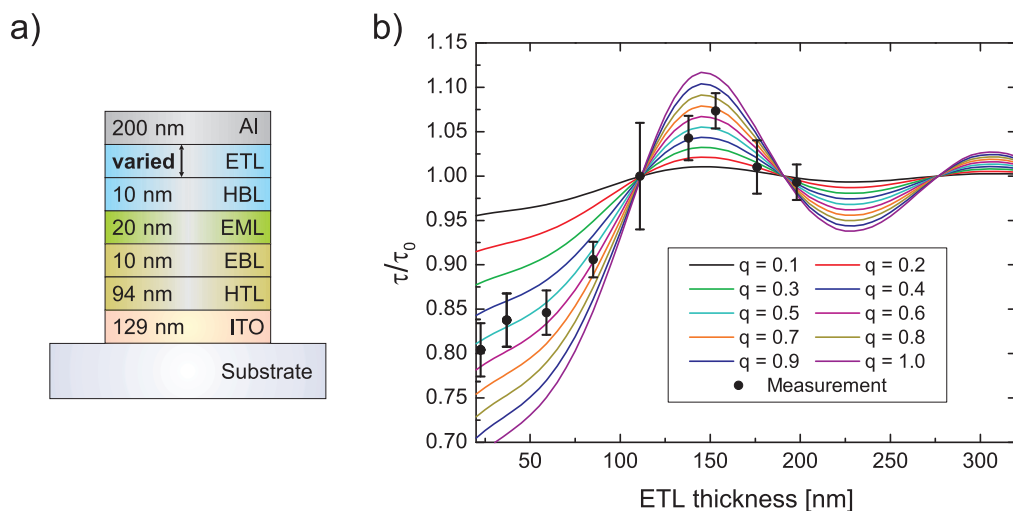


Figure 5.17: a) Stack layout of the state-of-the-art OLED exhibiting a third matrix for the emitting molecule Ir(ppy)₃. The ETL thickness was varied. b) Comparison of the relative excited states lifetime changes (dots) with optical simulations for a variation of the RQE as a function of the ETL thickness (solid lines), resulting in $q = 0.6 \pm 0.1$. All measured excited states lifetimes have been normalized with the intrinsic value of $0.60 \mu\text{s}$ (fitting parameter). Sample structure: Glass/ITO/HTL/EBL/EML (Ir(ppy)₃, dual matrix)/HBL/ETL/Ag.

time-resolved photoluminescence measurements, the simulated behavior of the external quantum efficiency describes the measured data points in a reasonable way, resulting in an RQE of $q = (60 \pm 5) \%$. Especially the simulations with outcoupling enhancement are in perfect agreement with the measured electrically driven external quantum efficiencies. Despite the problems for the analysis of the RQE via time-resolved photoluminescence measurements, both methods obtain almost the same values for the radiative quantum efficiency. Furthermore, these results give evidence that the broader emission layer reduces the current induced quenching processes, because both determined RQE values are much closer together than in the previous analysis.

In conclusion, the influence of the matrix material on the radiative quantum efficiency of emitting systems exhibiting Ir(ppy)₃ as emitting molecule has been investigated. The determined RQE values are between 40 % and 83 %. This clearly demonstrates the significance of choosing appropriate matrix materials in terms of both, long-term stability and efficiency optimization. Furthermore, it was therewith pointed out, that RQE investigations of emitters via photoluminescence measurements in integrating spheres are too far away from the final device and are hence not the method of choice for efficiency analysis in complex state-of-the-art OLED structures.

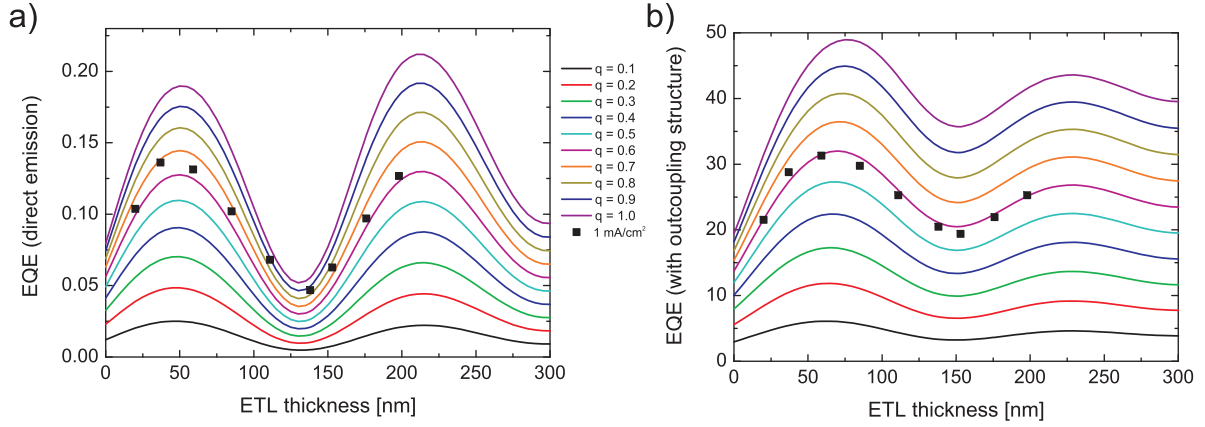


Figure 5.18: Simulations and measurements ($j = 1 \text{ mA/cm}^2$) of the external quantum efficiency for a) direct emission and b) if a macroscopic outcoupling enhancement is used, as a function of the ETL thickness. Dots represent measurements of the devices exhibiting nine different ETL thicknesses, while solid lines are illustrating the simulated behavior for different RQE values. A comparison of simulations and measurements yields an RQE of $q = 0.60 \pm 0.05$. Sample structure: Glass/ITO/HTL/EBL/EML (Ir(ppy)_3 , dual matrix)/HBL/ETL/Ag.

5.4.2 Influence of the current density

The previous section has investigated the influence of different matrix materials on the radiative quantum efficiency of the emitting systems exhibiting Ir(ppy)_3 as emitting molecules. This section will analyze the current induced changes of the RQE.

Therefore, the determination of the RQE of the emitting system of the devices presented in Fig. 5.14 a) using the mainly electron transporting matrix material was performed for different current densities. Unfortunately, the investigation of the underlying quenching process in terms of a combination of photo- and electroluminescence time-resolved measurements as mentioned in sec. 4.3.2 was not possible with these devices due to the overlap of the emission spectra of the Ir(ppy)_3 molecules and the blocking materials, that complicates the determination of the excited states lifetime particularly if the excitonic lifetime is reduced due to additional quenching processes. However, the investigation via the electrically driven external quantum efficiency was possible by applying different constant currents during the integrating sphere measurements.

Figure 5.19 illustrates the results of the external quantum efficiency measurements at different current densities. The comparison with the simulations for a variation of the RQE of the emitting system and as a function of the ETL thickness demonstrates the strong influence of the current density. The determined RQE values are drastically reduced with increasing current flow through the devices. While the RQE for a very

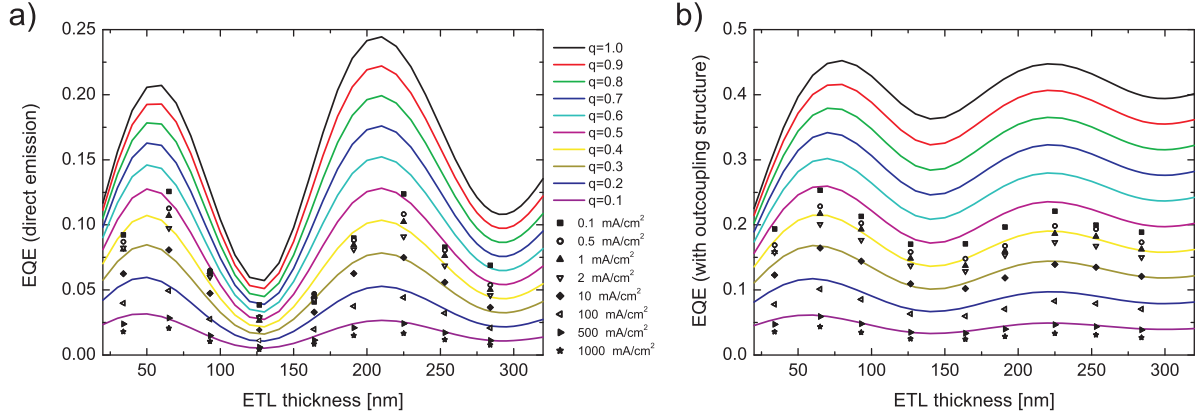


Figure 5.19: Investigation of the influence of the current density on the radiative quantum efficiency of the emitting system of the devices already presented in Fig. 5.14 for a) the direct emission and b) if macroscopic outcoupling structures are used. Points are representing measurements for different current densities, while solid lines stand for simulations for different RQEs as a function of the ETL thickness. The RQE is drastically reduced by an increasing current density in both cases. Graphics taken from Ref. [26]. Sample structure: Glass/ITO/HTL/EBL/EML (Ir(ppy)₃, electron transporting matrix)/HBL/ETL/Ag.

low current density of $j = 0.1 \text{ mA/cm}^2$ yields nearly the value extracted from the time-resolved photoluminescence measurements ($q = 0.50 \pm 0.075$), the RQE is only half of that value for a current density of $j = 10 \text{ mA/cm}^2$. This is an evidence, that strong current induced quenching effects are present in the devices under investigation. Due to a nearly perfect match of the simulations with the measurements up to high current densities, a reduction of the assumed perfect charge carrier balance can be excluded. If γ would be the reason for the decrease in the EQE, the measured data points would not fit the simulations that well, while a variation of the RQE of the emitting system results in changes in the relative heights of first and second cavity maximum and is therefore more characteristic.

In order to point out the influence of the current density on the RQE of an emitting system, Fig. 5.20 shows the results extracted from Fig. 5.19. It is obvious, that the radiative quantum efficiency is drastically reduced for increasing current density. This is in very good agreement with results previously published by other groups [47–49]. However, as mentioned before, this behavior has to be considered for device optimization in terms of layer thickness adjustment, because the favorable cavity length can vary for very low current densities and the planned operation conditions. It can clearly be seen from Fig. 5.20, that the RQE of the emitting system extracted from time-resolved photoluminescence experiments is still not reached even for very small current densities,

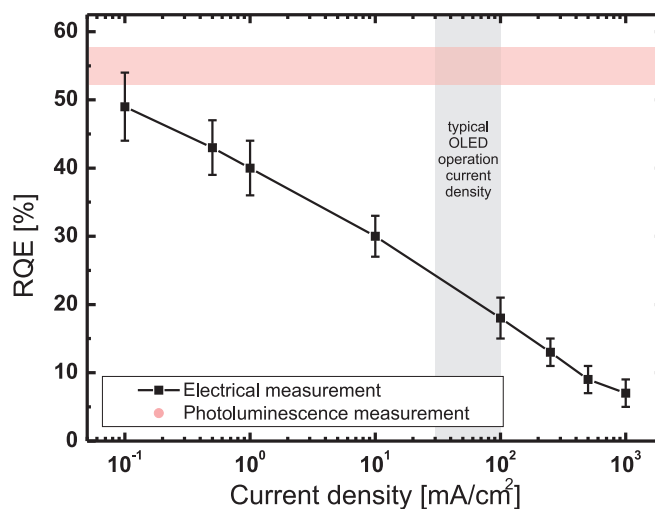


Figure 5.20: Current density dependence of the RQE of the emitting system exhibiting Ir(ppy)₃ as emitting molecules. The range of the typical operation current density of state-of-the-art OLEDs is marked with a gray area. The RQE of the emitting system extracted from time-resolved photoluminescence spectroscopy, which corresponds to the extrapolation of the curve for $j = 0 \text{ mA/cm}^2$, is marked as a pink area. Graphic taken from Ref. [64]. Sample structure: Glass/ITO/HTL/EBL/EML (Ir(ppy)₃, electron transporting matrix)/HBL/ETL/Ag.

and therewith the q_{PL} corresponds to the extrapolation for $j = 0 \text{ mA/cm}^2$. Moreover, the RQE is decreased with the current density and remains at about only 20 % at the typical operation current for state-of-the-art OLEDs. This is a remarkable decrease of 65 % of the intrinsic value.

5.4.3 Influence of non-isotropic emitter orientation

The previous sections have demonstrated the principles of determining the radiative quantum efficiency of emitting guest/host systems in both, simplified structures and in complex state-of-the-art multi-layered OLEDs. Until now, all measurements have been consistently explained by simulations assuming an isotropic orientation of the emissive dipole moments of the emitting molecules. This common assumption is based on the suggestion of an isotropic orientation, in particular in amorphous matrices, of most phosphorescent molecules based on iridium, i.e. Ir(ppy)₃, due to their spheric appearance calculated by density functional theory simulations [119]. Although emitter orientation is a well-known feature in OLEDs based on polymeric materials [54, 55], it was not taken into account for a long time in devices using emitting systems based on a compound of small molecules. However, recent studies have given clear evidence

for the existence of both, fluorescent [56, 57, 120] and phosphorescent [58, 121] small molecules with a prevailing orientation of their emissive dipole moments, even doped with only a few wt% in amorphous matrices. This section will investigate the principle influence of non-isotropic emitter orientation on the energy distribution between the different optical modes, and therewith the implication for the determination of the radiative quantum efficiency of emitting systems. Furthermore, the implication for a consistent efficiency analysis in state-of-the-art OLEDs will be pointed out. In order to emphasize the importance of taking account for possible deviations of randomness for emitting guest/host systems based on phosphorescent small molecules, an exemplary efficiency analysis for the common red phosphorescent emitter Iridium(III)bis(2-methyldibenzo-[f,h]quinoxaline)(acetylacetonate) ($\text{Ir}(\text{MDQ})_2(\text{acac})$) doped with 8 wt% in an α -NPD matrix, showing a prevailing horizontal orientation of the emissive dipole moments, will be given. Most of the presented results in this section are based on the publications [53, 59, 65]. First, the differences in the behavior of the Purcell factor, in the interference conditions and in the coupling to the optical modes will be pointed out by means of optical simulations. Additionally, the possible efficiency enhancement by using completely horizontally oriented emitting dipoles will be figured out. Second, the influence of non-isotropic emitter orientation on the determination of the radiative quantum efficiency will be emphasized. Finally, a comprehensive efficiency analysis of the state-of-the-art OLED stack under investigation will be presented, including orientation effects and current density induced quenching processes.

Figure 5.21 shows the state-of-the-art OLED stack under investigation in this section, the chemical structures of the molecules forming the emitting system and the intrinsic emitter spectrum used for all simulations presented in this section. The δ -shaped emission zone was set in the middle of the emission layer. Nine devices with different ETL thicknesses were investigated. All photoluminescence lifetime measurements have been performed using the nitrogen laser system with an excitation wavelength of 337.1 nm and the streak camera system, while the external quantum efficiency was determined by integrating sphere measurements. $\text{Ir}(\text{MDQ})_2(\text{acac})$ shows a prevailing horizontal emitter orientation if it is doped with 8 wt% in an α -NPD matrix, and the anisotropy factor was determined to $\theta = 0.65/2.65 = 0.25$ [58, 59].

Figure 5.22 demonstrates the different behavior of the relative excited states lifetime as a function of the ETL thickness for a variation of the emitter orientation. The plotted lines represent simulations of the reciprocal values of the Purcell factor, while dots stand for experimental data from time-resolved photoluminescence measurements normalized by an intrinsic excited states lifetime of 1.37 μs . It can clearly be seen, that the maxima

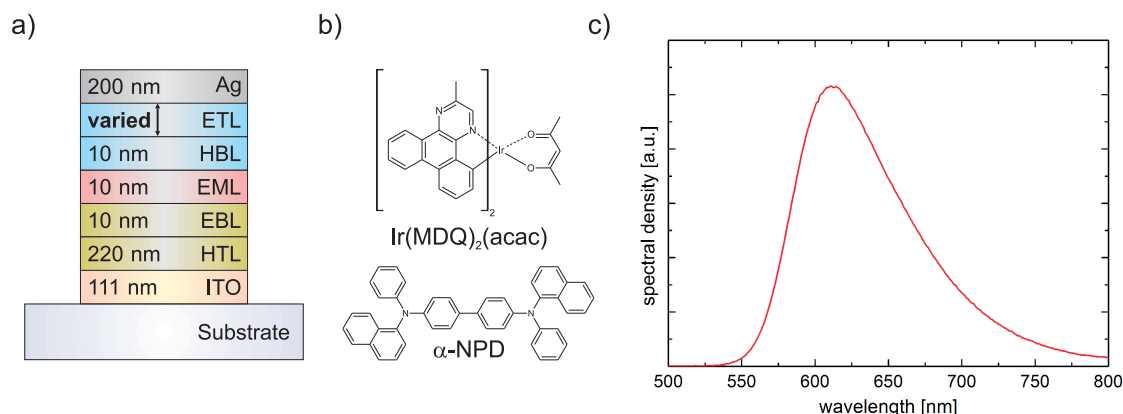


Figure 5.21: a) Structure of the red phosphorescent bottom emitting OLED stack under investigation and b) the chemical structure of the host- (α -NPD) and the guest- ($\text{Ir}(\text{MDQ})_2(\text{acac})$) molecule. The ETL layer thickness of the stack was varied between 20 and 400 nm. c) Intrinsic red emitter spectrum with a peak wavelength at 610 nm used for all optical simulations presented in this section. Graphics taken from Ref. [53].

of the lifetime are at (completely) different ETL thicknesses for the two extreme cases of horizontally and vertically oriented emitting dipoles. This is caused by the individual coupling to the optical modes and the different interference conditions for the different emitter orientations. While the differences between horizontal and isotropic emissive dipole orientation is only obvious in the strength of the variations but not in the position of maxima and minima for ETL thicknesses larger than 75 nm, they deviate strongly for low emitter/cathode distances. Furthermore, the characteristics for vertical emitter orientation differs strongly from the other two cases. While vertically oriented emitters show a maximum in the relative excited states lifetimes, horizontal and isotropic emitters exhibit a minimum, and vice versa (at slightly different ETL thicknesses). In particular, the strong deviations of the simulated behavior, especially if the emitting molecules are located close to the metallic cathode (below 55 nm), allows for measurements in this region that are very sensitive for non-isotropic emitter orientation [53, 59, 65, 122] due to the different coupling to surface plasmon polaritons resulting in a strong reduction of the excited states lifetime for vertically oriented emissive dipoles. However, the measured excited states lifetimes for the OLED stack under investigation do not fit to one of the simulations of the extreme cases of emitter orientation and the assumption of a perfect radiative quantum efficiency. Hence, the simulations have to be adjusted for the present emitter orientation and RQE of the emitting system, as will be presented later in this section.

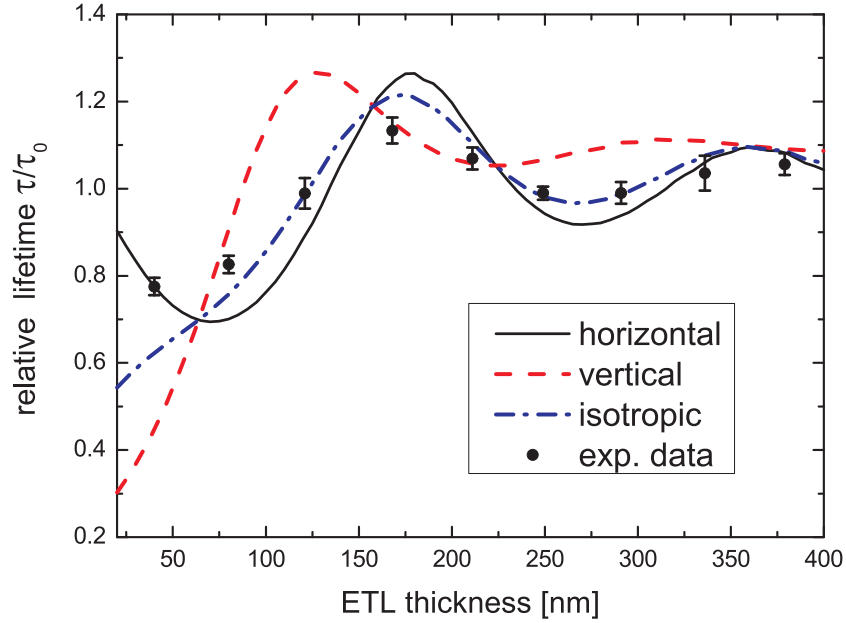


Figure 5.22: Relative lifetime changes for the stack under investigation. Solid lines: Simulations of the relative excited states lifetime changes as a function of the ETL thicknesses for horizontal, vertical and isotropic emitter orientation. The intrinsic radiative quantum efficiency of the emitting system was set to unity, for the sake of simplicity. Dots: Experimental data from time-resolved measurements. Graphic taken from Ref. [65]. Sample structure: Glass/ITO/HTL/EBL/EML ($\text{Ir}(\text{MDQ})_2(\text{acac})\text{:}\alpha\text{-NPD}$)/HBL/ETL/Ag.

In order to emphasize the individual performance of different emitter orientations, simulations of the direct emission of the OLED stack presented in Fig. 5.21 have been performed for the three extreme cases assuming a perfect radiative quantum efficiency ($q=1$). Figure 5.23 demonstrates the results of these simulations. In accordance to Fig. 5.22, the deviations of the different emitter orientations show the same characteristics. Again, vertically oriented emitters show maxima in the direct emission at ETL thicknesses, where horizontally oriented ones exhibit minima, and vice versa. It should be noted, that due to the assumption of an RQE of unity, these simulations represent directly the outcoupling factors for direct emission, that are mainly caused by the different interference conditions for the individual emitter orientations. As can be seen from Fig. 5.23, polarization and angular dependent electroluminescence measurements in the cavity minimum for isotropic and horizontal emitter orientation at an ETL thickness of about 160 nm allow for a determination of the ratio between vertically and horizontally oriented emissive dipole moments and therewith of the prevailing emitter orientation [55, 58]. This is one of the two methods that have been used to determine

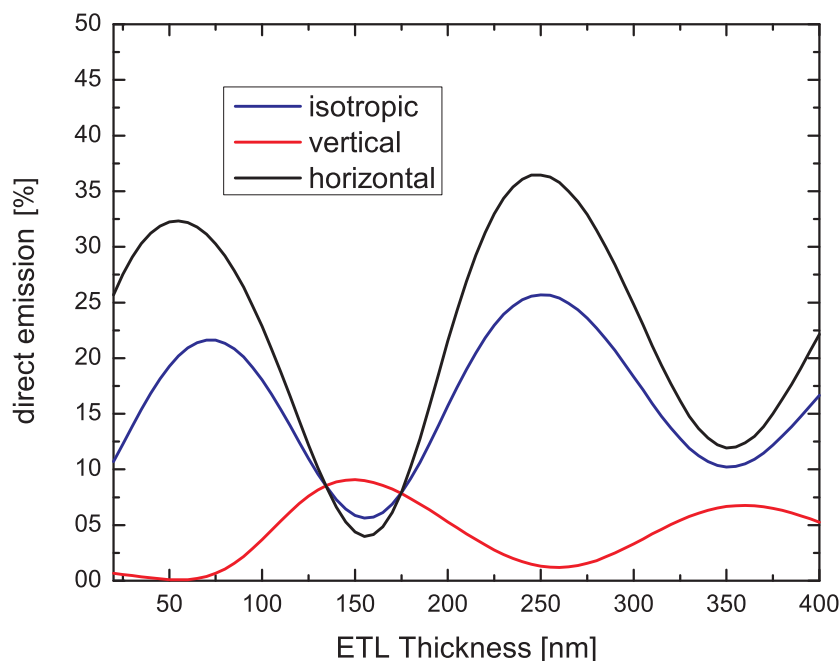


Figure 5.23: Simulations of the direct emission of the OLED stack under investigation performed for the three extreme cases of emitter orientation as a function of the ETL thickness. The RQE was set to unity. Graphic taken from Ref. [53]. Sample structure: Glass/ITO/HTL/EBL/EML ($\text{Ir}(\text{MDQ})_2(\text{acac}):\alpha\text{-NPD}$)/HBL/ETL/Ag.

the emitter orientation of the used emitting system. The other method is based on a polarization and angular dependent photoluminescence measurement of the OLED stack fabricated without a cathode to prevent energy coupling to surface plasmon polaritons, especially for the vertically oriented emissive dipole moments [56, 58].

Moreover, in order to elaborate the different energy coupling to the optical modes present in an OLED, Fig. 5.24 illustrates simulations of all energetic channels of the OLED stack under investigation for a radiative quantum efficiency of unity and the three extreme cases of emitter orientation of the used emitting system as a function of the ETL thickness. It can clearly be seen, that the characteristics of the vertically oriented emissive dipoles is completely different in comparison to the other two cases. Especially at low emitter/cathode distances, vertically oriented emitters are coupling almost their whole energy to surface plasmon polaritons and even in the cavity maximum for direct emission only very low external quantum efficiencies can be achieved. However, if substrate modes are extracted by an outcoupling enhancement, noteworthy 55 % EQE can be reached. Nevertheless, vertically oriented emitters are not favorable at all, due to the strong angular dependent emission spectrum, in particular for the outcoupled substrate modes. Hence, horizontally oriented emitting dipoles should

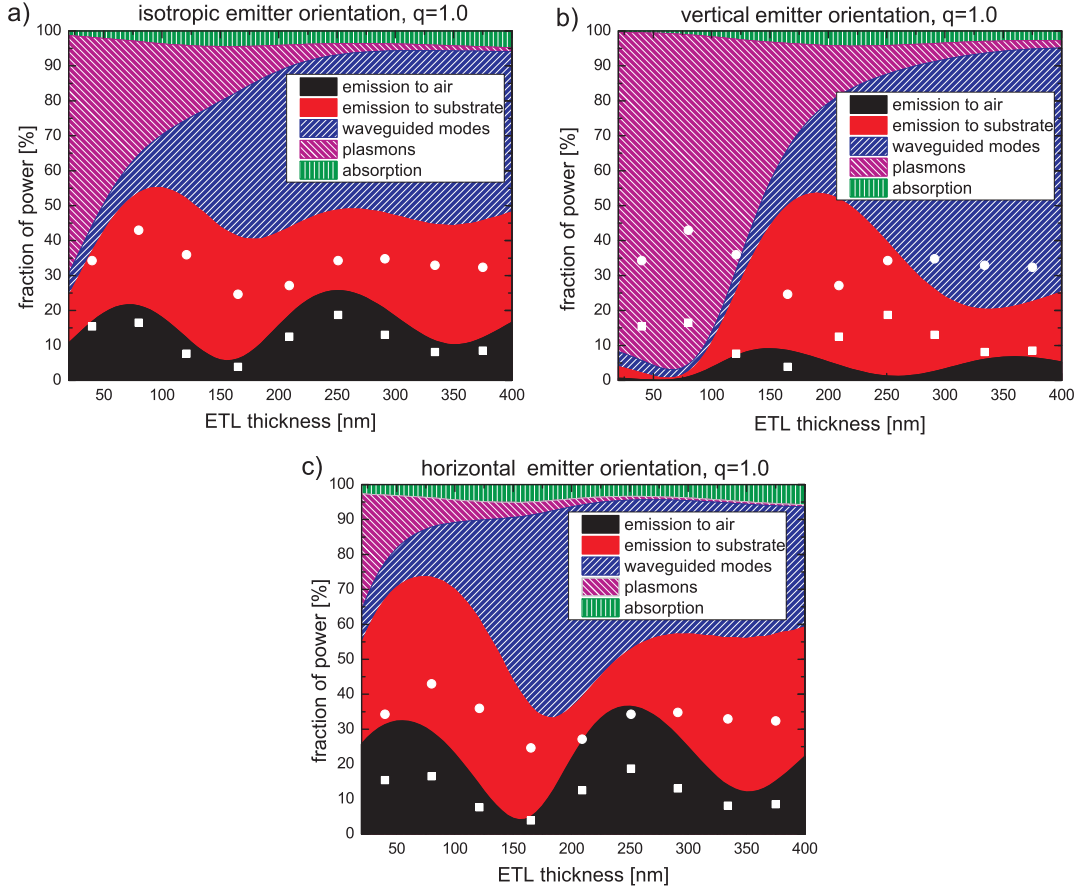


Figure 5.24: Simulated power dissipation to the different optical modes as a function of the ETL thickness for a) isotropic, b) vertical and c) horizontal emitter orientation. The radiative quantum efficiency was set to unity. White squares and dots represent external quantum efficiency measurements of the OLED stacks under investigation at a current density of 1 mA/cm^2 to avoid current induced quenching effects without and with an attached outcoupling structure, respectively. Graphics taken from Ref. [65]. Sample structure: Glass/ITO/HTL/EBL/EML ($\text{Ir}(\text{MDQ})_2(\text{acac}):\alpha\text{-NPD}$)/HBL/ETL/Ag.

be preferred. As expected from the previous results, the behavior of horizontally and isotropically oriented emitters differs only little in the positions of the maxima and minima. However, horizontally oriented emissive dipole moments can yield much higher external quantum efficiencies for both, direct emission and if outcoupling enhancements by means of macroscopic ray optics are used, giving access to the substrate modes of the device. This is mainly caused by the radiation pattern of an electrical dipole, emitting most of its energy perpendicular to its orientation. In the case of the used definition for OLEDs, horizontally oriented emissive dipoles are dissipating their energy mainly under low angles with respect to the surface normal, resulting in a comparable low fraction of

light that suffers from total internal reflection at the glass/air interface. Furthermore, the coupling of energy to optical modes that require high in-plane wavevectors, such as waveguided modes and surface plasmon polaritons, is drastically reduced for horizontal emitter orientation for almost all ETL thicknesses. Figure 5.24 c) demonstrates, that the fraction of power that is coupled to waveguided modes is much less pronounced in the horizontal than in the vertical case. Moreover, the coupling to SPPs especially for very low emitter/cathode distances is only very weak. As a consequence, it is possible to achieve remarkably high external quantum efficiency values of 37 % and 74 %, for direct emission and if outcoupling structures are used, respectively [53, 59, 65]. However as in Fig. 5.23, the external quantum efficiency values, measured for a low current density of 1 mA/cm^2 to avoid quenching processes, are not very well described by any of the simulations for the extreme cases. Hence, the orientation and the RQE of the emitting system have to be adjusted for the OLED stack under investigation. Nevertheless, a mainly vertical emitter orientation can be excluded, combining the comparisons of the simulations with the measured data points for the excited states lifetimes and the external quantum efficiency, due to their completely different behavior for the variation of the ETL thickness.

However, emitter orientation complicates the determination of the radiative quantum efficiency enormously. If this feature is not taken into account, the RQE of an emitting system will be overestimated for a prevailing horizontal orientation of the emitting dipoles, while the outcoupling factor is underestimated. Moreover, the efficiency analysis will be completely erroneous for a prevailing vertical emitter orientation. In order to emphasize this consequence and to demonstrate how big the mistakes can be if non-isotropic emitter orientation is not taken into account properly for efficiency analysis in state-of-the-art OLEDs, simulations for the devices under investigation with strongly differing radiative quantum efficiencies and corresponding emitter orientations have been performed. Figure 5.25 illustrates these results for an isotropic orientation with a corresponding RQE of 90 %, and for horizontal orientation and an RQE of 65 %. Both simulations are very similar for the changes of the excited states lifetimes for ETL thicknesses higher than 100 nm and the experimental data points can fit both curves depending on the intrinsic excited states lifetime used for normalization. If only data points with ETL thicknesses higher than 100 nm are available, a huge overestimation of the RQE of the emitting system would follow for a completely horizontal emitter orientation instead of the expected isotropic one. This clearly demonstrates the importance of using as many experimental data points as possible, especially at small emitter/cathode distances for the presented determination of the radiative quantum efficiency of an emitting system

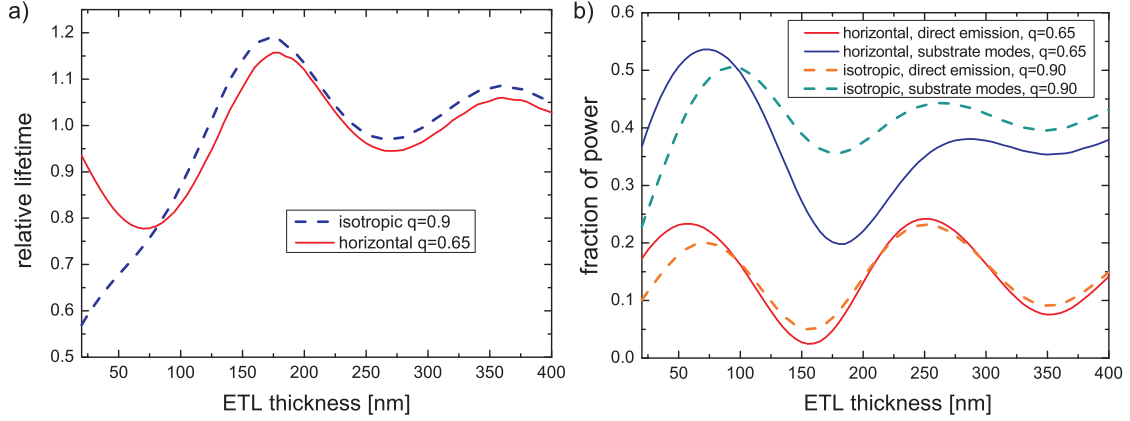


Figure 5.25: a) Simulation of the relative lifetime changes for the OLED stack under investigation as a function of the ETL thickness and for different emitter orientations with different RQEs. b) Simulation of the EQE with and without an outcoupling structure for the OLED stack under investigation as a function of the ETL thickness and for different emitter orientations with different RQEs. Graphics taken from Ref. [65]. Sample structure: Glass/ITO/HTL/EBL/EML ($\text{Ir}(\text{MDQ})_2(\text{acac}):\alpha\text{-NPD}$)/HBL/ETL/Ag.

via time-resolved measurements, due to the high sensitivity for orientation effects at small ETL thicknesses.

Additionally, simulations for the external quantum efficiency with and without attached outcoupling structures for the same combinations of RQE and orientation have been performed, as illustrated in Fig. 5.25 b). Here, the situation is comparable to the excited states lifetimes. While the simulation for direct emission is very similar for both assumptions, the characteristics, if an outcoupling structure is used, are completely different. Hence, a consistent determination of the radiative quantum efficiency of an emitting system is only possible if both measurements are performed. Otherwise, wrong estimation about the RQE and the orientation of the emissive dipole moments could follow. Therefore, it should be noted, that the best results will be obtained, if a combination of all three measurements compared with optical simulations with the RQE (q) and the anisotropy factor (θ) as free parameters are performed. Thus, these theoretical considerations should now be proven for a common red phosphorescent emitting system. The emitting system consisting of 8 wt% $\text{Ir}(\text{MDQ})_2(\text{acac})$ doped in an $\alpha\text{-NPD}$ matrix exhibits a prevailing horizontal emitter orientation with an anisotropy factor of $\theta = 0.25$ [58, 59]. This means that the dipole moments of the emitting species are predominantly oriented parallel to the device surface. In previous publications, the radiative quantum efficiency of this common emitting system was determined to 84 % [72, 123], however an isotropic orientation of the emissive dipole moments was assumed.

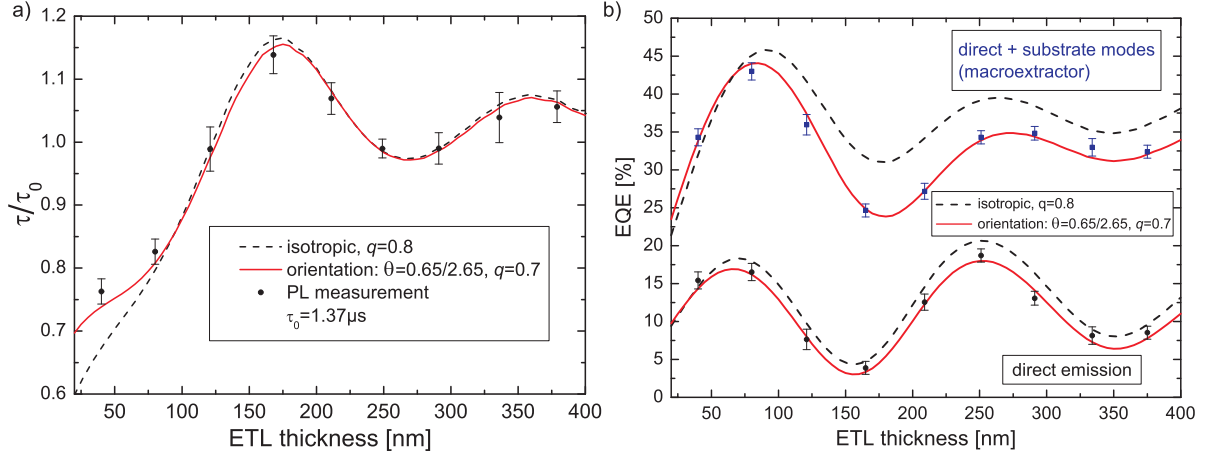


Figure 5.26: Simulations for different RQEs and emitter orientations as a function of the ETL thickness for the OLED stack under investigation and the comparison of these results with measured data points for a) excited states lifetimes and b) the external quantum efficiency with and without outcoupling structures. EQE measurements have been performed by a current density of 1 mA/cm^2 . Graphics taken from Ref. [65]. Sample structure: Glass/ITO/HTL/EBL/EML ($\text{Ir}(\text{MDQ})_2(\text{acac}):\alpha\text{-NPD}$)/HBL/ETL/Ag.

Figure 5.26 demonstrates the differences in the determination of the RQE of the emitting system for an isotropic distribution and if the prevailing horizontal emitter orientation is taken into account. While the simulation for both orientations with different RQE values ($q_{\theta=1/3} = 0.80$ and $q_{\theta=0.25} = 0.70$) fits the measured excited states lifetimes (excitation with nitrogen laser at 337.1 nm) in a reasonable way for ETL thicknesses higher than 100 nm , only the mainly parallel emitter orientation with an RQE of 70% can reproduce the measured behavior for smaller ETL thicknesses in an appropriate way. This clearly illustrates the importance of available data points at small emitter/cathode distance to achieve a reliable determination of the RQE of an emitting system via time-resolved measurements. However, the situation becomes even more drastical, if external quantum efficiency measurements (performed for a current density of 1 mA/cm^2) are additionally taken into account. In this case, the deviations of both simulations are remarkably pronounced especially for ETL thicknesses over 75 nm using the extracted substrate modes of the devices. While the measurements for the direct emission are well reproduced by both simulations, using the same conditions as for the excited states lifetime changes, the measurement with extracted substrate modes can only be described in a consistent way by the prevailing horizontal emitter orientation with an RQE of 70% . This clearly enforces taking into account possible deviations from isotropy to achieve a consistent efficiency analysis in state-of-the-art OLEDs, particularly for phosphorescent

emitting systems. Otherwise, an erroneous over- or underestimation of the factors determining the external quantum efficiency would follow. Additionally, the charge carrier balance factor (γ) of the devices can be estimated to be unity, due to the assumption of a perfect charge carrier balance in the simulations that describes the measured EQE values nearly perfectly.

In addition to the successful implementation of non-isotropic emitter orientation into the presented method for determining the emitters radiative quantum efficiency, the current dependent quenching was analyzed using the pulse sequence presented in chapter 4. Therefore, the photoluminescence lifetime was detected for different current densities through the devices with the varying ETL thickness. Unfortunately, it was not possible to perform the RQE determination via the changes of the excited states lifetime as a function of the ETL thickness, due to a too high possible step width for the modulation of the applied voltage by the available wave generator. Hence, an exemplary investigation of the current induced quenching processes will be presented for the device exhibiting an ETL thickness of 40 nm. For more information about the investigation of the remaining eight devices and a detailed error analysis, please refer to Ref. [124].

Figure 5.27 illustrates the current-voltage-luminance characteristics of the device with an ETL thickness of 40 nm. Charge carrier injection begins at a voltage of about 2 V, followed by a very fast increase of both the current density and the emitted luminance until a slight saturation occurs for voltages over 5 V. This measurement is the basis for the investigation of TPQ in this device, because with this information it is possible to choose the working point of the OLED properly for the following EL-PL-pulse sequence with an analysis of the photoluminescence lifetimes as a function of the current flow through the device.

Figure 5.28 a) demonstrates the measured time-resolved photoluminescence decay times (excitation via nitrogen laser with a wavelength of 337.1 nm) as a function of the current density. The excited states lifetimes have been determined by mono-exponential fit functions for all current densities. This gives a hint, that the main quenching process even at high current densities is based on triplet-polaron-quenching and not caused by triplet-triplet-annihilation, that would result in bi-exponential decay curves. It can clearly be seen, that the excited states lifetimes are drastically reduced with an increasing current flow through the device. The measured behavior can be reproduced by a reciprocal logarithmic fit function:

$$\tau(j) = \frac{1}{c + b \cdot \ln(j - a)}. \quad (5.3)$$

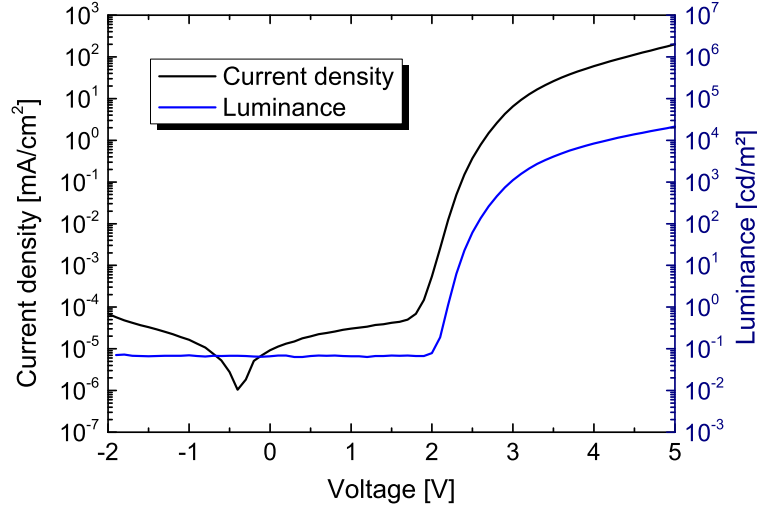


Figure 5.27: IVL characteristics of the device exhibiting an ETL thickness of 40 nm. Sample structure: Glass/ITO/HTL/EBL/EML ($\text{Ir}(\text{MDQ})_2(\text{acac}):\alpha\text{-NPD}$)/HBL/ETL/Ag.

Therein, c represents the radiative rate of the excited molecules modified by the Purcell factor for an ETL thickness of 40 nm ($F(40\text{ nm}) \approx 1.4$) and the determined value ($c = 7.1 \cdot 10^5 \text{ s}^{-1} = F \cdot \Gamma_r = 1.4 \cdot 5.1 \cdot 10^5 \text{ s}^{-1}$) is in good agreement with a previous publication [125]. The second term in the denominator represents the current dependent non-radiative rate ($\Gamma_{\text{nr}}(j)$). However, the physical background of the variables a and b and the logarithmic behavior is not yet fully understood and should be analyzed in more detail in further investigation beyond the scope of this thesis. Nevertheless, with these results and the assumption of an unchanged radiative rate and the previously determined intrinsic excited states lifetime of the emitting molecules, it is possible to calculate the growth of the non-radiative rate caused by the current flow through the device, as it is illustrated in Fig. 5.28 b), using

$$\tau(j)^{-1} - \Gamma_r = \Gamma_{\text{nr}}(j). \quad (5.4)$$

The calculated behavior can be described well by the logarithmic function used in Eq. 5.4 for the non-radiative rate $\Gamma_{\text{nr}}(j)$.

Additionally, it is possible to calculate the changes of the radiative quantum efficiency as a function of the current density via the determined non-radiative rates and compare these findings with measurements of the efficiency roll-off of the external quantum efficiency extracted from current-voltage-characteristics. This comparison allows for drawing conclusions about possible changes of the charge carrier balance for high

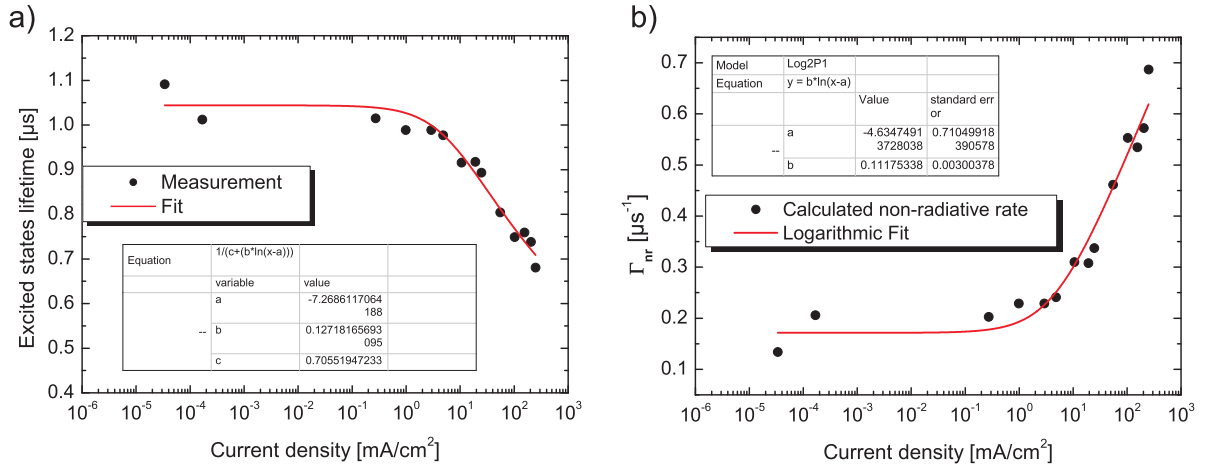


Figure 5.28: a) Measured excited states lifetimes as a function of the current density. A reciprocal fit function can describe the measured behavior. b) Calculated non-radiative rate as a function of the current density. The radiative rate was assumed constant for these calculations. A logarithmic fit function can reproduce the measured behavior. Sample structure: Glass/ITO/HTL/EBL/EML ($\text{Ir}(\text{MDQ})_2(\text{acac})$): α -NPD)/HBL/ETL/Ag.

current densities. If this were the case, the electrically measured efficiency roll-off should be more pronounced than the decrease of extracted values from the time-resolved photoluminescence decay curves. Both investigations of the RQE changes as a function of the current density are depicted in Fig. 5.29 resulting in a nearly perfect agreement of both methods. This gives strong evidence, that the efficiency roll-off at high current densities can be exclusively explained by triplet-polaron-quenching and other effects such as TTA (due to the mono-exponential decay for all current densities) or a charge carrier imbalanced γ^* (due to a missing additional decrease component, see Fig. 5.29) can be excluded for current densities up to $200 \text{ mA}/\text{cm}^2$ for this device. The analysis of the other devices with a variation of the ETL thickness shows a very similar behavior. However, for more information, please refer to Ref. [124].

To sum up this subsection, an investigation of all factors determining the EQE of an organic light-emitting diode has been demonstrated. Additionally, the importance of taking into account possible deviations from an isotropic orientation of the emissive dipole moments of (phosphorescent) molecules influencing the effective radiative quantum efficiency and the outcoupling factor of the devices has been demonstrated. Moreover, the basic process behind the efficiency roll-off at high current densities has been investigated and was identified as triplet-polaron-quenching for this OLED stack.

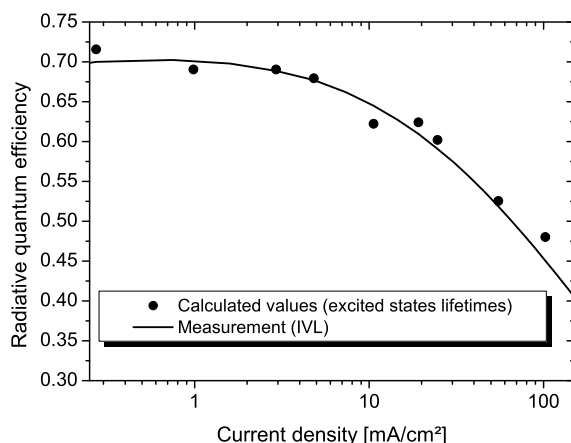


Figure 5.29: Via time-resolved measurements calculated (dots) and from IVL characteristics extracted (solid line) changes of the radiative quantum efficiency as a function of the current density. The very good agreement of both measurements gives evidence for TPQ being the main responsible effect for the efficiency roll-off for this device. Sample structure: Glass/ITO/HTL/EBL/EML ($\text{Ir}(\text{MDQ})_2(\text{acac})\text{:}\alpha\text{-NPD}$)/HBL/ETL/Ag.

5.5 Comprehensive efficiency analysis of fluorescent OLEDs

In the previous section, an efficiency analysis of state-of-the-art phosphorescent OLEDs using a mainly horizontally oriented emitting system was demonstrated including a determination of three of the four factors determining the external quantum efficiency of a device. Thereby, EQE measurements have been compared with time-resolved photoluminescence lifetime measurements to achieve consistent and reliable results. The radiative exciton fraction was set to unity due to the phosphorescent emitting system of the devices under investigation.

However, in this section a comprehensive efficiency analysis will be presented taking into account a possible increase of the radiative exciton fraction, which will lead to a boost in efficiency. Therefore, it is essential to combine electro- and photoluminescent time-resolved spectroscopy with EQE measurements to avoid wrong estimations of the four factors determining the EQE. The effect of an enhanced radiative exciton fraction for fluorescent devices was previously reported by several other groups for fluorescent emitters explained by either triplet-triplet-annihilation [13, 34, 36, 48] or thermally activated delayed fluorescence [37, 40, 41]. However, a reliable determination of the modified

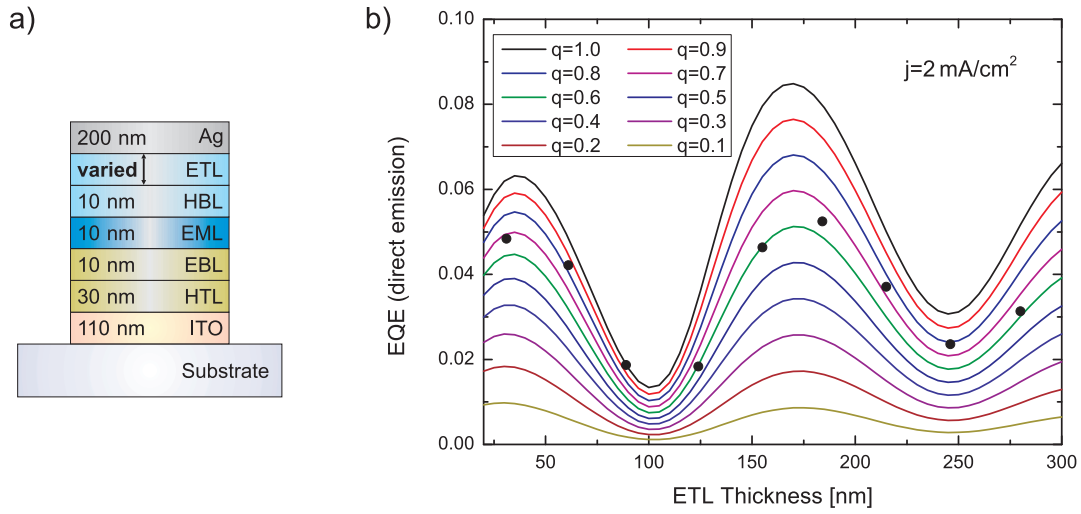


Figure 5.30: a) Device stack under investigation exhibiting a blue fluorescent emitting system. b) Comparison of measured EQE values for a current density of 2 mA/cm^2 for the fluorescent OLED stack under investigation (dots), with the simulated behavior (solid lines) for different RQEs as a function of the ETL thickness. The radiative exciton fraction was set to 25 %, while a perfect charge carrier balance was assumed. Sample structure: Glass/ITO/HTL/EBL/EML (blue)/HBL/ETL/Ag.

radiative exciton fraction, especially for emitting systems showing TADF, was still missing and will be presented in the following.

The OLED structure under investigation is shown in Fig. 5.30 a). Corresponding to the previous sections, the ETL thickness was subsequently varied to ensure a consistent efficiency analysis. The emitting system consists of a blue fluorescent emitter doped into a matrix material. The chemical structures of both molecules cannot be disclosed. However, the emitting system exhibits an almost completely horizontal orientation of its emissive dipole moments resulting in an anisotropy factor of $\theta = 0.2/2.2 = 0.09$ [126] and all simulations presented in this section have considered this deviation from isotropy.

Figure 5.30 b) illustrates the comparison of electrically measured EQE values for direct emission at a current density of 2 mA/cm^2 for the devices with the different ETL thicknesses and optical simulations of the extracted power for a variation of the radiative quantum efficiency of the emitting system and a radiative exciton fraction of 25 %. The mainly horizontally oriented emissive dipole moments of the emitting species is already taken into account. However, none of the simulated behaviors fits the measured data points in a consistent way and a very rough estimation would yield an RQE of 70 %. This gives a hint, that the radiative exciton fraction might aberrate from the intrinsic value, because the RQE of the emitting system is changing the relative heights of first and

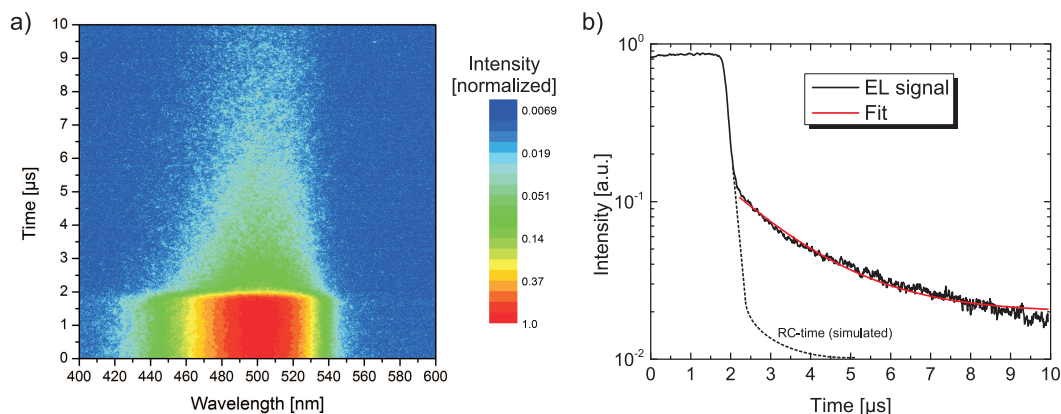


Figure 5.31: a) Streak camera image of a pulsed electrically driven experiment for the OLED under investigation exhibiting an ETL thickness of 184 nm. A slow decrease of the electroluminescence signal after the excitation pulse is clearly detectable. b) Intensity integrated over the emission wavelengths versus the time extracted from the streak camera image. After a quite fast decay over one magnitude after the electrical pulse, a slow decrease of the signal is obvious. Sample structure: Glass/ITO/HTL/EBL/EML (blue)/HBL/ETL/Ag.

second maximum for different values, while η_r is only a linear factor. Hence, electrically driven time-resolved measurements have been performed. Typically, the decay time after the end of the electrical square wave voltage should exhibit a quite fast decay time determined by the RC-time of the device for fluorescent emitters with an excited states lifetime in the range of a few nanoseconds. In contrast, the OLED stack under investigation shows a very pronounced slow electroluminescence decay even after the RC-time of the device, as can clearly be seen from Fig. 5.31 for the device exhibiting an ETL thickness of 184 nm.

After a quite fast decay over one magnitude of the electroluminescence signal, a second decay component with a time-constant of several μ s appears. This signal exhibits the same spectrum as the prompt fluorescence of the device, and therewith phosphorescence can be excluded due to the missing red shift of the spectrum. Thus, only two effects, namely triplet-triplet-annihilation and thermally activated delayed fluorescence, remain as possible explanations.

In order to investigate the underlying process of this delayed fluorescence, time-resolved photoluminescence in the microsecond range has been performed. If TTA is the responsible effect, no delayed signal should be obvious in this experiment, due to the very weak spin orbit coupling of fluorescent emitters and hence no significant population of the triplet states of the emitting molecules by laser excitation.

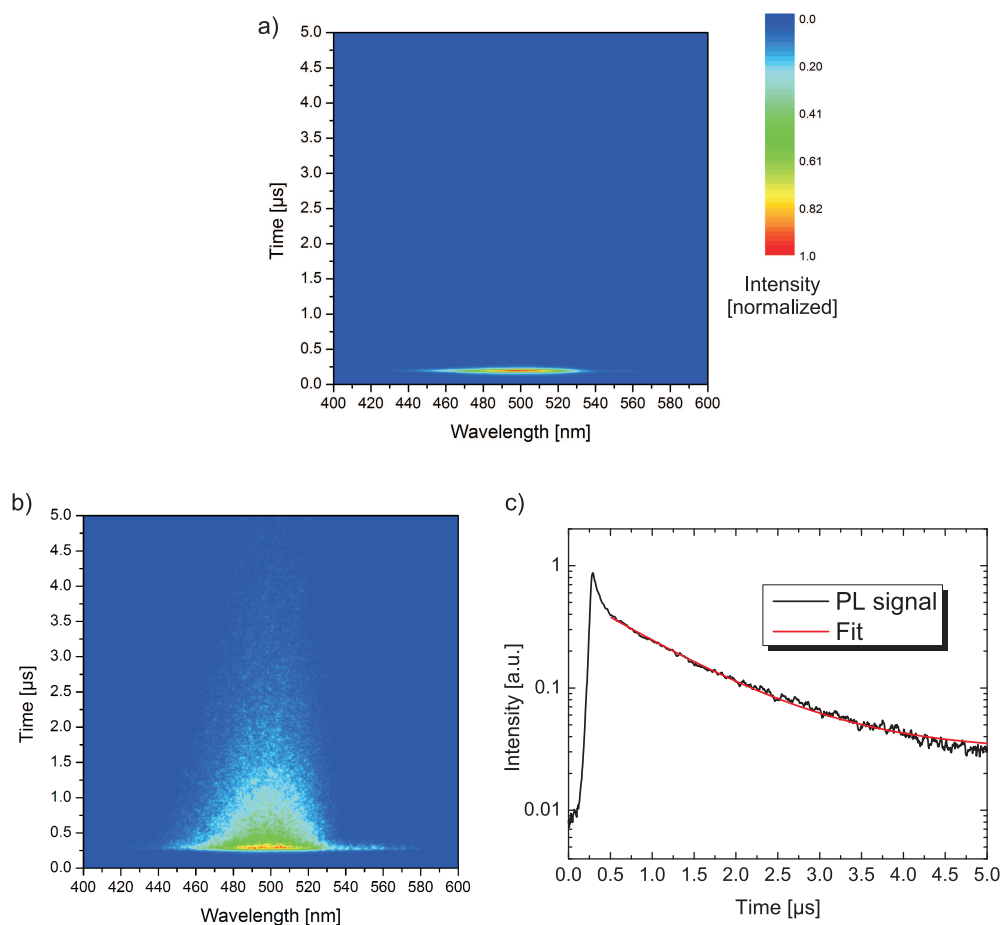


Figure 5.32: Streak camera images of time-resolved photoluminescence measurements of the OLED under investigation with an ETL thickness of 184 nm a) without and b) with activated gate function of the streak camera. c) Intensity integrated over the emission wavelengths versus the time extracted from the streak camera image demonstrating the delayed component of the photoluminescence. A logarithmic scale was used for the intensity and the legend in a) is also valid for b). Sample structure: Glass/ITO/HTL/EBL/EML (blue)/HBL/ETL/Ag.

Figure 5.32 illustrates the streak camera images of the time-resolved photoluminescence, a) under standard detection conditions, and b) if the gated mode of the streak camera is used for the device exhibiting an ETL thickness of 184 nm. This function allows for a suppression of very fast decaying signals, e.g. prompt fluorescence, in nanosecond steps. In Fig. 5.32 b) the prompt fluorescence signal, that would saturate the streak camera for the used amplifying conditions, is cut off. It should be noted that the differences of Fig. 5.32 a) and b) only consist of the used gate function and a lower gain in a) and that a logarithmic scale for the intensity was chosen in the graphic. All other settings

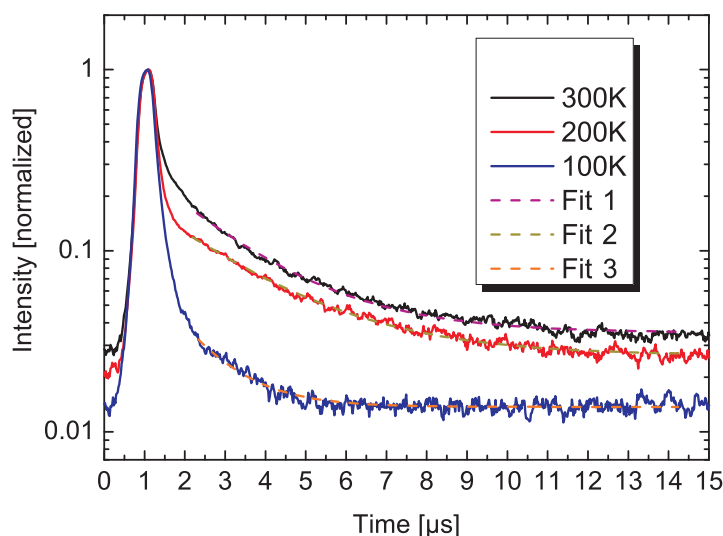


Figure 5.33: Time-resolved behavior of the photoluminescence signals of the device under investigation for different temperatures. The intensity depletes and the excited states lifetime of the delayed fluorescence increases with decreasing temperature. This gives strong evidence for TADF as the responsible process for the delayed fluorescence. Sample structure: Glass/ITO/HTL/EBL/EML (blue)/HBL/ETL/Ag.

of excitation and detection are identical. However, a clear delayed fluorescence with an excited states lifetime of several microseconds can be detected using the gate function of the streak camera, as it is obvious from Fig. 5.32 b). This gives a clear evidence that TADF and not TTA is the underlying process for the delayed fluorescence of these blue OLEDs.

However, time-resolved, temperature dependent photoluminescence measurements are carried out in order to confirm this hypothesis. While the delayed fluorescence should become more pronounced in the case of triplet-triplet-annihilation, it should deplete continuously for a decreasing temperature if TADF is the underlying process. Figure 5.33 demonstrates the time-resolved behavior of the delayed fluorescence for different temperatures for the device under investigation. It can clearly be seen, that the intensity of the delayed part is drastically reduced, while the excited states lifetime of the delayed fluorescence is continuously increased for a decreasing temperature. This gives strong evidence for TADF as the responsible process behind the delayed signal and TTA can definitely be excluded. With this information it is now possible to perform a comprehensive efficiency analysis of the OLEDs consisting of this blue, fluorescent emitting system.

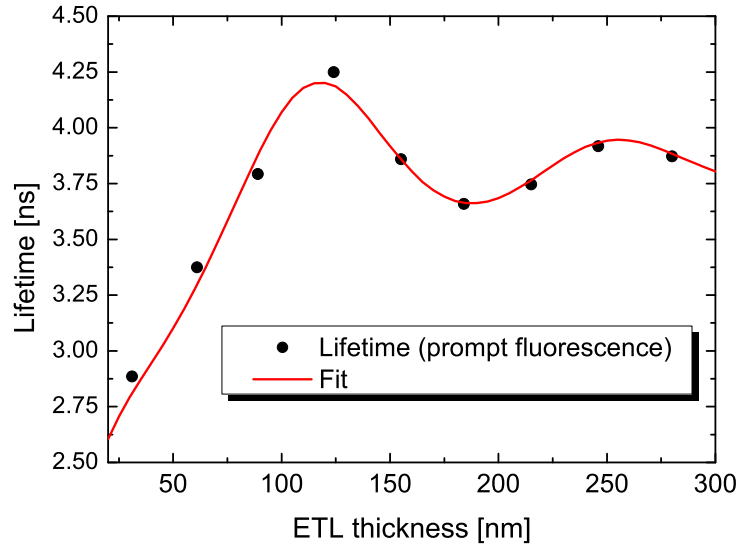


Figure 5.34: Dots: Measured photoluminescence excited states lifetimes of the prompt fluorescence for the devices exhibiting different ETL thicknesses. Solid line: Best fit of the measured data points resulting in a radiative quantum efficiency of 0.50 ± 0.04 and an intrinsic excited states lifetime of (3.75 ± 0.03) ns. Sample structure: Glass/ITO/HTL/EBL/EML (blue)/HBL/ETL/Ag.

However, although it is now known that the radiative exciton fraction is changed by TADF, the determination of the radiative quantum efficiency of the emitting system should be first performed via the changes of the excited states lifetime with the emitter/cathode distance, because the radiative and the non-radiative rate of the prompt fluorescence should not be strongly influenced by TADF. Figure 5.34 demonstrates the measured photoluminescence excited states lifetimes of the prompt fluorescence for the devices exhibiting different ETL thicknesses. The excitation was achieved by the PLP10-038 (wavelength 375 nm), because this laser system exhibits a very short pulse length (80 ps) appropriate for the excited states lifetimes of this blue emitting system in the range of only a few nanoseconds. Fitting the measured behavior of the excited states lifetimes using the simulated characteristics of the Purcell factor for the OLED stack, yields an RQE of 0.50 ± 0.04 and an intrinsic excited states lifetime of (3.75 ± 0.03) ns. This is considerably lower than the estimated value of 70 % for the determination via the direct emission with an assumption of a radiative exciton fraction of 25 %.

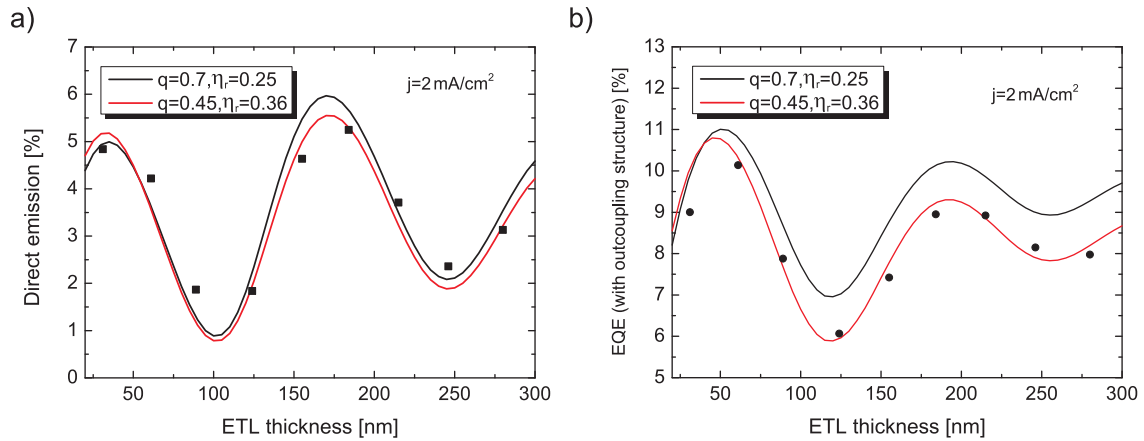


Figure 5.35: Efficiency analysis via EQE measurements using the variable ETL thickness approach. a) Determination of the RQE of the emitting system via EQE measurements (direct emission; dots) combined with fits using a fixed η_r of 25 % (black curve) and setting η_r as a free parameter yielding an RQE of 0.70 ± 0.05 and 0.45 ± 0.05 with a radiative exciton fraction of $(36 \pm 3) \%$, respectively. b) Measurement of the EQE using a macroextractor giving access to the substrate modes of the devices. Solid lines represent simulations of the EQE behavior using the parameters q and η_r as determined from a). Only the lower RQE of the emitting system with an enhanced radiative exciton fraction can describe the measured behavior. Sample structure: Glass/ITO/HTL/EBL/EML (blue)/HBL/ETL/Ag.

In order to verify this result, the determination of the radiative quantum efficiency of the emitting system via EQE measurements was performed simultaneously for a fixed radiative exciton fraction of 25 % and setting η_r as a free parameter in the fitting process for the direct emission. The results of the EQE measurements at a current density of 2 mA/cm^2 and the fits for the different parameter conditions are presented in Fig. 5.35 a). Both fits can describe the measured data points in a reasonable way, yielding RQEs of 0.70 ± 0.05 and 0.45 ± 0.05 with a radiative exciton fraction of 25 % (fixed) and $(36 \pm 3) \%$, respectively. The result with the enhanced radiative exciton fraction is in very good agreement with the determined value of the radiative quantum efficiency of the emitting system via the analysis based on the excited states lifetimes of the prompt fluorescence. This gives a hint, that the TADF is strongly influencing the radiative exciton fraction of the devices.

In addition the external quantum efficiency using macroscopic outcoupling structures, giving access to the substrate modes of the devices, has been investigated. These results are illustrated in Fig. 5.35 b). The solid lines represent simulations of the behavior of the external quantum efficiency using the parameters determined by the direct emission analysis. It can clearly be seen, that only the simulation for the radiative quantum

efficiency of 45 % with an enhanced radiative exciton fraction of 36 % can describe the measured data points in an appropriate way. Therewith, only the result of a TADF induced increase of η_r can describe all measurements in a consistent way.

However, the result of $\eta_r = 0.36$, which is remarkably 1.5 times higher than the normal value, should be understood as a lower limit of this factor, due to the assumption of a perfect charge carrier balance for the fits and simulations performed for the devices under investigation. Nevertheless, this clearly demonstrates the importance of combining electrical excitation and photoluminescence, steady state and time-resolved measurements to ensure a reliable efficiency analysis particularly in terms of orientation effects of the transition dipole moments of the emitting species and possible deviations of the typical radiative exciton fraction due to processes such as TTA or TADF.

Indeed, the integration of changes in the radiative exciton fraction was successfully demonstrated with the efficiency analysis method used in this thesis. Therewith, it was possible to determine all four factors determining the external quantum efficiency actually for a fluorescent emitting system exhibiting nearly a complete horizontal orientation of its emissive dipole moments and simultaneously an enhanced radiative exciton fraction due to thermally activated delayed fluorescence. This effect has to be taken into account properly for device optimization in terms of layer thickness adjustment, because the optimal position in the OLED cavity depends on the RQE of the emitting system but not on the radiative exciton fraction.

5.6 Conclusions and further work

This chapter started with discussing, in terms of optical simulations, the problems of the determination of the radiative quantum efficiency of emitting systems with standard methods using an integrating sphere. Particularly, considering possible deviations from isotropic emitter orientation were pointed out.

Hence, a different method of RQE determination using simplified structures was presented. This concept is based on a subsequent variation of the distance of the emitting system to a highly reflecting interface, e.g. a metallic layer, in terms of layer thicknesses of optical spacers and comparing the changes of excited states lifetimes with numerical simulations. Two different optical spacers, SiO_2 and LiF , have been investigated and the advantages and disadvantages of both have been pointed out. With this method it was possible to determine the radiative quantum efficiency of two phosphorescent emitting systems. The first one was Ir-SC4 doped in a PMMA matrix and the second was the very commonly used emitting system consisting of $\text{Ir}(\text{ppy})_3$ doped into a CBP matrix resulting in RQEs of $(70 \pm 10) \%$ and $(83 \pm 3) \%$, respectively. Additionally, the presented method was extended by a fitting procedure to determine the RQE from excited states lifetime measurements.

Thereafter, a method to determine the RQE of an emitting system inside a whole OLED stack was presented using microcavity structures by the implementation of a thin metal layer on top of the ITO anode of the samples. Due to electrical instabilities, however, it was only possible to determine the RQE of the emitting system ($\text{Ir}(\text{ppy})_3\text{:CBP}$) via time-resolved photoluminescence measurements. Nevertheless, this method allows for a determination of the RQE of the emitting system to $(75 \pm 7) \%$, which is in good agreement with the previous results. However, this method is not appropriate for a comprehensive efficiency analysis of complex, multi-layered state-of-the-art OLED structures with electro- and photoluminescence measurements.

Hence, the approach of the simplified structures was expanded to complete OLEDs by a subsequent variation of the ETL thickness and therewith the emitter/mirror distance. The electrical properties of these samples are not changing with the ETL thickness, due to the use of conductivity doped transport layers, but the cavity length and thus the influence of the power distribution between the optical modes of the OLED and the effective radiative quantum efficiency is strongly differing with the ETL thickness. This allows for a determination of the RQE of emitting systems in complex OLED structures with both, the measurement of excited states lifetimes for the variation of the emitter/cathode distance and via electrically driven external quantum efficiency mea-

measurements with and without macroscopic outcoupling structures giving access to the substrate modes of the devices. Therewith, it was possible to investigate the influence of the matrix material on the RQE of the emitting systems exhibiting Ir(ppy)₃ as emissive species. Thus, it was possible to demonstrate the importance of taking into account the matrix material for emitting molecules and its influence on the radiative quantum efficiency of the whole emitting system, which can vary between 50 % and 85 % depending on the used matrix for the common emitter Ir(ppy)₃.

Additionally, the influence of the current density on the effective radiative quantum efficiency of the used emitting system was pointed out including an analysis of its influence on device optimization in terms of layer thickness adjustment for the planned application conditions.

Subsequently, the main focus was on the influence of non-isotropic orientation of the transition dipole moments of the emitting molecules on the determination of the radiative quantum efficiency in state-of-the-art OLEDs. First, the differences between the extreme conditions of vertical, horizontal and isotropic emitter orientation was pointed out in terms of optical simulations. Moreover, possible mistakes in the context of the determination of the RQE of an emitting system showing horizontal emitter orientation were elaborated. Afterwards, the possibilities of emitter orientation for efficiency enhancement have been demonstrated resulting in very high external quantum efficiencies of 37 % and 74 % for direct emission and if the substrate modes of the device are coupled out using ray optics, respectively, assuming perfect horizontal orientation of the emissive dipole moments and a radiative quantum efficiency of unity. With these results, it was possible to demonstrate a comprehensive efficiency analysis of the red phosphorescent emitting system Ir(MDQ)₂(acac): α -NPD exhibiting a predominant horizontal orientation of the transition dipole moments of the emitting species. These findings have been compared with results from other groups who did not take into account the non-isotropic orientation, leading to an overestimation of the RQE and an underestimation of the outcoupling factor of the devices. Finally, the influence of the current density on the efficiency and the induced efficiency roll-off at high brightness was investigated using a combination of electrical and laser induced excitation in a time-resolved experiment. With this method it was possible to investigate the main responsible effect of the roll-off and triplet-polaron-quenching was identified as being the underlying process. Triplet-triplet-annihilation and imbalances of the injected charge carriers could be excluded for current densities up to 200 mA/cm².

The last section of this chapter has discussed the influence of a deviation of the radiative exciton fraction from its typically assumed value of 25 % for fluorescent emitting systems.

Therefore, the detected delayed fluorescence of a state-of-the-art blue fluorescent OLED, exhibiting nearly perfect horizontal emitter orientation, was unambiguously identified as thermally activated delayed fluorescence. The other effect that could be the reason for the delayed signal, triplet-triplet-annihilation, was excluded by time-resolved, temperature dependent photoluminescence measurements. Moreover, it was demonstrated that a reliable determination of all four factors influencing the external quantum efficiency of organic light-emitting diodes is possible without any adhoc assumptions.

Therewith, the successful implementation of non-isotropic emitter orientation, current induced quenching processes and thermally activated delayed fluorescence in the initially presented approach for a comprehensive efficiency analysis of state-of-the-art OLEDs was achieved.

The next step of future improvement of the presented comprehensive efficiency analysis is implementing multi-colored stack systems. First, the energy transfer processes of phosphorescent red and green emitting systems located next to each other should be investigated in state-of-the-art OLEDs. First experiments have shown the existence of an energy transfer via triplet excitons traveling from the host and/or the doped green phosphorescent emitter molecules over a matrix material to red phosphorescent emitters, resulting in a boost of red emission as a function of the distance between both emitting systems [80]. Time-resolved electroluminescence and photoluminescence spectroscopy would be a powerful tool to investigate the underlying physical processes and the energy transfer rates via changes in excited states lifetimes of both emitting species. Additionally, the efficiency analysis should also be performed for stacked OLEDs using charge generation layers. In these systems energy transfer between the red and the green unit is fully suppressed. However, both emitting systems can be optimized by layer thickness adjustment. Determining the radiative quantum efficiencies of the single emitting systems in both types of dual-colored OLEDs is a promising investigation for profound understanding of the underlying (photo-)physical processes of efficiency and energy transfer mechanisms.

Second, based on this research it should be the aim to achieve a comprehensive efficiency analysis in full colored white OLEDs consisting of three (red, green, blue) or four (red, yellow, green, blue) emitting systems, including hybrid (fluorescent blue and phosphorescent red and green) or full phosphorescent emitting systems and stacked device layouts (two times white, or stacked single-colored devices).

Indeed, the previously mentioned advantages of emitter orientation and changes of the radiative exciton fraction of the emitting systems have to be taken into account properly. A first investigation of an energy transfer from a blue fluorescent to a red phosphorescent

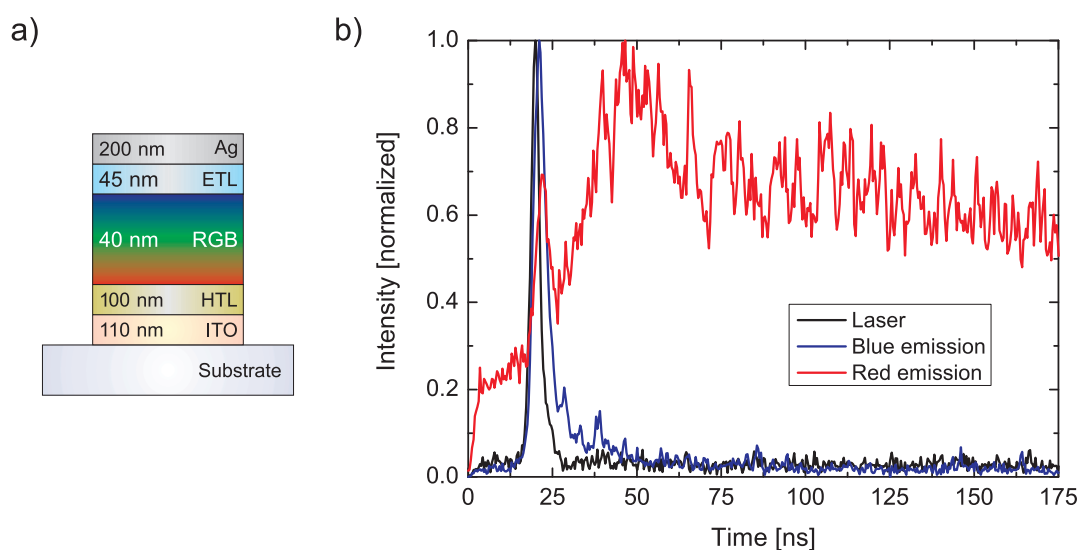


Figure 5.36: a) RGB-OLED stack under investigation. b) Time-resolved photoluminescence spectroscopy of the RGB-OLED. Black line: Laser signal; blue line: blue emission; red line: red emission. A slow, delayed increase of the red emission is caused by an energy transfer process in the device under investigation. The red emission signal before laser excitation can be an artifact caused by a very long lifetime of the emission in the range of the repetition rate of the laser and/or by normalization of the signals (bad signal to noise ratio).

emitter by time-resolved photoluminescence spectroscopy is illustrated in Fig. 5.36 for the device already presented in Fig. 3.3 d). The delay between red and blue emission can clearly be seen, giving a hint for energy transfer between both adjacent emitting systems.

Understanding the (photo-)physical effects behind the efficiency of white OLEDs is the basis for further optimization and improvement and therewith to enter the commercial sector of general lighting.

Moreover, the current dependence of the non-radiative rate of the emitting molecules during the efficiency roll-off at high current densities should be investigated to identify the exact principles behind (current induced) quenching processes. With this comprehension it should be possible to prevent or minimize the efficiency roll-off at high brightness, which would result in an increase in power efficiency and long-term stability.

DEGRADATION PROCESSES IN OLEDs

The biggest advantage of inorganic light-emitting diodes over their organic counterparts (beside fabrication cost and efficiency) are high lifetimes (LT), i.e. of long-term stability during electrical operation. While inorganic (white) LEDs exhibit lifetimes of more than 50,000 hours, this mark is not yet reached for white OLEDs (at the required brightness for general lighting), e.g. due to the unavailability of stable phosphorescent blue emitters. It should be noted, that the lifetime of OLEDs is usually defined by the time until a certain decrease of the initial luminance for a constant current is reached. For example, the terminology LT70 describes the time after which the actual luminance reaches 70 % of the initial value under constant current conditions.

In the previous chapter, an approach for efficiency analysis of state-of-the-art single-colored OLEDs was illustrated. An efficiency enhancement would directly follow in a strong increase of the lifetime of the devices, due to lower electrical energy consumption [79,127–129]. However, the physical background of device degradation during electrical operation is not yet fully understood.

Hence, the following sections will investigate the influence of electrical aging on the excited states lifetime of the emitting molecules and on the efficiency of the emitting system in standard and state-of-the-art OLEDs. These findings will be supplemented with an analysis of the electrical characteristics of the devices during the electrical aging process via IVL measurements and impedance spectroscopy. The electrical aging of the devices was established by an accelerated degradation protocol by applying a high constant current density and a simultaneous detection of the required voltage and the emitted luminance of the OLEDs. After each degradation step, IVL characteristics,

time-resolved luminescence measurements and impedance spectroscopy have been performed in order to analyze the processes behind the decrease of the emitted light.

First, an approach of a modified sample structure exhibiting very short RC-times will be presented. Short RC-times of the devices allows for time-resolved electroluminescence measurements, that are much closer to the actual driving conditions during the electrical aging than photoluminescence spectroscopy. This consideration directly follows from the excitation process. While the emission layer is excited with an almost constant exciton density over the whole layer thickness by an optical laser pulse, it is possible that the emission zone is very narrow and located at one of the interfaces of the emission layer during electrical operation. Therewith higher exciton densities within a few nanometers can follow. Thus, the electrical excitation in time-resolved luminescence measurements would yield more realistic results than optical excitation.

Second, the presented modified sample structure is used to analyze the influence of electrical aging on the excited states lifetime of the previously presented emitting system Ir(ppy)₃:CBP including an estimation of the changes of the radiative quantum efficiency of the emitting system.

Finally, the comprehensive efficiency analysis presented in the previous chapter will be established to analyze the changes of the radiative quantum efficiency of the red phosphorescent emitting system during the electrical aging by time-resolved photoluminescence spectroscopy and external quantum efficiency measurements, allowing for a detailed analysis of the influence of the degradation process on the four factors determining the external quantum efficiency of OLEDs.

6.1 OLED devices with short RC-times

Time-resolved electroluminescence spectroscopy is only feasible if the used samples exhibit RC-times that are shorter than the excited states lifetimes of the emitting system under investigation. The decay times of most of the common used phosphorescent emitters are in the range of a few microseconds. Hence, devices with RC-times in the range of some ten nanoseconds are required to achieve straightforward analysis of the excited states lifetimes of the emitting species after excitation with an electrical pulse. A second crucial point is the edge steepness of the applied voltage pulse. However, the used wave function generator, mentioned in chapter three, exhibits an acceptable edge steepness of only a few nanoseconds (see Fig 6.1 a)) and therefore the RC-time of the used device structure is the limiting factor for time-resolved electroluminescence spectroscopy. Unfortunately, the RC-times of the standard structure of OLEDs fabricated at University

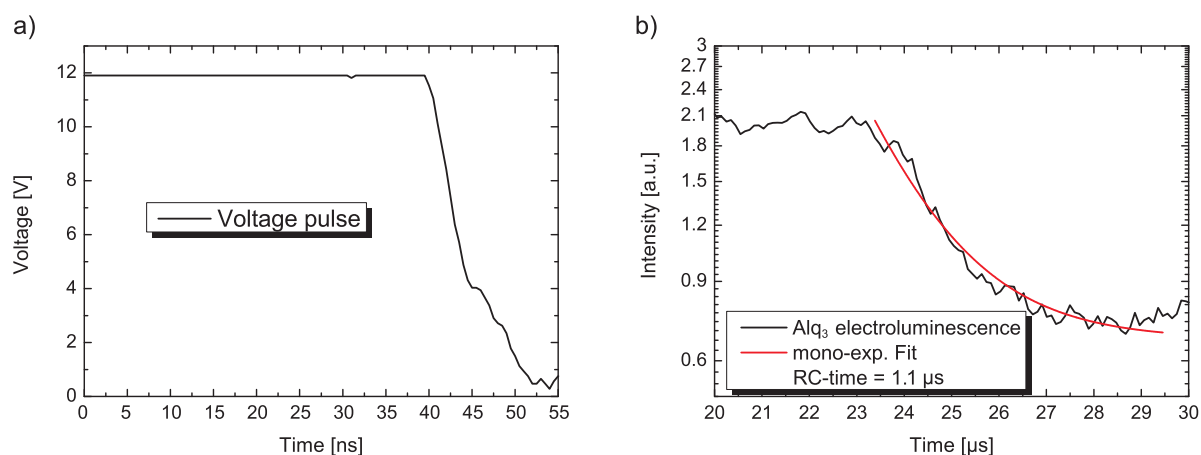


Figure 6.1: a) Illustration of the voltage pulse steepness measured by a digital storage oscilloscope. b) Time-resolved electroluminescence signal of an OLED exhibiting Alq₃ as emitting molecule. The RC-time of the device was determined to 1.1 μs.

of Augsburg exhibit a too long RC-time of about 1.1 μs, as can be seen from Fig. 6.1 b) showing a time-resolved electroluminescence experiment of a device exhibiting Alq₃ as emitting material with an excited states lifetime of ≈ 15 nanoseconds (see chapter 4). Hence, the standard OLED structure was modified to achieve short RC-times. The results of this section have been achieved in cooperation with Christoph Mieskes in the scope of his Bachelor thesis [130].

The RC-time of OLEDs is mainly determined by the capacitance (C) of the pixel and the resistance (R) of the electric line. The resistance of the electric line is affected by the conductivity of the ITO anode of the device and is therefore relatively fixed for the OLEDs under investigation. Thus, the capacitance of the OLED structure has to be reduced to achieve shorter RC-times. The easiest accessible factor determining the capacitance of the OLED pixels is their area. Unfortunately, the area that contributes to the capacitance of the pixels is not only the active, light-emitting one, but also parasitic stray capacitances, caused by in-plane conductivity of the unstructured organic layers. Especially the commonly used hole injection layer (PEDOT:PSS) exhibits a very high in-plane conductivity resulting in an enormous parasitic stray capacitance of the OLED pixels. Hence, the spincoated polymer PEDOT:PSS was replaced by a new hole injection material (HATCN). HATCN is a small molecule that allows for a patterned structure of the HIL and the following organic materials by thermal evaporation (see Fig. 3.1) and therewith a strong reduction of the capacitance of the fabricated OLED pixels. Strictly speaking, HATCN is not acting as classical HIL and exhibits a hole generating character, as already explained in sec. 3.1. In addition the size of the active

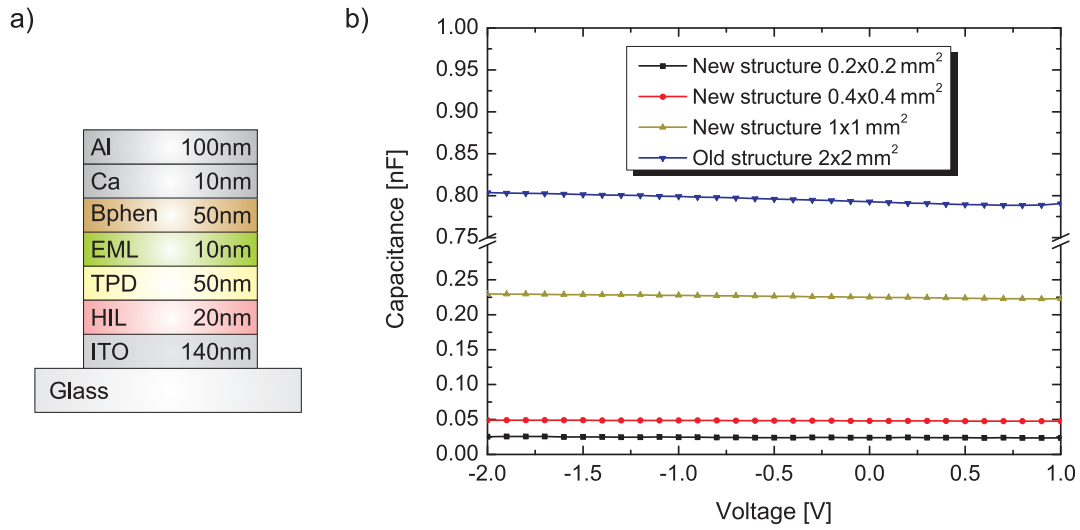


Figure 6.2: a) Sample structure of the devices under investigation. PEDOT:PSS and HATCN are used as HIL for the old and the new sample structure, respectively. The EML consists of Ir(ppy)₃ doped with 6 wt% in a CBP matrix. b) Measurements of the geometric capacitance of different OLED structures via impedance spectroscopy. Blue line: OLED with unstructured organic layers using PEDOT:PSS as HIL resulting in an active pixel area of 2x2 mm². Black, red and ocher lines represent the new OLED structures with an active pixel area of 0.2x0.2 mm², 0.4x0.4 mm² and 1x1 mm², respectively. All measurements have been performed at a fixed frequency of 133 Hz.

area has been reduced from 4 mm² to 1 mm². In order to prove this concept of a reduced capacitance, measurements of the geometric capacitance of pixels fabricated with the new and the old structure, exhibiting different active areas, have been performed via impedance spectroscopy. The sample structure and the results are presented in Fig. 6.2.

It can clearly be seen, that the measured geometric capacitance of the pixels exhibiting patterned organic layers (new structure) is drastically reduced compared to the pixels using an unstructured HIL (old structure). Please note that the difference between both sample types are the exchange of the HIL, the active area size and the patterned organic layers. The thicknesses of all organic layers are identical in both structures. Hence, the decrease of the capacitance and therewith simultaneously of the RC-time of the devices is caused by the new sample structure. Although the new sample structure with an active area of 1x1 mm² does not show the lowest geometric capacitance of the measured pixels, they have been chosen to be the future structure due to much higher light output and lower resistance of the ITO anode bars. With measurements of the capacitance and the sheet resistance of the OLED extracted from IVL characteristics it is possible to estimate the theoretical RC-time of this device structure to $\tau_{RC} = 66.7$ ns [130].

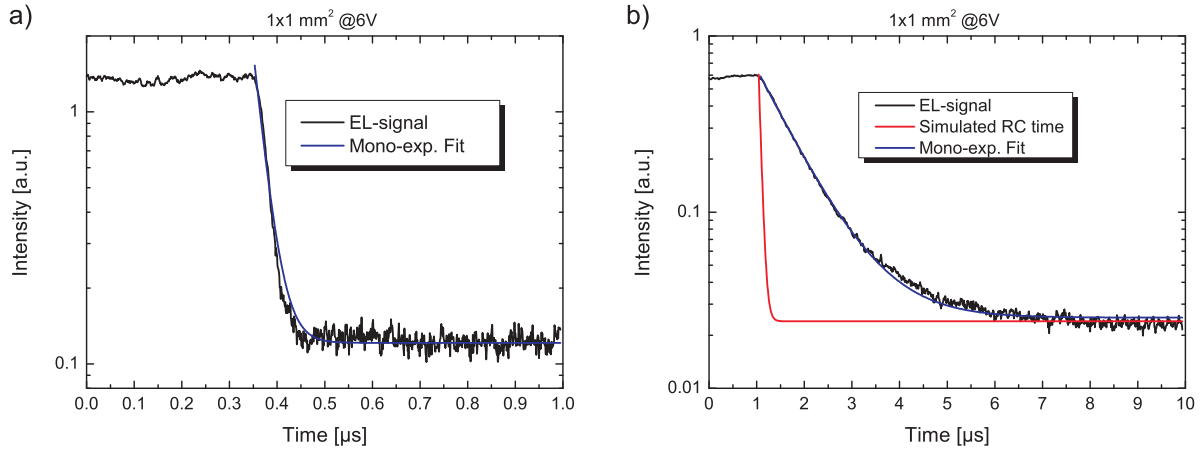


Figure 6.3: Time-resolved electroluminescence measurements using the new sample structure exhibiting a) a fluorescent and b) a phosphorescent emitting system. Due to the very short excited states lifetime of the fluorescent emitting species, the fitted decay time gives directly the RC-time of the devices. In b) additionally to the measured and the fitted electroluminescence decay of Ir(ppy)₃ molecules, the theoretically calculated behavior for the sample is plotted as a red line. Sample structure: ITO/HATCN/TPD/EML/Bphen/Ca/Al.

However, in order to give evidence that the new sample structure is appropriate for time-resolved electroluminescence spectroscopy, two devices with a fluorescent emitter, exhibiting an excited states lifetime of only a few nanoseconds, and the standard stack with Ir(ppy)₃:CBP as emitting system, with a decay time in the range of 750 ns, have been fabricated and measured with the streak camera system. Figure 6.3 a) illustrates the time-dependent electroluminescence signal of the device with the fluorescent emitting system, resulting in a fitted decay time of the signal of 59.4 ns. This corresponds to the RC-time of the device, due to the much shorter excited states lifetime of the fluorescent molecules [130]. This experimentally determined value is in very good agreement with the theoretically calculated one. Additionally, the measured electroluminescence decay curve of the sample with the green phosphorescent emitter Ir(ppy)₃ is shown in Fig. 6.3 b). The excited states lifetime of the emitting molecules was determined to 800 ns using the new OLED structure and electrical square wave pulses with an amplitude of 6 V, which is in very good agreement with the expected decay time. The slight difference can be a consequence of a deviation of the actual ETL thickness from the planned one.

This gives clear evidence, that the developed new OLED structure is appropriate for time-resolved electroluminescence spectroscopy, and is the basis for the analysis of degradation effects presented in the following section.

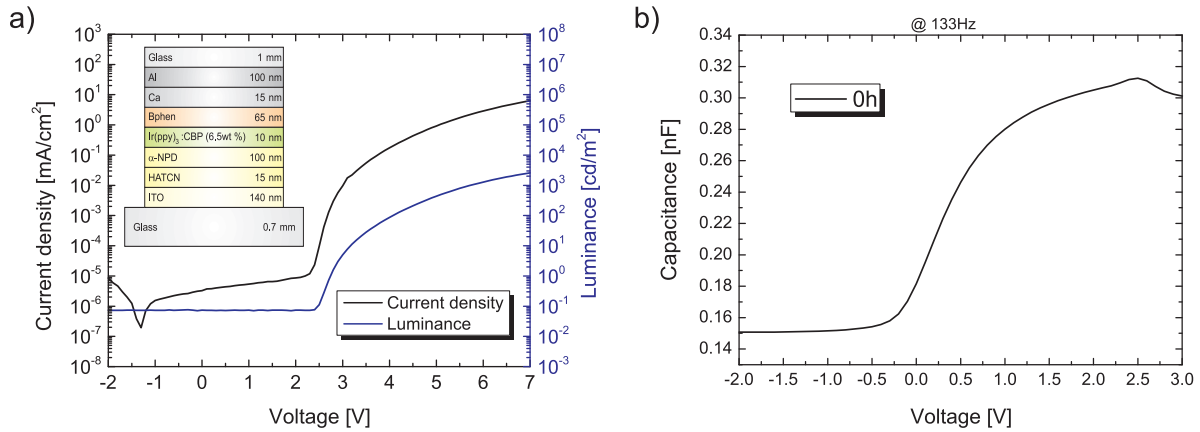


Figure 6.4: a) IVL characteristics of the device under investigation (sample structure shown as inset). Light output starts at 2.5 V. b) CV measurement of the device under investigation. Holes are already injected into the α -NPD layer due to an interface charge caused by the polar ETL. Electrons are injected for voltages over 2.5 V and hence light output occurs.

6.2 Degradation analysis for low latency devices

In the previous section the development of a new device structure exhibiting low RC-times was presented. Hence, this approach can be used to analyze degradation processes in organic light-emitting diodes in terms of time-resolved electroluminescence spectroscopy, which is expected to give more precise results than photoluminescence experiments. Therefore, the device already presented in Fig. 3.1 a) (see also Fig. 6.4 a)) was fabricated with the low latency structure. After the electrical characterization via IVL measurements and impedance spectroscopy the device was electrically aged under constant current conditions. After each degradation step of usually one hour, IVL and impedance measurements have been performed to detect changes in the electrical behavior. Additionally, time-resolved electroluminescence spectroscopy have been accomplished to investigate the influence of the current induced aging process on the excited states lifetime of the used emitting guest/host system.

Figure 6.4 demonstrates the electrical characterization of the pristine device before starting the aging protocol. The current through the device shows a typical behavior of an OLED and the built-in voltage is about 2.5 V. Simultaneously, light output from the active pixel occurs at the same voltage. A current density of 1 mA/cm² is reached at about 4.8 V resulting in a luminance of about 4,000 cd/m². The CV measurement shown in Fig. 6.4 b) was performed for a fixed frequency of 133 Hz. It can clearly be seen, that charge carrier injection already occurs for voltages over -0.25 V. Further investigations

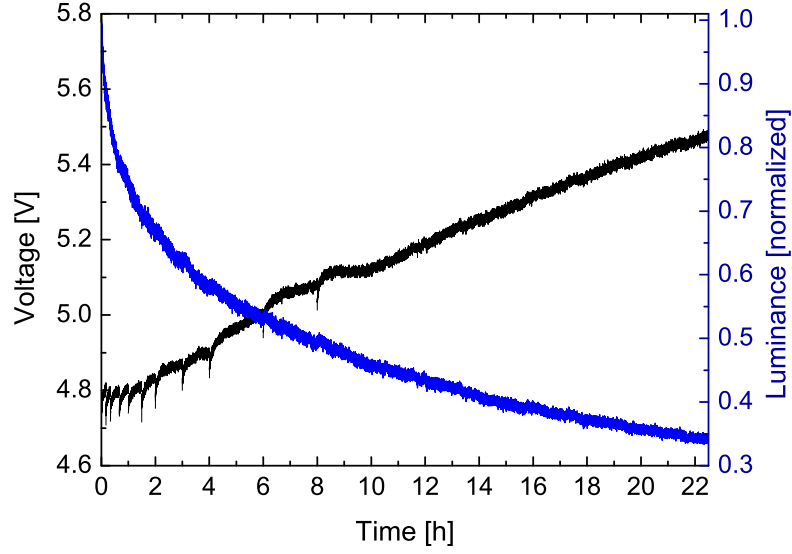


Figure 6.5: Degradation of the device under investigation at a constant current density of 1 mA/cm^2 . LT35 is reached after 20 hours aging time. The required voltage for 1 mA/cm^2 increases from 4.8 V to 5.5 V during this period. Sample structure: ITO/HATCN/ α -NPD/Ir(ppy)₃:CBP/Bphen/Ca/Al.

have demonstrated that holes are already injected into the HTL at -0.25 V and accumulate at the α -NPD/CBP interface compensating an interface charge caused by the polar Bphen layer [131, 132]. However, a detailed analysis of impedance spectroscopy, including CF measurements, performed for this type of samples is beyond the scope of this thesis and will not be discussed in detail in the following. Nevertheless, Fig. 6.4 b) illustrates that the electrons are injected into the device at a voltage of about 2.5 V what is in good agreement with the measured IVL-characteristics. Additionally, time-resolved electroluminescence spectroscopy has been performed for the pristine state, as will be discussed later in detail.

Figure 6.5 illustrates the accelerated degradation behavior of the device under constant current density conditions of 1 mA/cm^2 . This current density results in an initial value of the luminance of about $4,000 \text{ cd/m}^2$. As can clearly be seen, the required voltage increases from 4.8 V to 5.5 V during 20 hours of electrical aging, while simultaneously the luminance decreases to only 35 % of the initial value (LT35). The decrease of the luminance with degradation time shows a stretched-exponential decay behavior, that gives a hint for the creation of non-radiative recombination centers in the emission layer [133] and the reduction of the luminance is fastest in the first few hours of electrical aging.

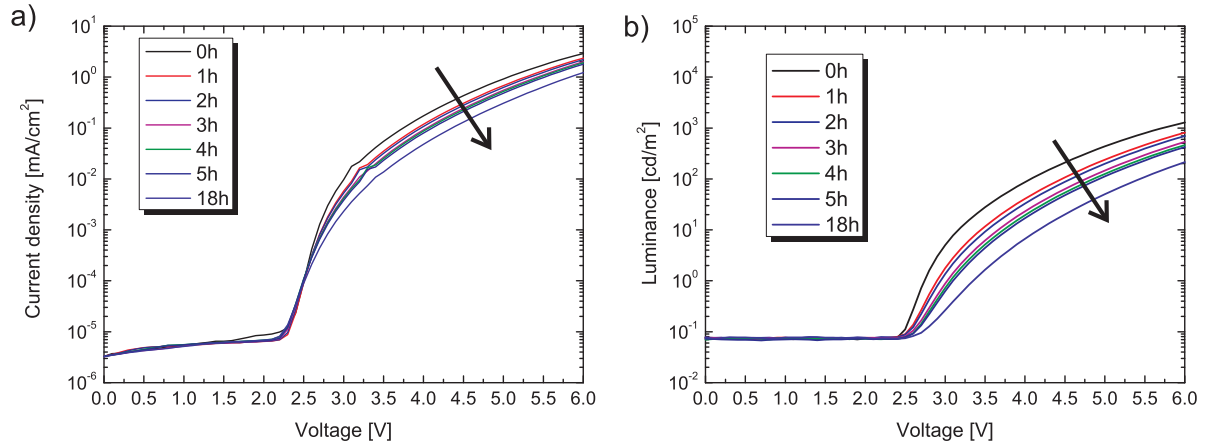


Figure 6.6: Degradation induced changes of the IVL-characteristics of the device under investigation. a) Current density and b) luminance as a function of the applied voltage for different aging times. The different onset voltages of the current and the luminance are caused by a slightly lower sensitivity of the photodiode compared to the current detector. Sample structure: ITO/HATCN/ α -NPD/Ir(ppy)₃:CBP/Bphen/Ca/Al.

The small spikes, more pronounced for the required voltage than for the measured luminance, result from slight recovery effects and temperature decrease of the sample during the investigation of the IVL characteristics, the impedance spectroscopy and the time-resolved electroluminescence measurements that all together take about one hour between two degradation steps. It should be noted, that additional degradation due to the electrical characterization and time-resolved electroluminescence spectroscopy was not detectable.

Figure 6.6 illustrates the changes in the IVL characteristics due to electrical aging. It is obvious, that the continuous decrease in the current density for a fixed voltage over the aging time is less pronounced than for the corresponding luminance, which is in good agreement with other publications [134]. This gives a hint, that the present degradation effects are influencing the electrical characteristics in a different way than the creation of light and/or different effects are responsible for the decrease of both values. Moreover, it is obvious that the built-in voltage of the current shows only slight differences for the different degradation steps, while the voltage, at which light output is detectable, is shifted by about 0.5 V from the pristine state to the value after 18 hours of electrical aging. However, to analyze the electrical changes in more detail, CV measurements are presented in Fig. 6.7. As a first result from the impedance spectroscopy, it can clearly be seen, that the geometrical capacitance of the device is not changing during electrical degradation. Though, a strong shift in the transition voltage of holes is obvious.

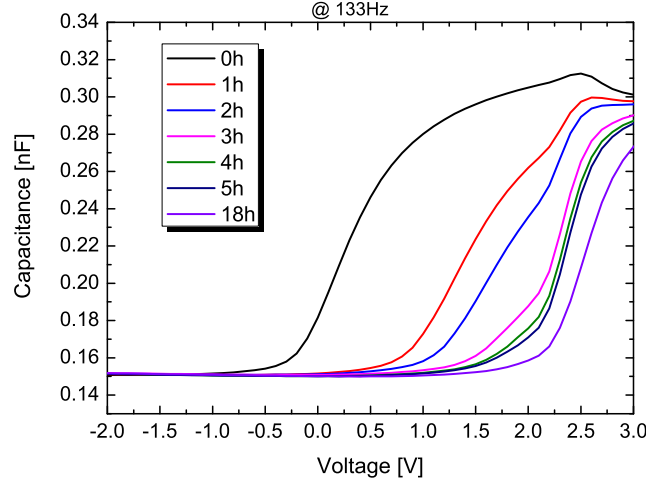


Figure 6.7: CV-measurements for different degradation steps. The frequency was fixed to 133 Hz for all measurements. The transition voltage shifts to higher voltages during electrical aging. Sample structure: ITO/HATCN/ α -NPD/Ir(ppy)₃:CBP/Bphen/Ca/Al.

While the injection of holes already occurs at -0.25 V in the pristine case, the injection begins at about 1.5 V after 5 hours of electrical aging. The shift is more pronounced for the first degradation step than for the following ones. That gives a hint, that the electrical changes are arising mainly in the first hours of degradation and correspond to the fast initial decrease of luminance at the beginning of the aging protocol. One possible explanation for these changes is a creation of charged trap states in the emission layer, that are compensating the interface charge due to the polar Bphen layer, which is in accordance with previously published results [82, 83]. Additionally, these trap states can act as quenchers, which is in good agreement with the stretched-exponential decay of the luminance during electrical aging.

In order to analyze the creation of non-radiative recombination centers due to the electrical aging of the devices [135, 136], time-resolved electroluminescence spectroscopy was performed. Figure 6.8 illustrates the results of two exemplary investigations of the excited states lifetimes of the emitting molecules of the device under investigation for the pristine state and after 18 hours of electrical aging. The excited states lifetime is drastically reduced due to the degradation process from 0.81 μ s to 0.61 μ s, respectively. This gives strong evidence for the formation of non-radiative recombination centers in the emission layer of the device.

To clarify that the changes of the decay times of the emitting species are not affected due to changes of the emission zone position inside the OLED cavity, the emission spec-

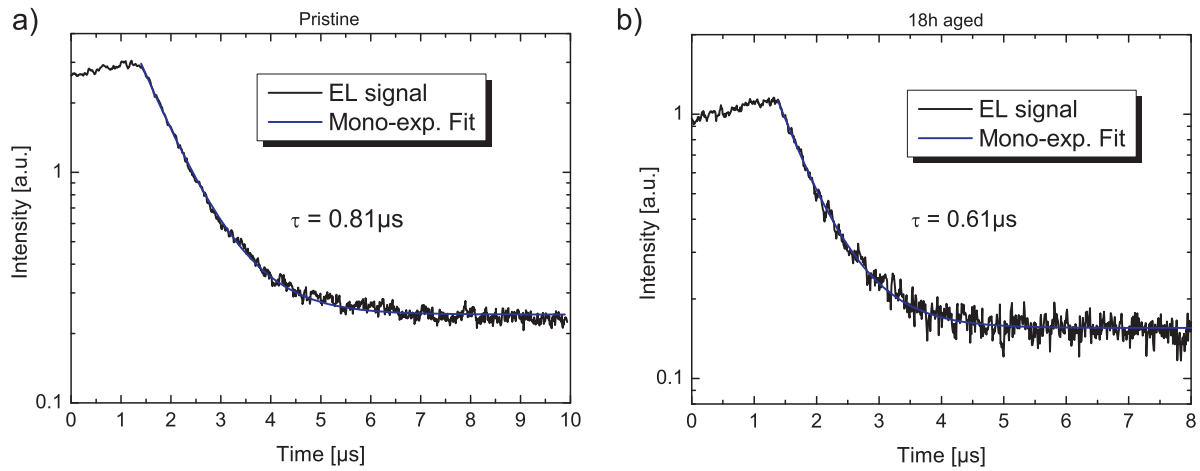


Figure 6.8: Exemplary investigation of the excited states lifetimes measured via time-resolved electroluminescence spectroscopy a) for the pristine state of the device under investigation and b) after 18 hours of electrical aging. The decay time is drastically reduced due to the degradation process. Sample structure: ITO/HATCN/ α -NPD/Ir(ppy)₃:CBP/Bphen/Ca/Al.

tra of the pristine device and after electrical aging was extracted from the time-resolved electroluminescence spectroscopy used for the excited states lifetime determination. As it is obvious from Fig. 6.9 a) no changes in the shape of the emission spectrum is detectable, resulting in a fixed position of the emission zone inside the OLED cavity for all degradation steps.

Figure 6.9 b) demonstrates the degradation induced decrease of the excited states lifetime as a function of the relative reduction in luminance. The measured data points can be reproduced by a linear function. This gives clear evidence that the main part of the loss in luminance due to electrical aging is caused by the reduction of the radiative quantum efficiency of the used emitting guest/host system. This is directly following from Eq. 2.10 if the radiative rate of the emissive species is assumed to remain constant and is not influenced by the degradation process:

$$\text{Luminance} \propto \text{EQE} \propto q_{\text{eff}} \equiv \Gamma_r \cdot F \cdot \tau. \quad (6.1)$$

This means, that the main drop in luminance during electrical aging is caused by a reduction of the RQE of the emitting system. Other factors determining the external quantum efficiency of an OLED, particularly the charge carrier balance, remain constant although strong changes of the electrical characteristics have been observed. However, the exact mechanism behind the increase of the non-radiative rate of the emitting species is not known until now and should be part of further investigations.

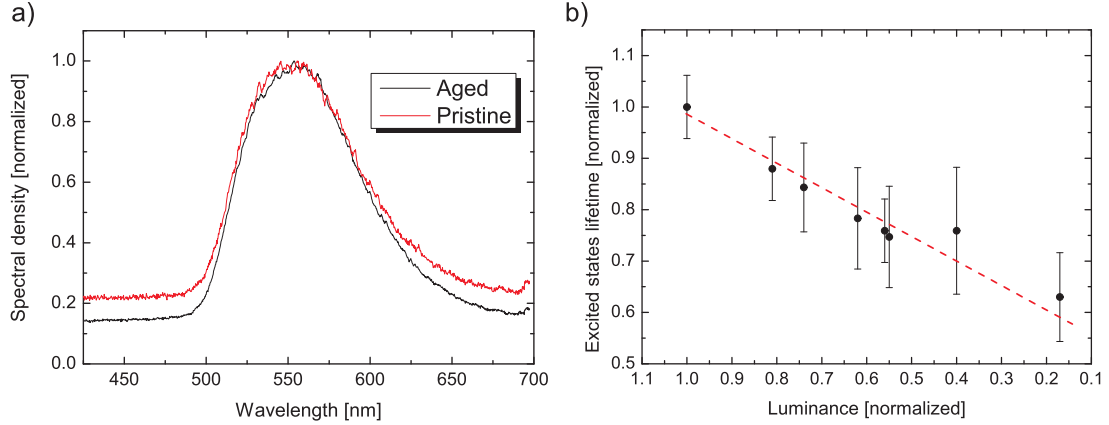


Figure 6.9: a) Comparison of the electroluminescence emission spectra of the device for the pristine state and after degradation. No changes of the shape of the spectrum are detectable. (The offset of the pristine device is caused by a different signal to background ratio for both measurements.) b) Changes of the excited states lifetimes extracted from time-resolved electroluminescence spectroscopy as a function of the luminance. A linear behavior can explain the measured data points. Sample structure: ITO/HATCN/ α -NPD/Ir(ppy)₃:CBP/Bphen/Ca/Al.

6.3 Efficiency analysis after degradation of OLEDs

In order to analyze degradation effects of state-of-the-art OLEDs in detail, the comprehensive efficiency analysis, previously presented in sec. 5.4.3, has been additionally performed after an accelerated degradation process of all nine samples exhibiting different ETL thicknesses and the red emitting system Ir(MDQ)₂(acac): α -NPD (see Fig. 3.3 c) and Fig. 5.21).

The accelerated electrical aging process was accomplished by driving the OLEDs at a high current density of 62.5 mA/cm² resulting in a luminance of about 15,000 cd/m² for the device with an ETL thickness of 249 nm (second cavity maximum) for direct emission. Figure 6.10 illustrates an exemplary degradation curve and the IVL-characteristics of this device. After 65 hours of degradation LT60 is reached and the decrease of the luminance shows a stretched-exponential decay, which is an evidence for the creation of non-radiative recombination centers in the emission layer [133]. However, the required voltage is changing only little over the whole aging period. The small oscillation of the voltage is caused by problems with climatisation of the room during device degradation. However, the main result of a slight voltage increase, while the luminance drop is well pronounced, is in good agreement with other publications [134]. Moreover, the IV characteristics of the device shows only little changes due to the degradation process.

Although the variation of the ETL thickness results in a strong variation of the cavity

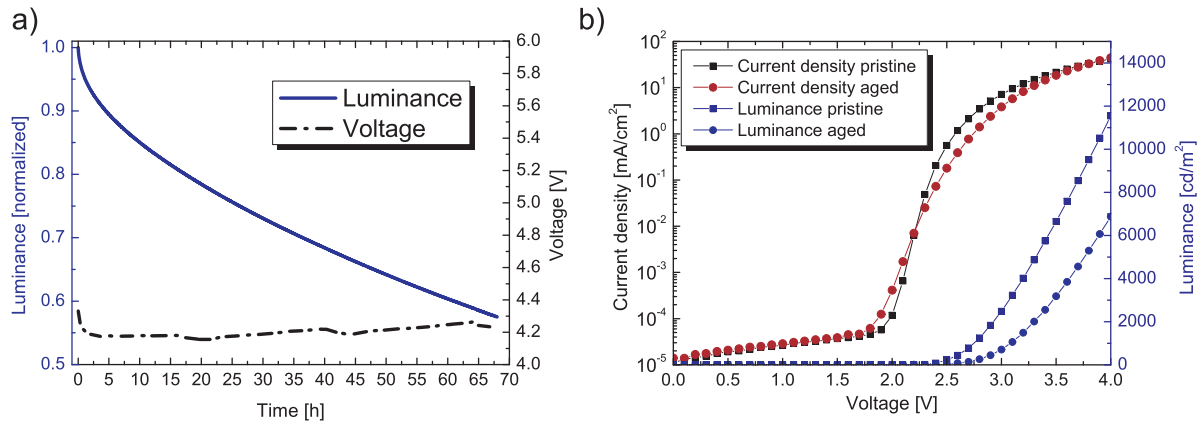


Figure 6.10: a) Exemplary degradation curve of the device exhibiting an ETL thickness of 249 nm resulting in an initial luminance of about 15,000 cd/m^2 at the aging current of 62.5 mA/cm^2 . The stretched exponential decay of the luminance results in LT60 after 65 hours degradation time, while the required voltage changes only little. b) IVL-characteristics for the pristine state and after degradation of the same sample. The current characteristics shows only slight changes, while the reduction of the corresponding luminance is well pronounced. Graphics taken from Ref. [125]. Sample structure: ITO/HTL/EBL/EML ($\text{Ir}(\text{MDQ})_2(\text{acac})$): α -NPD)/HBL/ETL/Ag.

length of the devices and therewith different coupling to the optical modes and effective radiative quantum efficiencies of the emitting system, all nine devices show a comparable degradation behavior for the same aging conditions yielding LT60 after 65 hours electrical stressing time. It should be noted, that LT60 corresponds to each initial value of direct emission for the different samples, by means of reduction by the same factor during the degradation time. Hence, although the external quantum efficiency values for the samples differ considerably, the identical relative decrease of their initial values is the basis that allows for performing an efficiency analysis as has been performed already for the pristine devices.

Figure 6.11 demonstrates the determination of the RQE of the emitting system of the samples before and after the degradation process via electrically driven EQE measurements at a low current density of 1 mA/cm^2 to avoid current induced quenching processes. The measured EQE values for the pristine state can be reproduced by the fit in a reasonable way yielding an RQE of $68 \pm 2\%$ for an assumed charge carrier balance of unity, which is in good agreement with the previously presented results. However, the determination of the radiative quantum efficiency of the aged devices leads to a changed RQE of the emitting system of $40 \pm 2\%$, while the charge carrier balance seems to remain constant during the aging process, because it was assumed to be unity in the

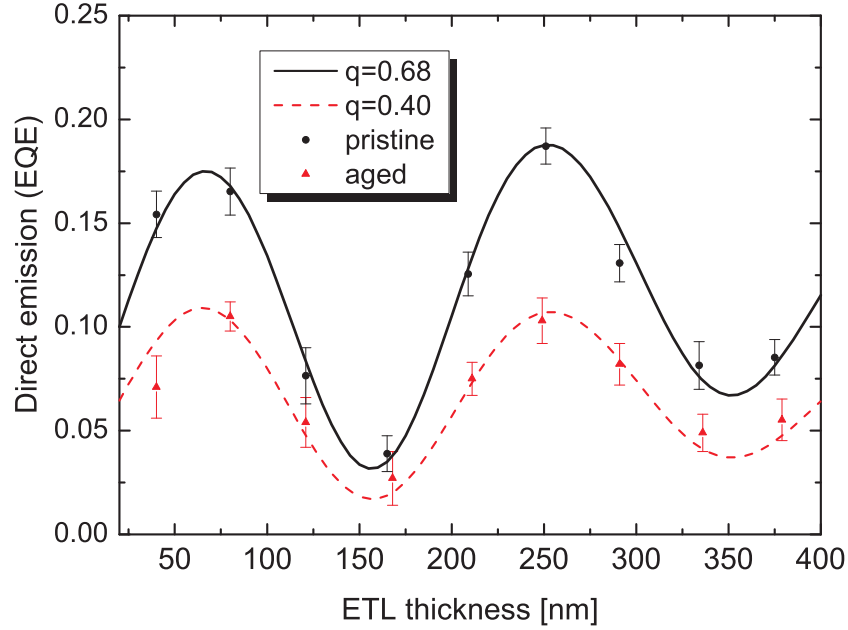


Figure 6.11: RQE determination via electrically driven external quantum efficiency measurements at a current density of 1 mA/cm^2 for the pristine state (black) and after degradation (red) of the samples to LT60. Fitting the measured data results in an RQE of the emitting system of 68 % and 40 % for the pristine state and after degradation, respectively. Graphic taken from Ref. [125]. Sample structure: ITO/HTL/EBL/EML ($\text{Ir}(\text{MDQ})_2(\text{acac})\text{:}\alpha\text{-NPD}$)/HBL/ETL/Ag.

fitting procedure. Indeed, this reduction in the RQE can exclusively explain the whole luminance drop over the degradation. This gives strong evidence, that only the RQE of the emitting system is significantly influenced by this accelerated degradation process and other factors determining the external quantum efficiency of these devices are not modified.

However, to exclude a possible rearrangement of the emissive dipole moments of the emitting species resulting in a changed outcoupling and Purcell factor for the devices, angular and polarization dependent measurements in the cavity minimum at an ETL thickness of 168 nm, where this type of measurement is very sensitive for emitter orientation [55], have been performed after degradation. Indeed, no changes of the assumed orientation of the emissive transition dipole moments are detectable. Furthermore, performing this measurement gives additional access to the position of the emission zone, that is unmodified despite the aging process, too.

In order to verify these results and to investigate the underlying degradation process in more detail, time-resolved photoluminescence spectroscopy was performed for all nine

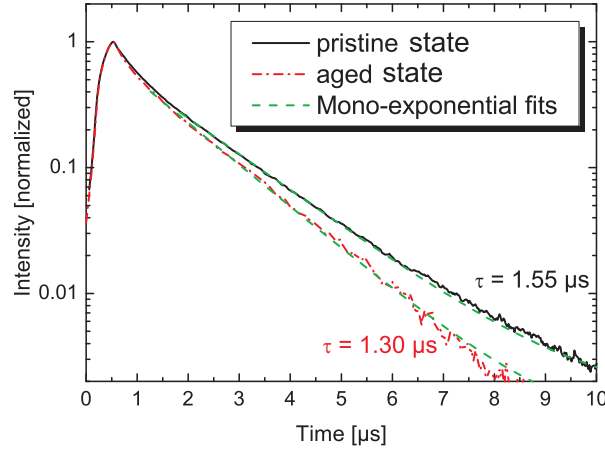


Figure 6.12: Decay of the photoluminescence signal for the device exhibiting an ETL thickness of 168 nm for the pristine state (black solid line) and after degradation (red dashed line). Green dashed lines represent mono-exponential fits of the curves resulting in a reduction of the excited states lifetime due to the aging process. Graphic taken from Ref. [125]. Sample structure: ITO/HTL/EBL/EML ($\text{Ir}(\text{MDQ})_2(\text{acac})\text{:}\alpha\text{-NPD}$)/HBL/ETL/Ag.

devices before and after degradation. A common explanation of the drop of the luminance during electrical degradation is an increase of the non-radiative rate of the emitting species and a corresponding decrease of the excited states lifetime with the assumption of an unchanged radiative rate [135,136]. Figure 6.12 shows the exemplary time-resolved photoluminescence decay of the device exhibiting an ETL thickness of 168 nm, for the pristine state and after degradation. Both signals have been normalized for an identification of the changes in the decay times determined by mono-exponential fits for both measurements. It can clearly be seen that the excited states lifetime is reduced by the electrical aging resulting in $1.55\text{ }\mu\text{s}$ and $1.30\text{ }\mu\text{s}$ for the pristine device and after degradation, respectively. This gives evidence, that the non-radiative rate of the emitting species is drastically increased during degradation.

To analyze this behavior in more detail, the RQE of the emitting system has been additionally investigated via the changes of the excited states lifetimes before and after degradation to LT60. The measured data point sets and best fits are presented in Fig. 6.13. The analysis of the pristine state results in the same values of the radiative quantum efficiency and intrinsic excited states lifetime of the emitting system as presented before. Furthermore, the determination of both values was performed after degradation, too, yielding a q' of $40 \pm 2\%$ and a τ'_0 of $1.23 \pm 0.03\text{ }\mu\text{s}$. It should be noted, that the RQE and the intrinsic excited states lifetime of the degraded emitting guest/host system is denoted with a $'$ for clarity. These results are in good agreement

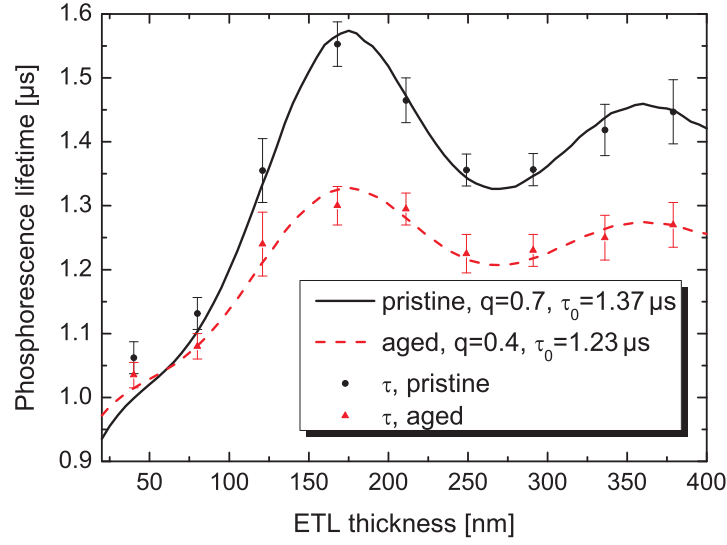


Figure 6.13: Determination of the RQE of the emitting system before (black dots) and after (red triangles) degradation. The lines represent best fits of both measured data point sets resulting in RQEs of $70 \pm 5\%$ and $40 \pm 5\%$ for the pristine state and after aging, respectively. Additionally, a clear reduction of the intrinsic lifetime by the degradation process is detectable. Graphic taken from Ref. [125]. Sample structure: ITO/HTL/EBL/EML ($\text{Ir}(\text{MDQ})_2(\text{acac})$): α -NPD)/HBL/ETL/Ag.

with the investigation of the EQE of the devices. Accordingly, the drop of the luminance due to the electrical degradation process can be exclusively explained by a decrease of the RQE of the emitting system from $q = 0.7$ to $q' = 0.4$.

Moreover, with the investigated changes of the intrinsic excited states lifetime and the radiative quantum efficiency it is possible to calculate both, the radiative and the non-radiative rate of the emitting system before and after the degradation process in order to prove the assumption of an unchanged radiative rate and an increased non-radiative rate, as mentioned before. Solving Eq. 2.11 and 2.12 with the determined values results in $\Gamma_r = 5.1 \cdot 10^5 \text{ s}^{-1}$ and $\Gamma_{nr} = 2.2 \cdot 10^5 \text{ s}^{-1}$ for the pristine devices. In the same way for τ'_0 and q' after degradation one obtains a radiative decay rate Γ'_r of $3.3 \cdot 10^5 \text{ s}^{-1}$ and a non-radiative decay rate Γ'_{nr} of $4.8 \cdot 10^5 \text{ s}^{-1}$ [125]. As expected from other experiments [135, 136] the non-radiative rate increases due to the aging. However, it is evident that also the radiative rate is modified and decreases upon device degradation.

Hence, the common assumption of an unmodified (intrinsic) radiative rate due to electrical degradation is not valid for the devices under investigation and should be considered for future degradation experiments.

It is known that the matrix material α -NPD is not very stable under current flow and reacts chemically with its surrounding. These chemical reactions can create deep charge carrier traps and non-radiative recombination centers [134,137–139]. One possible effect is that the electronic levels of these degradation products are shifted in energy with respect to the pristine molecules, which can influence the Dexter transfer rate (k_D) from the host to the phosphorescent guest. If the energy transfer rate to $\text{Ir}(\text{MDQ})_2(\text{acac})$ is drastically reduced due to degradation of the α -NPD molecules and the decay rates of the emitting species is of the same magnitude as the degraded transfer rate k_D^* , one would expect a bi-exponential decay behavior of the measured phosphorescence with an initial slow increase of the signal. As can be seen from Fig. 6.12 this is actually not the case. Therefore, two other effects that can explain the changes of the non-radiative and the radiative decay rate of the emitting molecules are assumed. As mentioned before, the non-radiative decay rate of the emitting molecules can be enhanced by both, the degraded matrix molecules themselves, acting as emission quenchers, and charge carriers that are trapped on the matrix resulting in possible triplet-polaron-quenching. In addition, the degraded matrix molecules can exhibit a different permittivity with respect to their intact counterparts. This could explain the changed radiative decay rate of the embedded dye molecules due to changes in the optical environment [125].

Figure 6.14 illustrates exemplary capacitance-voltage measurements at a fixed frequency of 133 Hz of the device exhibiting an ETL thickness of 249 nm for the pristine state and after degradation. It can clearly be seen, that the geometrical capacitance of the device is reduced by the aging process. This gives evidence, that the assumption of a changed relative permittivity of the matrix could be the responsible process for the changed radiative rate of the emitting species.

Besides matrix effects, the emitter molecule $\text{Ir}(\text{MDQ})_2(\text{acac})$ can react chemically by replacement of its ligands [125]. These products (deactivated sites) are normally not able to emit light. This behavior is known for many Ir-complexes such as $\text{Ir}(\text{ppy})_3$ or $\text{Ir}(\text{ppy})_2(\text{acac})$ [140], which have similar structures as $\text{Ir}(\text{MDQ})_2(\text{acac})$ [128], and from devices using Alq_3 as emitting system [141]. Energy transfer from the host as well as from intact emitting molecules to these degradation products can increase the non-radiative decay rate and reduce the Dexter transfer rate by creating a competing transfer channel or by simply depleting the guest/host system from intact dye molecules. In addition, the degradation of emitters might lead to rather subtle molecular changes only. In that case, one could expect a similar emission spectrum of these degradation products exhibiting different decay times. This could be another reason for the changed radiative and non-radiative decay rates.

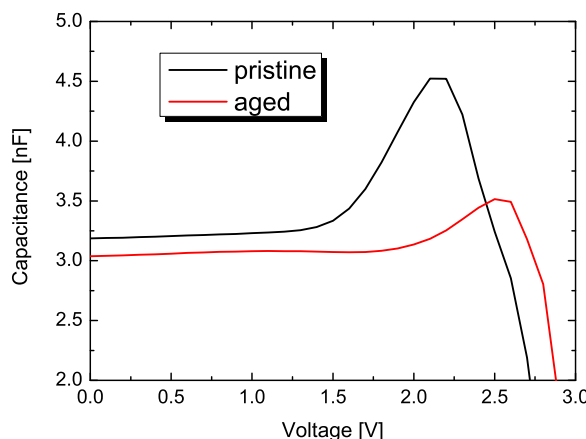


Figure 6.14: Capacitance-voltage measurements at a fixed frequency of 133 Hz of the device exhibiting an ETL thickness of 249 nm for the pristine state and after degradation. The geometrical capacitance is reduced due to the aging process. Sample structure: ITO/HTL/EBL/EML (Ir(MDQ)₂(acac): α -NPD)/HBL/ETL/Ag.

6.4 Conclusions and further work

In this chapter, innovative approaches for the analysis of degradation effects have been presented.

First, the development and the evaluation of a new sample structure exhibiting short RC-times has been pointed out.

Second, these new low latency devices have been used for analyzing the influence of electrical aging on the excited states lifetime of the emitting guest/host system. By using the low RC-time devices it was possible to perform time-resolved electroluminescence spectroscopy even for the emitting system under investigation exhibiting a relatively short excited states lifetime of less than one microsecond. Therewith, the investigation of the degradation induced changes of the excited states lifetime and the corresponding radiative quantum efficiency of the emitting system is much closer to the situation of the electrical aging process, because a photoluminescence experiment would probe the whole emission layer and not only a narrow emission zone that is often the case in organic light-emitting diodes. Hence, the electrically pulsed time-resolved experiment promises considerably more precise results.

The accelerated degradation process under constant current conditions results in a fast decrease of the luminance and a corresponding increase in the required voltage. Impedance spectroscopy demonstrated the electrical changes of the device, namely a

shift of the transition voltage of holes to higher voltages and slight changes in the built-in voltage. One possible explanation for these changes is the creation of charged trap states in the emission layer, that are compensating the interface charge due to the polar Bphen layer, which is in accordance with previously published results [82, 83]. Additionally, these trap states can act as quenchers, which is in good agreement with the stretched-exponential decay of the luminance during electrical aging.

However, the main focus was lying on degradation induced changes of the photo-physical properties of the emitting system. Time-resolved electroluminescence spectroscopy detected a subsequent decrease of the excited states lifetime of the emitting species with electrical aging time. Moreover, the relative decrease of the excited states lifetime is directly correlated with the relative drop of the luminance during the degradation process. Thus, the common assumption of an unchanged radiative rate and a degradation induced increase of the non-radiative rate, that was supposed due to the stretched exponential decrease of the luminance with degradation time, was certified for the emitting system used in the device under investigation.

Finally, the previously presented comprehensive efficiency analysis for a set of state-of-the-art OLEDs with varying electron transport layer thickness was performed before and after an accelerated degradation process reaching LT60 after 65 hours of electrical aging. Due to a very similar degradation behavior independently from the cavity strength at the emitter position achieved by the variation of the ETL layer thickness, it was possible to perform the mentioned efficiency analysis via both electrically driven external quantum efficiency and time-resolved photoluminescence measurements.

The analysis of the EQE measurements for the direct emission before and after the degradation process results in a decrease by a factor of 1.6 from 70 % to 40 %, respectively. Thus, the whole luminance drop during the degradation process can be explained by a reduction of the radiative quantum efficiency of the emitting guest host system under investigation. The charge carrier balance seems to remain constant due to the very good agreement of measurement and simulation for the pristine state and after degradation, although small changes in the electrical characteristics have been detected via IVL measurements and impedance spectroscopy. Additionally, a degradation induced rearrangement of the emissive dipole moments of the emitting molecules and therewith changes of the outcoupling factor of the devices can be excluded due to angular and polarization dependent measurements performed in the cavity minimum of the devices at an ETL thickness of 168 nm for the pristine state and after degradation.

Furthermore, the determination of the radiative quantum efficiency of the emitting system under investigation via time-resolved photoluminescence measurements results

in nearly the same values before and after degradation compared to the EQE investigations. Thus, the intrinsic excited states lifetime of the emitting system was subsequently reduced with electrical aging time. From calculations of the radiative and the non-radiative rate for the pristine state and after the degradation process it follows, that for the emitting system under investigation, the assumption of an unchanged radiative rate during electrical degradation is definitely wrong. This is in clear contrast to the results achieved for the emitting system $\text{Ir(ppy)}_3\text{:CBP}$. Hence, an a priori predication about possible changes of the radiative rate of an emitting system during electrical operation is not possible and must to be investigated separately for each OLED stack. However, in the case of $\text{Ir(MDQ)}_2(\text{acac})\text{:}\alpha\text{-NPD}$, not only the non-radiative rate of the emitting species is increased but also the radiative rate is remarkably reduced. Hence, two different degradation processes are assumed to explain the changes in both rates, namely an aging of the matrix material and of the emitting molecules. With impedance spectroscopy it was possible to detect a clear decrease of the geometrical capacitance of the device exhibiting an ETL thickness of 249 nm. This can be the result of a changed dielectric constant of the matrix material, that influences the radiative rate of the emitting species. Furthermore, the creation of (charged) trap states of the matrix molecules can yield an increase of the non-radiative rate of the emitting molecules. Moreover, the emitting species can chemically react under replacement of its ligands, typically resulting in deactivated sites, that are not able to emit light. Nevertheless, a detailed analysis of the reason for changes in both rates and of the degradation products is missing and should be the focus of further research.

Future investigations, should aim at a combination of both presented methods. With a comprehensive efficiency analysis of the emitting system in state-of-the-art OLEDs via time-resolved electroluminescence spectroscopy, additional investigations of emission zone modifications should be possible. Hence, a more detailed analysis would follow. Moreover, the aim is to understand degradation processes in multi-colored OLED systems, especially for white emission. In white OLEDs, the degradation behavior of the different emission layers is typically different, resulting in strong emission spectrum changes during electrical aging. Additionally, energy transfer processes between different emitting molecules can be modified. Analyzing these processes could result in a deeper understanding of degradation processes even in multi-colored OLEDs.

First degradation experiments for red-green-blue hybrid OLEDs have been performed. Current dependent emission spectra comparisons have been the basis to investigate the charge traveling through the three-layered emission system of the device already presented in Fig. 3.3 d). With these extracted results it was possible to create a model

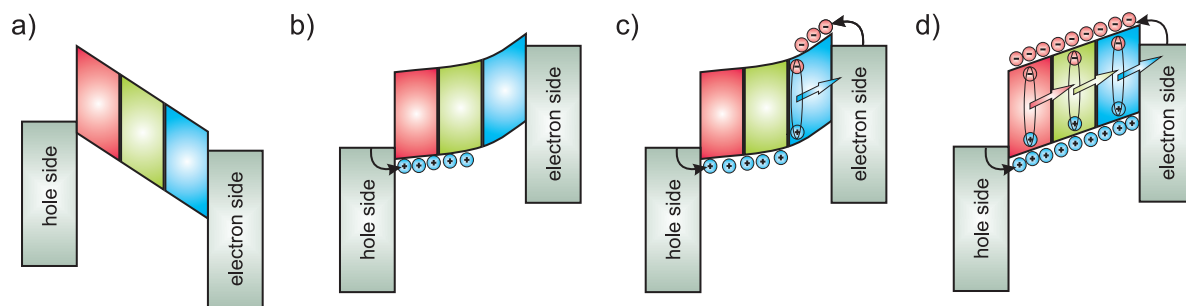


Figure 6.15: Schematic model of charge carrier injection and traveling in the RGB unit of a white state-of-the-art OLED. a) Reverse bias conditions, no charges are injected. b) Holes are injected first into the RGB-unit and are traveling towards the electron side for voltages higher than the transition voltage. c) Holes accumulate at the interface between the blue emission layer and the electron side (e.g. a HBL). At the built-in voltage electron injection into the blue emission layer starts. Blue light is emitted. d) For higher voltages than the built-in voltage, the three emission layers are completely flooded by both charge carrier types and white emission is detectable.

system presented in Fig. 6.15. Therewith, it was found that with increasing voltage holes are injected first into the RGB unit of the device and travel to the electron side until accumulation at the interface between the blue emission layer and the hole blocking layer (electron side) takes place. If the built-in voltage is reached, electrons are injected into the blue unit resulting in blue emission. If the voltage is subsequently increased the whole emission unit is flooded by both charge carrier types and white emission is detectable.

In order to analyze which of the emission species degrades first, an accelerated electrical aging protocol under constant current conditions was performed, reaching LT70 after about 150 h. After the degradation process electrical characterization was achieved by impedance spectroscopy (not shown). Additionally, the emission spectrum before and after degradation was detected (see Fig. 6.16), resulting in a relative decrease of the red emission. Therefore, a faster degradation process is assumed for the red emitting system than for the green and the blue one. The next steps to go, are performing a comprehensive efficiency analysis including energy transfer mechanisms, for a set of white OLED stacks with varying ETL thickness, before and after degradation. The accomplishment of these investigations can result in a deep understanding of degradation processes in multi-colored OLED structures, that would lead to an improvement in long-term stability in terms of electrical degradation.

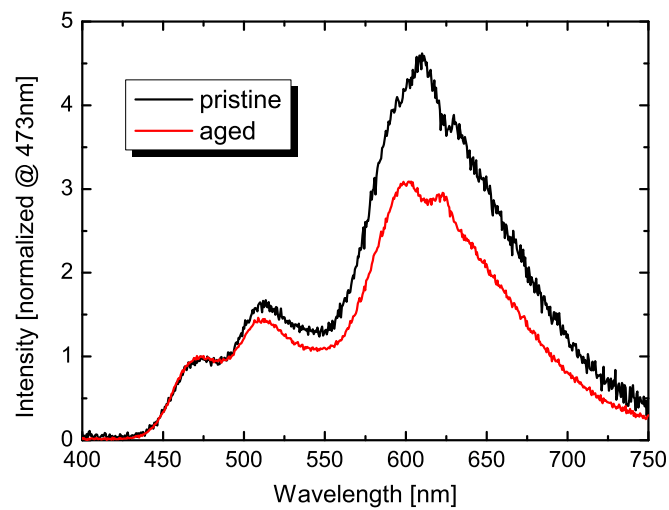


Figure 6.16: Emission spectra of the white OLED under investigation before and after degradation to LT70. Emission spectra are normalized to the value of 473 nm for the sake of a better comparison. From this it follows, that the red emitting system is degrading faster than the other two.

CHAPTER 7

SUMMARY

Organic light-emitting diodes are promising new light sources for both general lighting and display technologies. Although first commercial products are already available, the efficiency and the long-term stability during electrical operation are not really satisfying, yet. Thus, there is still much room for improvement of both factors influencing future applications based on OLEDs.

The motivation of this thesis was the better understanding of the photo-physical processes inside complex OLED structures. Especially the influence of cavity effects on the efficiency of the devices and a detailed analysis of energy dissipation to the optical modes of an OLED was in the focus of the first part, resulting in a comprehensive efficiency analysis of state-of-the-art devices.

Additionally, the degradation induced changes of the photo-physical properties of the emitting molecules have been less investigated in the past. Hence, the second part of this thesis deals with this topic because a better understanding of degradation effects, especially their influence on the emitting guest/host systems, can lead to an enormous increase of lifetimes in terms of long-term stability and a deeper physical understanding. However, the external quantum efficiency of organic light-emitting diodes is determined by four different factors, namely the charge carrier balance, the radiative exciton fraction, the effective radiative quantum efficiency of the emitting system and the outcoupling factor of the device. The first factor is mainly influenced by electrical properties of the used organic layers such as charge carrier mobility and injection barriers between them. The radiative exciton fraction is caused by quantum mechanical selection rules and is unity for phosphorescent emitting systems, while it can be significantly less for

fluorescent emitters. However, only the determination of all four factors of the EQE would lead to a consistent comprehensive efficiency analysis of state-of-the-art OLEDs, which was one aim of this thesis.

Therefore, the main focus was on developing and evaluating an approach to determine the radiative quantum efficiency of an emitting guest/host system inside a complex OLED structure, because measurements of isolated thin films in integrating spheres can lead to a wrong estimation of this important factor. Thus, a method based on a subsequent variation of the cavity strength, mainly formed by the typically used metallic cathode of an OLED, at the position of the emission zone was investigated by using simplified structures. Thereby, changes of the cavity strength were achieved by a variation of the distance of the emission layer to a highly reflecting silver layer which was obtained by a variable optical spacer thickness between both layers. Therewith, the interference effects and the power dissipation between the different optical modes of this system are changed, which is known as Purcell effect. Thus, the radiative rate of the emitting molecules is modified while the non-radiative rate remains unchanged. The corresponding excited states lifetime of the emitting molecules inside the cavity is hence changed with the optical spacer thickness. Using time-resolved photoluminescence spectroscopy and comparing the extracted excited states lifetimes to numerical simulations leads to a determination of the radiative quantum efficiency of the emitting system under investigation. This approach was proven for two different optical spacer materials, SiO_2 and LiF , for the phosphorescent emitting molecules Ir-SC4 and Ir(ppy)_3 doped with some weight percent in PMMA and CBP, respectively.

The electrical characteristics of a complete OLED should not be changed by the method for the RQE determination. Hence, this approach was first not applicable, due to changes of the charge carrier balance for heavily differing layer thicknesses. Therefore, another technique was investigated to change the cavity strength at the emission zone inside complete OLED stacks, using a second reflective layer on top of the typically transparent anode. Thus, a thin silver layer with variable thickness was introduced to a conventional stack. Analyzing changes of the excited states lifetime of the emitting system inside the microcavity with a variable strength at the emitter position and comparing these results with numerical simulations allows for a determination of both, the intrinsic excited states lifetime and the RQE of the emitting system under investigation. Unfortunately, the electrical characteristics of these microcavity OLEDs have been unstable and hence, another approach was needed.

The solution of this problem of changing the optical properties but not the electrical characteristics was the introduction of well established conductivity doped transport

layers, for which the resistance of the layer is independent of its actual thickness. Hence, the first approach changing the distance of the emitting system to a highly reflective metal layer was implemented by a subsequent variation of the electron transporting layer thickness that is typically sandwiched between the metallic cathode and the emission layer of an OLED. Therewith, it was possible to determine the RQE of several emitting systems with two different experiments, namely external quantum efficiency measurements with and without outcoupling enhancements based on ray optics and time-resolved photoluminescence spectroscopy. Comparing these results with numerical simulations allows for a determination of the RQE of the emitting system under investigation. Thus, it was possible to investigate the influence of the matrix material on the radiative quantum efficiency of the emitting molecule Ir(ppy)₃, leading to changes of the RQE between 40 % and 85 % depending on the used matrix material. Therewith, the common assumption of a very high RQE close to unity for phosphorescent emitting systems is not a priori correct.

Additionally, the current density induced changes of the RQE of the emitting system was analyzed. One result was that the effective RQE of the emitting system is drastically reduced even for moderate and especially for high current densities as they are used in applications. Hence, the OLED cavity has to be optimized in terms of layer thickness adjustment for the planned current density, because typically the first cavity maximum is the favorable one if the effective RQE of the emitting system is lower than 50 %, while the second one should be used for higher effective RQE values. It should be noted, that this assumption is only true if an application for direct emission is considered, while the first maximum is always the more efficient one, if macroscopic outcoupling structures are used.

Thereafter, the influence of non-isotropic orientation of the transition dipole moments of the emitting molecules on the efficiency analysis of state-of-the-art OLEDs was pointed out. Recent studies have shown the existence of both, fluorescent and phosphorescent oriented emitting molecules, even if they are doped in amorphous matrices. This feature was not taken into account in a proper way for many years. Non-isotropic emitter orientation is influencing both the outcoupling factor of the devices and the effective RQE of the emitting systems due to different coupling to the optical modes and different interference conditions inside the OLED cavity, respectively. Hence, the emitting system Ir(MDQ)₂(acac): α -NPD exhibiting predominantly horizontally oriented emitting dipole moments with respect to the device surface was analyzed in detail. The possible mistakes in efficiency analysis assuming an isotropic emitter orientation, if a (prevailing) horizontal alignment is present, has been highlighted and the potential efficiency

increase due to the introduction of totally horizontally oriented emissive dipole moments was calculated resulting in remarkably high EQE values of 38 % and 74 %, that can be reached for direct emission and if macroscopic outcoupling structures giving access to the substrate modes of the devices are used, respectively. Therewith, two of the four factors determining the EQE of an OLED have been analyzed in detail (the charge carrier balance was included into the numerical simulations). Furthermore, the current dependent increase of the non-radiative rate of the emitting system was analyzed and was identified to exhibit a logarithmic behavior for the emitting system under investigation.

In order to analyze the influence of changes of the radiative exciton fraction on the efficiency analysis of state-of-the-art OLEDs, the phosphorescent emitting system was replaced by a fluorescent, nearly completely horizontally oriented emitting system exhibiting thermally activated delayed fluorescence. TADF can recycle normally lost triplet excitons by a thermally activated spin flip and therewith delayed fluorescence. Hence, the analysis via electrically driven external quantum efficiency measurements is complicated by this effect. Therefore, the RQE of the emitting system was first investigated by changes of the excited states lifetime of the prompt fluorescence with a subsequent variation of the emitter/cathode distance. With this result it was thereafter possible to estimate a lower limit for the radiative exciton fraction (for the assumption of an ideal charge carrier balance) of 36 % instead of the typically used value of 25 % owing to simple spin statistics. Thus, three factors responsible for the EQE of an OLED have been determined in a reasonable and reliable way for the first time in literature for an emitting system showing non-isotropic emitter orientation and changes of its radiative exciton fraction due to thermally activated delayed fluorescence.

The second part of this thesis focused on the analysis of degradation processes by means of electrical aging of the devices. First, a new sample structure exhibiting low latency has been developed. With this new structure it was possible to investigate the changes of the excited states lifetime during electrical aging via time-resolved electroluminescence spectroscopy. This method is much closer to the real processes arising during electrical operation than probing the whole emission layer with an optical excitation. The decrease of the excited states lifetime of the emitting system can be correlated with the drop in luminance during electrical aging. Thus, the common assumption of an unchanged radiative rate while the non-radiative rate is increased due to electrical operation was proved for the emitting system Ir(ppy)₃:CBP. Additionally, the decrease of the excited states lifetime and the corresponding radiative quantum efficiency of the emitting system was identified to be the main reason for the drop in luminance although

strong changes in the electrical characteristics have been detectable via IVL measurements and impedance spectroscopy.

Finally, the presented approach for efficiency analysis of OLEDs was then used for analyzing degradation effects in state-of-the-art devices. Therefore, the efficiency analysis was performed via EQE measurements and time-resolved photoluminescence spectroscopy before and after an accelerated degradation process. Therewith, it was possible to explain the electrical aging induced drop in luminance exclusively by a decrease of the radiative quantum efficiency of the emitting system ($\text{Ir}(\text{MDQ})_2(\text{acac}):\alpha\text{-NPD}$), while the other three factors determining the external quantum efficiency of an OLED remained constant. It should be noted, that a possible deviation of the emitter orientation due to the electrical degradation has been included in the analysis. Additionally, the calculation of the radiative and the non-radiative rates of the emitting species for the pristine state and after degradation disproved the assumption of an unchanged radiative rate due to electrical aging. It was found, that both rates are modified by the degradation process, the non-radiative rate is increased while the radiative rate is reduced. In order to explain these unexpected changes, two different degradation mechanisms, namely aging of the matrix and of the emitting molecules, have been assumed and partial evidence has been achieved.

Thus, the comprehensive efficiency analysis of monochrome OLEDs was accomplished and should now be extended to multi-colored stacks. Furthermore, first basic results have been achieved in terms of investigations of degradation processes and the presented innovative approach should be deepened for future research.

In conclusion, this work presented a comprehensive efficiency analysis for state-of-the-art OLEDs, that should be a basic method for analyzing the factors determining the external quantum efficiency of a device. In particular, the achieved results are very important for device optimization in terms of layer thickness adjustment. Moreover, degradation processes have been investigated and changes of the radiative and the non-radiative rates of the emitting molecules have been detected. This can be the basis for a deeper understanding of degradation processes in organic light-emitting diodes.

APPENDIX

Materials

α -NPD	N,N'-bis(naphthalen-1-yl)-N,N'-bis(phenyl)benzidine
Alq ₃	Tris-(8-hydroxyquinoline)aluminum
Bphen	4,7-diphenyl-1,10-phenanthroline
CBP	4,4'-N,N'-dicarbazole-biphenyl
Ir(MDQ) ₂ (acac)	Bis(2-methyldibenzo[f,h]quinoxaline)(acetylacetonate)- iridium(III)
Ir(ppy) ₃	Tris(2-phenylpyridine) iridium
Ir-SC4	fac-tris[2-(2-pyridinyl-kN) (5-(3,4-bis(2-methylpropyloxy)phenyl)phenyl)-kC]-iridium(III)
ITO	Indium-tin oxide
LR	Lumogen Red
PEDOT/PSS	Poly(3,4-ethylenedioxythiophene) poly(styrenesulfonate)
PMMA	Polymethylmethacrylate
TPD	N,N'-diphenyl-N,N'-bis(3-methylphenyl)-1,1'-biphenyl-4,4'- diamine

General abbreviations

a. u.	Arbitrary units
AFM	Atomic force microscopy
cw	Continuous wave
EBL	Electron blocking layer
EIL	Electron injection layer
EL	Electroluminescence
EML	Emission layer
EQE	External (electroluminescence) quantum efficiency
ETL	Electron transport layer
HBL	Hole blocking layer
HIL	Hole injection layer
HOMO	Highest occupied molecular orbital
HTL	Hole transport layer
ISC	Intersystem crossing
LED	Light-emitting diode
LUMO	Lowest unoccupied molecular orbital
OLED	Organic light-emitting diode
OOS	OSRAM Opto Semiconductors
OPVC	Organic photovoltaic cell
PL	Photoluminescence
SPP	Surface plasmon polariton
SPQ	Singlet-polaron-quenching
SSA	Singlet-singlet-annihilation
TADF	Thermally activated delayed fluorescence
TE	Transverse electric
TM	Transverse magnetic
TPQ	Triplet-polaron-quenching
TTA	Triplet-triplet-annihilation
UNA	University of Augsburg
WG	Waveguided mode

BIBLIOGRAPHY

- [1] M. POPE, H. P. KALLMANN, and P. MAGNANTE, *J. Chem. Phys.* **38**, 2042 (1963).
- [2] C. W. TANG and S. A. VANSLYKE, *Appl. Phys. Lett.* **51**, 913 (1987).
- [3] J. H. BURROUGHS, D. D. C. BRADLEY, A. R. BROWN, R. N. MARKS, K. MACKAY, R. H. FRIEND, P. L. BURNS, and A. B. HOLMES, *Nature* **347**, 539 (1990).
- [4] <http://www.oled-info.com/osram-developed-87-lmw-white-oled-panel-production-soon>.
- [5] R. CHENG, *Wall Street Journal* **September 6th** (2010).
- [6] Y.-S. TYAN, *J. Photon. Energy* **1**, 011009 (2011).
- [7] Commercial white OLEDs are offered since 2010 e.g. by Osram and Philips (see www.osram.com and www.lighting.philips.com).
- [8] <http://oled.beleuchtung-mit-led.de/osram-orbeos-oled-panel>.
- [9] <http://www.golem.de/1011/79187.html>.
- [10] <http://www.oled-info.com/files/images/OSRAM-OLED-rollercoaster.jpg>.
- [11] M. SCHWOERER and H. WOLF, *Organic Molecular Solids*, Wiley-VCH, Berlin, 2006.
- [12] W. BRÜTTING, editor, *Physics of Organic Semiconductors*, Wiley-VCH, Berlin, 2012.

-
- [13] D. Y. KONDAKOV, T. D. PAWLIK, T. K. HATWAR, and J. P. SPINDLER, *J. Appl. Phys.* **106**, 124510 (2009).
- [14] H. YERSIN, editor, *Highly Efficient OLEDs with Phosphorescent Materials*, Wiley-VCH, Berlin, 2007.
- [15] M. PFEIFFER, K. LEO, X. ZHOU, J. S. HUANG, M. HOFMANN, A. WERNER, and J. BLOCHWITZ-NIMOTH, *Org. Electron.* **4**, 89 (2003).
- [16] H. BÄSSLER, *phys. stat. sol. (b)* **175**, 15 (1993).
- [17] R. P. HEMENGER, *J. Chem. Phys.* **67**, 262 (1977).
- [18] A. RUINI, M. J. CALDAS, G. BUSSI, and E. MOLINARI, *Phys. Rev. Lett.* **88**, 206403 (2002).
- [19] Y. WU, B. HU, and J. HOWE, *J. Appl. Phys.* **98**, 103510 (2005).
- [20] M. POPE and C. E. SWENBERG, *Electronic processes in organic crystals and polymers*, Oxford University Press, 1999.
- [21] A. DODABALAPUR, *Sol. Stat. Comm.* **102**, 259 (1997).
- [22] W. L. BARNES, *J. Mod. Opt.* **45**, 661 (1998).
- [23] H. BECKER, S. E. BURNS, and R. H. FRIEND, *Phys. Rev. B* **56**, 1893 (1997).
- [24] J. A. E. WASEY and W. L. BARNES, *J. Mod. Opt.* **47**, 725 (2000).
- [25] B. C. KRUMMACHER, S. NOWY, J. FRISCHEISEN, M. KLEIN, and W. BRÜTTING, *Org. Electron.* **10**, 478 (2009).
- [26] D. S. SETZ, T. D. SCHMIDT, M. FLÄMMICH, S. NOWY, J. FRISCHEISEN, B. C. KRUMMACHER, T. DOBBERTIN, K. HEUSER, D. MICHAELIS, N. DANZ, W. BRÜTTING, and A. WINNACKER, *J. Photon. Energy* **1**, 011006 (2011).
- [27] S. MLADENOVSKI, K. NEYTS, D. PAVICIC, A. WERNER, and C. ROTHE, *Opt. Express* **17**, 7562 (2009).
- [28] C. ADACHI, T. TSUTSUI, and S. SAITO, *Appl. Phys. Lett.* **57**, 531 (1990).
- [29] T. TSUTSUI, E. AMINAKA, C. P. LIN, and D. U. KIM, *Phil. Trans. Soc. A* **355**, 801 (1997).

- [30] C. ADACHI, M. A. BALDO, M. E. THOMPSON, and S. R. FORREST, *J. Appl. Phys.* **90**, 5048 (2001).
- [31] M. A. BALDO, D. F. O'BRIEN, Y. YOU, A. SHOUSTIKOV, S. SIBLEY, M. E. THOMPSON, and S. R. FORREST, *Nature* **395**, 151 (1998).
- [32] J. S. WILSON, A. S. DHOOT, A. J. A. B. SEELEY, M. S. KHAN, A. KOHLER, and R. H. FRIEND, *Nature* **413**, 828 (2001).
- [33] Y. SUN, N. C. GIEBINK, H. KANNO, B. MA, M. E. THOMPSON, and S. R. FORREST, *Nature* **440**, 908 (2006).
- [34] M. A. BALDO, D. F. O'BRIEN, M. E. THOMPSON, and S. R. FORREST, *Phys. Rev. B* **60**, 14422 (1999).
- [35] M. SEGAL, M. A. BALDO, R. J. HOLMES, S. R. FORREST, and Z. G. SOOS, *Phys. Rev. B* **68**, 075211 (2003).
- [36] Y. LUO and H. AZIZ, *Adv. Funct. Mater.* **20**, 1285 (2010).
- [37] D. YOKOYAMA, Y. PARK, B. KIM, S. KIM, Y.-J. PU, J. KIDO, and J. PARK, *Appl. Phys. Lett.* **99**, 123303 (2011).
- [38] Y.-J. PU, G. NAKATA, F. SATOH, H. SASABE, D. YOKOYAMA, and J. KIDO, *Adv. Mater.* **24**, 1765 (2012).
- [39] H. STERNLICHT, G. C. NIEMAN, and G. W. ROBINSON, *J. Chem. Phys.* **38**, 1326 (1963).
- [40] A. ENDO, K. SATO, K. YOSHIMURA, T. KAI, A. KAWADA, H. MIYAZAKI, and C. ADACHI, *Appl. Phys. Lett.* **98**, 083302 (2011).
- [41] K. GOUSHI, K. YOSHIDA, K. SATO, and C. ADACHI, *Nature Photon.* **6**, 253 (2012).
- [42] S. NOWY, B. C. KRUMMACHER, J. FRISCHEISEN, N. A. REINKE, and W. BRÜTTING, *J. Appl. Phys.* **104**, 123109 (2008).
- [43] E. PURCELL, *Phys. Rev.* **69**, 674 (1946).
- [44] K. A. NEYTS, *J. Opt. Soc. Am. A* **15**, 962 (1998).

-
- [45] X.-W. CHEN, W. C. H. CHOY, C. J. LIANG, P. K. A. WAI, and S. HE, *Appl. Phys. Lett.* **91**, 221112 (2007).
- [46] J. A. E. WASEY, A. SAFONOV, I. D. W. SAMUEL, and W. L. BARNES, *Phys. Rev. B* **64**, 205201 (2001).
- [47] N. C. GIEBINK, B. W. D. ANDRADE, M. S. WEAVER, P. B. MACKENZIE, J. J. BROWN, M. E. THOMPSON, and S. R. FORREST, *J. Appl. Phys.* **103**, 044509 (2008).
- [48] N. C. GIEBINK and S. R. FORREST, *Phys. Rev. B* **77**, 235215 (2008).
- [49] S. REINEKE, K. WALZER, and K. LEO, *Phys. Rev. B* **75**, 125328 (2007).
- [50] N. C. GREENHAM, R. H. FRIEND, and D. D. C. BRADLEY, *Adv. Mater.* **6**, 491 (1994).
- [51] L. SMITH, J. A. E. WASEY, I. D. W. SAMUEL, and W. L. BARNES, *Adv. Funct. Mater.* **15**, 1839 (2005).
- [52] S. NOWY, J. FRISCHEISEN, and W. BRÜTTING, *Proc. SPIE* **7415**, 74151C (2009).
- [53] T. D. SCHMIDT, M. FLÄMMICH, B. J. SCHOLZ, D. MICHAELIS, C. MAYR, N. DANZ, and W. BRÜTTING, *Proc. SPIE* **8435**, 843513 (2012).
- [54] J. A. E. WASEY, A. SAFONOV, I. D. W. SAMUEL, and W. L. BARNES, *Opt. Comm.* **183**, 109 (2000).
- [55] M. FLÄMMICH, M. C. GATHER, N. DANZ, D. MICHAELIS, A. H. BRÄUER, K. MEERHOLZ, and A. TÜNNERMANN, *Org. Electron.* **11**, 1039 (2010).
- [56] J. FRISCHEISEN, D. YOKOYAMA, C. ADACHI, and W. BRÜTTING, *Appl. Phys. Lett.* **96**, 073302 (2010).
- [57] J. FRISCHEISEN, D. YOKOYAMA, A. ENDO, C. ADACHI, and W. BRÜTTING, *Org. Electron.* **12**, 809 (2011).
- [58] M. FLÄMMICH, J. FRISCHEISEN, D. S. SETZ, D. MICHAELIS, B. C. KRUM-MACHER, T. D. SCHMIDT, W. BRÜTTING, and N. DANZ, *Org. Electron.* **12**, 1663 (2011).

- [59] T. D. SCHMIDT, D. S. SETZ, M. FLÄMMICH, J. FRISCHEISEN, D. MICHAELIS, B. C. KRUMMACHER, N. DANZ, and W. BRÜTTING, *Appl. Phys. Lett.* **99**, 163302 (2011).
- [60] N. A. REINKE, *Photophysikalische Prozesse und Lichtextraktion in organischen Leuchtdioden*, PhD thesis, University of Augsburg, 2008.
- [61] S. NOWY, *Understanding losses in OLEDs: optical device simulation and electrical characterization using impedance spectroscopy*, PhD thesis, University of Augsburg, 2010.
- [62] J. FRISCHEISEN, *Light extraction in organic light-emitting diodes*, PhD thesis, University of Augsburg, 2011.
- [63] B. J. SCHOLZ, PhD thesis, University of Augsburg, to be published, (private communications).
- [64] W. BRÜTTING, J. FRISCHEISEN, T. D. SCHMIDT, B. J. SCHOLZ, and C. MAYR, *phys. stat. sol. (a)* **210**, 44 (2012).
- [65] T. D. SCHMIDT, B. J. SCHOLZ, C. MAYR, and W. BRÜTTING, *IEEE*, in press (2013).
- [66] K. DREXHAGE, *Journal of Luminescence* **1**, 693 (1970).
- [67] K. DREXHAGE, *Prog. Opt.* **12**, 165 (1974).
- [68] R. R. CHANCE, A. PROCK, and R. SILBEY, *J. Chem. Phys.* **60**, 2744 (1974).
- [69] R. R. CHANCE, A. PROCK, and R. SILBEY, *Molecular Fluorescence and Energy Transfer Near Interfaces*, pp. 1–65, John Wiley & Sons, Inc., 2007.
- [70] W. LUKOSZ, *J. Opt. Soc. Am.* **71**, 744 (1981).
- [71] M. C. GATHER, M. FLÄMMICH, N. DANZ, D. MICHAELIS, and K. MEERHOLZ, *Appl. Phys. Lett.* **94**, 263301 (2009).
- [72] M. FURNO, R. MEERHEIM, S. HOFMANN, B. LÜSSEM, and K. LEO, *Phys. Rev. B* **85**, 115205 (2012).
- [73] Y. ZHOU, J. W. SHIM, C. FUENTES-HERNANDEZ, A. SHARMA, K. A. KNAUER, A. J. GIORDANO, S. R. MARDER, and B. KIPPELEN, *Phys. Chem. Chem. Phys.* **14**, 12014 (2012).

-
- [74] B. BRÖKER, *Electronic and structural properties of interfaces between electron donor & acceptor molecules and conductive electrodes*, PhD thesis, Humboldt-University Berlin, 2010.
- [75] D.-H. LEE, Y.-P. LIU, K.-H. LEE, H. CHAE, and S. M. CHO, *Org. Electron.* **11**, 427 (2010).
- [76] B. D. CHIN, Y. CHOI, H.-I. BAEK, and C. LEE, *Proc. SPIE* **7415**, 741510 (2009).
- [77] M. Y. CHAN, C. S. LEE, S. L. LAI, M. K. FUNG, F. L. WONG, H. Y. SUN, K. M. LAU, and S. T. LEE, *J. Appl. Phys.* **100**, 094506 (2006).
- [78] S. Y. KIM, J.-L. LEE, K.-B. KIM, and Y.-H. TAK, *J. Appl. Phys.* **95**, 2560 (2004).
- [79] C. DIEZ, T. C. G. REUSCH, E. LANG, T. DOBBERTIN, and W. BRÜTTING, *J. Appl. Phys.* **111**, 103107 (2012).
- [80] C. DIEZ, T. C. G. REUSCH, S. SEIDEL, and W. BRÜTTING, *J. Appl. Phys.* **111**, 113102 (2012).
- [81] W. BRÜTTING, S. BERLEB, and A. G. MÜCKL, *Org. Electron.* **2**, 1 (2001).
- [82] S. NOWY, W. REN, J. WAGNER, J. A. WEBER, and W. BRÜTTING, *Proc. SPIE* **7415**, 74150G (2009).
- [83] S. NOWY, W. REN, A. ELSCHNER, W. LÖVENICH, and W. BRÜTTING, *J. Appl. Phys.* **107**, 054501 (2010).
- [84] Y. NOGUCHI, Y. MIYAZAKI, Y. TANAKA, N. SATO, Y. NAKAYAMA, T. D. SCHMIDT, W. BRÜTTING, and H. ISHII, *J. Appl. Phys.* **111**, 114508 (2012).
- [85] J. FRISCHEISEN, B. SCHOLZ, B. J. ARNDT, T. D. SCHMIDT, R. GEHLHAAR, C. ADACHI, and W. BRÜTTING, *J. Photon. Energy* **1**, 011004 (2011).
- [86] S. A. MAIER, *Plasmonics: Fundamentals and Applications*, Springer, 2007.
- [87] H. RAETHER, *Surface Plasmons on Smooth and Rough Surfaces and on Gratings*, Springer, 1988.
- [88] R. P. VAN DUYNE, *Science* **306**, 985 (2004).

- [89] P. ANDREW and W. L. BARNES, *Science* **306**, 1002 (2004).
- [90] T. FÖRSTER, *Annalen der Physik* **437**, 55 (1948).
- [91] J. FENG, T. OKAMOTO, and S. NARAOKA, R. ANDI KAWATA, *Appl. Phys. Lett.* **93**, 051106 (2008).
- [92] S. WEHRMEISTER, Exzitonische Lebenszeitänderung in organischen Leuchtdioden induziert durch Triplett-Polaron-Quenching, Technical report, University of Augsburg, 2012.
- [93] S. FORREST, D. BRADLEY, and M. THOMPSON, *Advanced Materials* **15**, 1043 (2003).
- [94] J. C. DE MELLO, H. F. WITTMANN, and R. H. FRIEND, *Adv. Mater.* **9**, 230 (1997).
- [95] H. MATTOUSSI, H. ANDMURATA, C. D. MERRITT, Y. IIZUMI, J. KIDO, and Z. H. KAFABI, *J. Appl. Phys.* **86**, 2642 (1999).
- [96] N. DANZ, J. HEBER, A. BRÄUER, and R. KOWARSCHIK, *Phys. Rev. A* **66**, 063809 (2002).
- [97] T. BEIERLEIN, B. RUHSTALLER, D. GUNDLACH, H. RIEL, S. KARG, C. ROST, and W. RIESS, *Synth. Met.* **138**, 213 (2003).
- [98] J. WAGNER, M. GRUBER, A. HINDERHOFER, A. WILKE, B. BRÖKER, J. FRISCH, P. AMSALEM, A. VOLLMER, A. OPITZ, N. KOCH, F. SCHREIBER, and W. BRÜTTING, *Adv. Funct. Mater.* **20**, 4295 (2010).
- [99] A. C. DÜRR, N. KOCH, M. KELSCH, A. RÜHM, J. GHIJSEN, R. L. JOHNSON, J.-J. PIREAUX, J. SCHWARTZ, F. SCHREIBER, H. DOSCH, and A. KAHN, *Phys. Rev. B* **68**, 115428 (2003).
- [100] B. LEBSANFT, Bestimmung der Quanteneffizienz organischer Farbstoffe über ihre Lumineszenzlebensdauer, Diplomarbeit, University of Augsburg, 2010.
- [101] A. K. SHERIDAN, A. R. BUCKLEY, A. M. FOX, A. BACHER, D. D. C. BRADLEY, and I. D. W. SAMUEL, *J. Appl. Phys.* **92**, 6367 (2002).
- [102] C. ROTHE, S. KING, and A. P. MONKMAN, *Phys. Rev. B* **73**, 245208 (2006).

-
- [103] J. M. BRAUN, Messung der Lumineszenzlebensdauer von organischen Emittern auf Silberoberflächen mit LiF-Spacern unterschiedlicher Dicke, Bachelor Thesis, University of Augsburg, 2011.
- [104] T. WEHLUS, *Anorganisch-Organische Hybridsysteme als Funktionsstrukturen für die integrierte Optoelektronik*, PhD thesis, University of Augsburg, 2011.
- [105] M. A. BALDO, S. LAMANSKY, P. E. BURROWS, M. E. THOMPSON, and S. R. FORREST, *Appl. Phys. Lett.* **75**, 4 (1999).
- [106] M. A. BALDO and S. R. FORREST, *Phys. Rev. B* **62**, 10958 (2000).
- [107] W. HOLZER, A. PENZKOFER, and T. TSUBOI, *Chem. Phys.* **308**, 93 (2005).
- [108] W. FINKENZELLER and H. YERSIN, *Chem. Phys. Lett.* **377**, 299 (2003).
- [109] G. RAMOS-ORTIZ, Y. OKI, B. DOMERCQ, and B. KIPPELEN, *Phys. Chem. Chem. Phys.* **4**, 4109 (2002).
- [110] K. NEYTS, P. DE VISSCHERE, D. K. FORK, and G. B. ANDERSON, *J. Opt. Soc. Am. B* **17**, 114 (2000).
- [111] H. J. PENG, M. WONG, and H. S. KWOK, *SID Symposium Digest of Technical Papers* **34**, 516 (2003).
- [112] J. HUANG, M. PFEIFFER, A. WERNER, J. BLOCHWITZ, K. LEO, and S. LIU, *Appl. Phys. Lett.* **80**, 139 (2002).
- [113] M. PFEIFFER, S. FORREST, K. LEO, and M. THOMPSON, *Adv. Mater.* **14**, 1633 (2002).
- [114] C.-L. LIN, T.-Y. CHO, C.-H. CHANG, and C.-C. WU, *Appl. Phys. Lett.* **88**, 081114 (2006).
- [115] F. SO, B. KRUMMACHER, M. K. MATHAI, D. POPLAVSKY, S. A. CHOULIS, and V.-E. CHOONG, *J. Appl. Phys.* **102**, 091101 (2007).
- [116] J. MEI, M. S. BRADLEY, and V. BULOVIĆ, *Phys. Rev. B* **79**, 235205 (2009).
- [117] G. FORD and W. WEBER, *Phys. Rep.* **113**, 195 (1984).
- [118] E. JANSSON, B. MINAEV, S. SCHRADER, and H. ÅGREN, *Chem. Phys.* **333**, 157 (2007).

- [119] D. YOKOYAMA, *J. Mater. Chem.* **21**, 19187 (2011).
- [120] P. LIEHM, C. MURAWSKI, M. FURNO, B. LÜSSEM, K. LEO, and M. C. GATHER, *Appl. Phys. Lett.* **101**, 253304 (2012).
- [121] L. PENNINCK, F. STEINBACHER, R. KRAUSE, and K. NEYTS, *Org. Electron.* **13**, 3079 (2012).
- [122] R. MEERHEIM, M. FURNO, S. HOFMANN, B. LÜSSEM, and K. LEO, *Appl. Phys. Lett.* **97**, 253305 (2010).
- [123] S. WEHRMEISTER, Analyse der Quanteneffizienz organischer Farbstoffe mittels zeitaufgelöster Spektroskopie, Master's thesis, University of Augsburg, 2013.
- [124] T. D. SCHMIDT, D. S. SETZ, M. FLÄMMICH, B. J. SCHOLZ, A. JAEGER, C. DIEZ, D. MICHAELIS, N. DANZ, and W. BRÜTTING, *Appl. Phys. Lett.* **101**, 103301 (2012).
- [125] T. D. SCHMIDT, A. RAUSCH, B. J. SCHOLZ, C. MAYR, D. MICHAELIS, T. REUSCH, N. DANZ, and W. BRÜTTING, **in preparation** (2013).
- [126] S. XIA, R. KWONG, V. ADAMOVICH, M. WEAVER, and J. BROWN, OLED Device Operational Lifetime: Insights and Challenges, in *Reliability physics symposium, 2007. proceedings. 45th annual. ieee international*, pp. 253–257, 2007.
- [127] R. MEERHEIM, S. SCHOLZ, S. OLTHOF, G. SCHWARTZ, S. REINEKE, K. WALZER, and K. LEO, *J. Applied Phys.* **104**, 014510 (2008).
- [128] G. GU, D. Z. GARBUZOV, P. E. BURROWS, S. VENKATESH, S. R. FORREST, and M. E. THOMPSON, *Opt. Lett.* **22**, 396 (1997).
- [129] C. MIESKES, Entwicklung eines neuen Probandesigns für transiente Elektrolumineszenz-Messungen an phosphoreszenten OLEDs, Bachelor Thesis, University of Augsburg, 2011.
- [130] Y. NOGUCHI, Y. MIYAZAKI, Y. TANAKA, N. SATO, Y. NAKAYAMA, T. D. SCHMIDT, W. BRÜTTING, and H. ISHII, *J. Appl. Phys.* **111**, 114508 (2012).
- [131] L. JÄGER, Private communications.
- [132] C. FÉRY, B. RACINE, D. VAUFREY, H. DOYEUX, and S. CINA, *Appl. Phys. Lett.* **87**, 213502 (2005).

- [133] F. SO and D. KONDAKOV, *Adv.Mater.* **22**, 3762 (2010).
- [134] Z. D. POPOVIC, H. AZIZ, N.-X. HU, A. IOANNIDIS, and P. N. M. DOS ANJO, *J. Appl. Phys.* **89**, 4673 (2001).
- [135] Z. D. POPOVIC, H. N.-X. AZIZ, A. IOANNIDIS, HU, and P. N. M. DOS ANJO, *Synth. Met.* **123**, 179 (2001).
- [136] D. Y. KONDAKOV and R. H. YOUNG, *J. Appl. Phys.* **108**, 074513 (2010).
- [137] D. Y. KONDAKOV, *J. Appl. Phys.* **104**, 084520 (2008).
- [138] N. C. GIEBINK, B. W. D'ANDRADE, M. S. WEAVER, J. J. BROWN, and S. R. FORREST, *J. Appl. Phys.* **105**, 124514 (2009).
- [139] I. R. DE MORAES, S. SCHOLZ, B. LÜSSEM, and K. LEO, *Appl. Phys. Lett.* **99**, 053302 (2011).
- [140] S. SCHOLZ, B. LÜSSEM, and K. LEO, *Appl. Phys. Lett.* **95**, 183309 (2009).

PUBLICATIONS

List of publications

- J. Frischeisen, B. J. Scholz, B. J. Arndt, T. D. Schmidt, R. Gehlhaar, C. Adachi, and W. Brütting, *Strategies for light extraction from surface plasmons in organic light-emitting diodes*, J. Photon. Energy. **1**, 011004 (2011).
- D. S. Setz, T. D. Schmidt, M. Flämmich, S. Nowy, J. Frischeisen, B. C. Krummacher, T. Dobbertin, K. Heuser, D. Michaelis, N. Danz, W. Brütting, and A. Winnacker, *Comprehensive Efficiency Analysis of Organic Light-Emitting Devices*, J. Photon. Energy. **1**, 011006 (2011).
- T. D. Schmidt, A. Buchschuster, M. Holm, S. Nowy, J. A. Weber, and W. Brütting, *Degradation effect on the magnetoresistance in organic light-emitting diodes*, Synth. Met. **161**, 637-641 (2011).
- M. Flämmich, J. Frischeisen, D. S. Setz, D. Michaelis, B. C. Krummacher, T. D. Schmidt, W. Brütting, and N. Danz, *Oriented phosphorescent emitters boost OLED efficiency*, Org. Electron. **12**, 1663-1668 (2011).
- W. Brütting, J. Frischeisen, B. J. Scholz, and T. D. Schmidt, *More light from organic light-emitting diodes*, Europhys. News **42**, 20-24 (2011).
- T. D. Schmidt, D. S. Setz, M. Flämmich, J. Frischeisen, D. Michaelis, B. C. Krummacher, N. Danz, and W. Brütting, *Evidence for non-isotropic emitter orientation in a red phosphorescent organic light-emitting diode and its implications for determining the emitters radiative quantum efficiency*, Appl. Phys. Lett. **99**, 163302 (2011).

- A. Buchschuster, T. D. Schmidt, and W. Brütting, *Evidence for different origins of the magnetic field effect on current and electroluminescence in organic light-emitting diodes*, Appl. Phys. Lett. **100**, 123302 (2012).
- T. D. Schmidt, B. J. Scholz, C. Mayr, and W. Brütting, *Non-isotropic emitter orientation and its implications for efficiency analysis of organic light-emitting diodes*, Proc. SPIE **8435**, 843513 (2012).
- Y. Noguchi, Y. Miyazaki, Y. Tanaka, N. Sato, Y. Nakayama, T. D. Schmidt, W. Brütting, and H. Ishii, *Charge accumulation at organic semiconductor interfaces due to a permanent dipole moment and its orientational order in bilayer devices*, J. Appl. Phys. **111**, 114508 (2012).
- W. Brütting, J. Frischeisen, T. D. Schmidt, B. J. Scholz and C. Mayr, *Device efficiency of organic light-emitting diodes: Progress by improved light outcoupling*, phys. stat. sol. a **210**, 1862-6319 (2013).
- T. D. Schmidt, D. S. Setz, M. Flämmich, B. J. Scholz, A. Jaeger, C. Diez, D. Michaelis, N. Danz, and W. Brütting, *Degradation induced decrease of the radiative quantum efficiency in organic light-emitting diodes*, Appl. Phys. Lett. **101**, 103301 (2012).
- T. D. Schmidt, B. J. Scholz, C. Mayr, and W. Brütting, *Efficiency Analysis of Organic Light-Emitting Diodes Based on Optical Simulations*, IEEE, submitted (2013).
- S. Wehrmeister, T. D. Schmidt, D. S. Setz, M. Flämmich, A. Rausch, D. Michaelis, T. Reusch, N. Danz, and W. Brütting, *Efficiency roll-off of organic-light emitting diodes: Evidence for Triplet-Polaron-Quenching as main process*, in preparation (2013).
- T. D. Schmidt, A. Rausch, B. J. Scholz, C. Mayr, D. Michaelis, T. Reusch, N. Danz, and W. Brütting, *Thermally activated delayed fluorescence induced increase of the radiative exciton fraction in organic light-emitting diodes*, in preparation (2013).

List of conference contributions and awards

List of international conference contributions

- *Degradation effect on the magnetoresistance in organic light emitting diodes*, SPINOS, Amsterdam, Netherlands (2010).
- *Determination of the effective radiative quantum efficiency of organic light-emitting guest-host systems*, DPG Frühjahrstagung, Dresden, Germany (2011).
- *Determination of the radiative quantum efficiency in organic light-emitting guest-host systems*, OLED100.eu Summer School 2011, Kögis, Germany (2011).
- *Evidence for non-isotropic emitter orientation in a red phosphorescent organic light-emitting diode and its implications for efficiency analysis*, DPG Frühjahrstagung, Berlin, Germany (2012).
- *Non-isotropic emitter orientation and its implications for efficiency analysis in organic light-emitting diodes*, SPIE Europe, Brussels, Belgium (2012).
- *Efficiency analysis of organic light-emitting diodes based on non-isotropically oriented phosphorescent emitters*, ICEL, Fukuoka, Japan (2012).
- *Comprehensive efficiency analysis of organic light-emitting diodes*, Seminar Talk Ishii's Lab, Chiba University, Japan (2012).
- *Degradation induced decrease of the radiative quantum efficiency in organic light-emitting diodes*, DPG Frühjahrstagung, Regensburg, Germany (2013).

Awards

- **Best student paper award**, *Non-isotropic emitter orientation and its implications for comprehensive efficiency analysis of organic light-emitting diodes*, SPIE Photonics Europe, Brussels, Belgium (2012).

DANKSAGUNG

- **Prof. Dr. Wolfgang Brütting** für die Aufnahme in seine Arbeitsgruppe, das unerschöpfliche Vertrauen in meine Arbeit und die vielen Hilfestellungen und Anregungen in unzähligen Gesprächen und Diskussionen.
- **Prof. Dr. Achim Wixforth** für seine Bereitschaft das Zweitgutachten meiner Dissertation zu erstellen.
- **Prof. Dr. Bernd Stritzker** für die Aufnahme an seinen Lehrstuhl.
- allen Studenten, die ich während meiner Zeit bei Ihren Abschlußarbeiten betreut habe und deren Ergebnisse teilweise auch hier präsentiert wurden: **Benjamin Lebsanft, Andreas Buchschuster, Matthias Holm, Robert Hanfland, Johannes Braun, Christoph Mieskes** und **Sebastian Wehrmeister**. Vielen Dank für euren unstillbaren Wissensdurst und die hervorragende und manchmal auch witzige Zusammenarbeit.
- meinen (ehemaligen) Kolleginnen und Kollegen in der Arbeitsgruppe und am gesamten Lehrstuhl, im Speziellen **Julia Wagner, Dr. Michael Kraus, Dr. Jörg Frischeisen** (für das Mentoring und Korrekturlesen), **Ulrich Hörmann** (für die unzähligen Hilfestellungen), **Mark Gruber, Bert Scholz** (auch für das Korrekturlesen), **PD Dr. Andreas Opitz, Dr. Thomas Wehlus, Stefan Grob, Christian Mayr, Lars Jäger, Theresa Linderl, Michael Weinl, Christian Stehl, Alfred Grießer** und **Daniel Kraus**, sowie dem gesamten Rest von EPIV für die hervorragende Arbeitsatmosphäre, der gegenseitigen Unterstützung, den interessanten teambildenden Maßnahmen und die netten Gespräche auf den Gängen. Vielen Dank.
- **Cornelia Ludescher**, die als Sekretärin in unserer gemeinsamen Zeit am Lehrstuhl immer ein offenes Ohr für mich hatte.

- **Maria Fuso** für die darauf folgenden drei Jahre im Sekretariat und als gute Seele der "Männerbande". Vielen Dank für die tolle gemeinsame Zeit und das viele Gequatsche über den Tresen hinweg. Ich wünsche dir von Herzen alles Gute an deiner neuen Arbeitsstelle.
- **Wolfgang Reiber, Birgit Knoblich und Sybille Heidemeyer**, die für alle technischen Fragen aber auch bei Feierlichkeiten immer mit Rat und Tat parat standen.
- der **Feinmechanischen Werkstatt** für die schnelle und unkomplizierte Abwicklung meiner Wünsche.
- **Prof. Hisao Ishii** and **Assistant Prof. Yutaka Noguchi** for giving me the opportunity to doing research at Chiba University. **Dr. Yuya Tanaka** and **Hyunsoo Lim** for the affectionate accommodation in Japan, in particular at Ishii's lab and for helping me with everything.
- allen Kolleginnen und Kollegen bei OSRAM OS, Regensburg, insbesondere **Dr. Thilo Reusch, Dr. Carola Diez, Dr. Daniel Setz, Dr. Arndt Jaeger, Dr. Andreas Rausch** und **Dr. Benjamin Krummacher** für die hervorragende Zusammenarbeit und die vielen langen und interessanten Diskussionen.
- allen Kollegen des IOF Jena für die gute Zusammenarbeit, die vielen Diskussionen und die gemeinsamen Publikationen. Insbesondere seien erwähnt: **Dr. Michael Flämmich, Dr. Dirk Michaelis** und **Dr. Norbert Danz**.
- meinen Geldgebern, insbesondere den vom **BMBF** geförderten Projekten OPAL (FKZ 13N8995), TOPAS (FKZ 13N10474) und OLYMP, sowie der **DFG** in dem Projekt Br 1728/6.
- **meinen Eltern** für die endlose Unterstützung sowohl während meines Studiums, als auch während meiner Promotion.
- und vor allem meiner Frau **Nicole** für die unglaubliche Geduld (speziell in der Endphase meiner Dissertation), die Aufmunterungen und für einfach alles. Danke, dass es dich gibt!

CURRICULUM VITAE

Personal data

Name: Tobias Daniel Schmidt
Date of birth: March 18, 1983
Place of birth: Augsburg
E-Mail: tobias.schmidt@physik.uni-augsburg.de, Tobias_D_Schmidt@gmx.de
Marital status: married

Education

10/2009 – 01/2013 **PhD thesis at University of Augsburg**
Institute of Physics
Advisor: Prof. Dr. Wolfgang Brütting
Topic: "Photophysics of organic light-emitting diodes –
Device efficiency and degradation processes"
09/2003 – 02/2009 **Studies of teaching degree for secondary schools
in mathematics and physics**
Degree: Erstes Staatsexamen
Zulassungsarbeit:
"Lumineszenz an Quantentöpfen"
09/1993 – 07/2002 **Gymnasium Wertingen**
Degree: Abitur

Military service

08/2002 – 04/2003 **Transportbattalion 220 in Günzburg**
